UNIVERSITY OF OKLAHOMA

GRADUATE COLLEGE

INTEGRATED GEOPHYSICAL STUDIES OF THE NORTHEASTERN CARIBBEAN PLATE, EASTERN TIBETAN PLATEAU IN CHINA AND PANHANDLE FIELD (TEXAS)

A DISSERTATION

SUBMITTED TO THE GRADUATE FACULTY

in partial fulfillment of the requirements for the

Degree of

DOCTOR OF PHILOSOPHY

By

XIAO XU
Norman, Oklahoma
2014

INTEGRATED GEOPHYSICAL STUDIES OF THE NORTHEASTERN CARIBBEAN PLATE, EASTERN TIBETAN PLATEAU IN CHINA AND PANHANDLE FIELD (TEXAS)

A DISSERTATION APPROVED FOR THE
CONOCOPHILLIPS SCHOOL OF GEOLOGY AND GEOPHYSICS

BY

_____
Dr. G. Randy Keller, Chair

_____
Dr. Kurt J. Marfurt

_____
Dr. May Yuan

_____
Dr. Jamie Rich

_____
Dr. Kevin Mickus

Acknowledgements

I would never have been able to finish my dissertation without the guidance of my committee members, help from friends, and support from my family and wife.

I would like to express my deepest gratitude to my supervisor Dr. G. Randy Keller, for your excellent suggestions, guidance, providing me with an excellent atmosphere for doing research and unwavering continuous support during these five years. Thank you for believing in me during this research and continuously funding me during these years. Your knowledge and noble qualities will be lifetime wealth for me. I would like to thank Dr. Kurt J. Marfurt for instilling in me the qualities of being a good scientist. I would also like to thank my committee members Dr. May Yuan, Dr. Jamie Rich, and Dr. Kevin Mickus for their continuous support and cooperation.

The Longmen Shan project was supported by the SinoProbe-02 Project, a National Natural Science Foundation of China grant (40830316) and a U.S. National Science Foundation, Partnerships for International Research and Education grant (0730154). I thank all our colleagues from both China and USA who have worked in the field to collect the seismic data used in this study, and the No. 6 Geophysical Prospecting Team, Sinopec Huadong Petroleum Bureau, Nanjing, China, for their excellent and enthusiastic work under difficult terrain and logistic conditions. Also I would like to thank Cimarex Energy for providing 3D seismic data and aeromagnetic data for Gray County, USGS, PACES, and IRIS were the free online data resources. Without these data, this dissertation would never exist. I used FMTOMO package by Dr. Nick Rawlinson for tomographic modeling all three projects. He thoroughly and answered my questions about the code, I am cordially thankful to him. Many thanks are

going to the Computational Infrastructure for Geodynamics (CIG) project because of the open source Gale finite element-based code.

I am grateful to Dr. Kevin Crain, Stephan Holloway, and Galen Kaip for all kinds of technical supports as well as help during field works. I appreciate the time and support from my colleagues Guang Chen, Bo Zhang, Chen Chen, Murari Khatiwada Hamed Alrefaee, and Jefferson Chang while running different software, and proofreading my writing.

Last but not the least, I would like to thank my family, my mother Jianqiu Hong, my wife Xiaoyu Guo and my son Chongyuan Xu. You were always there cheering me up and stood by me through the good times and bad. Without your support and endless love, this work would not have been complete.

Table of Contents

List of Tables

List of Figures

Chapter 3: Imaging Igneous Basement Structures in the Panhandle Field of the Western Anadarko Basin by Integrating 3D Seismic, Gravity, and Magnetic Data

Abstract

There are three different areas and research projects that are the targets of this proposed dissertation. These projects have the common theme of integration of a variety of data but are at different scales. The first one focuses on plate scale interactions in northeastern Caribbean at a lithospheric scale. The second one focuses on crustal scale deformation in the eastern Tibetan Plateau. The last project is in the Panhandle oil and gas field in Texas and targets the structure of basement and seismic attributes of reservoirs.

The first project targets slab dip variations of the Caribbean Plate along the Muertos Trough, which bounds the Puerto Rico-Virgin Islands tectonic block on the south. Results of this research are intended to contribute to understanding the kinematic evolution of this region and the associated natural hazards. Two-dimensional gravity modeling is being employed to address this question for the first time. Integration of the potential field data and seismic data is providing details on the geometry of the subducting slab of the northeastern Caribbean plate. To further reveal the 3D deep structural geometry, P wave tomography is also being used in this research.

The second project aims to explore the lithospheric structure across the Songpan-Ganzi terrane, LMS and western Sichuan basin by undertaking an integrated analysis of deep seismic profiling, gravity, magnetic, and geologic data. Based on our new results and previous research, a 2D numerical simulation was conducted using three initial models with different viscosity structures. These modeling results show that the uplift and crustal thickening observed can be due simply to ductile deformation in the middle crust west of the LMSFZ.

The third project focuses on the igneous basement structures of Panhandle Field in northern Texas by integrating 3D seismic reflection data, aeromagnetic data and gravity data. The gravity and magnetic data are the useful tool to identify these igneous basement structures. The high-resolution 3D seismic data were collected in Gray County, Texas. I employ volumetric seismic attributes such as instantaneous frequency, instantaneous phase and cosine instantaneous phase derived from 3D seismic data to better characterize subtle features such as collapse features, faulting and fracturing within the deposits that are difficult to detect on conventional 3D seismic data displays. Our research show the igneous basement has been broken into a series of grabens and horsts bounding with normal and reverse faults due to rifting, uplifting and left-lateral deformation.

Introduction

The geophysical methods are developing with time; it has been used more often because of the upgrade of methods and instruments. So it helps scientists to find new geological information. So integrated analysis with different geophysical methods is a powerful tool to solve geologic problems. In this dissertation, three major datasets, seismic gravity and magnetic data, have been used and interpreted the results with geologic observations to discover the subsurface structures. Three different areas in different tectonic provinces in different plates, which are: northeastern Caribbean plate, eastern Tibetan Plateau, the Panhandle oil and gas field in Texas. In Puerto Rico-Virgin islands, I studied the geometry of northeastern Caribbean plate and North American Plate. The second project is focused on the uplifting mechanism of Longmen Shan area in eastern Tibetan Plateau. Whereas in Panhandle field, the main purpose is the structure of igneous basement and tectonic evolution of this area. The primarily target of this dissertation is to identify the tectonic and structural features of local and regional geological settings of the study areas by integrating with different geophysical datasets with geological data.

This dissertation includes three different chapters and each chapter is standalone scientific paper. These chapters are at different stage of publications. Chapter 1 on the Puerto Rico-Virgin islands and adjacent areas has submitted to the Geosphere Journal by Geological Society of America. Chapter 2 on Longmen Shan area in eastern Tibetan Plateau is almost ready to submit to the Journal of Geophysical Research (Solid Earth) by American Geophysical Union. Chapter 3 on the Panhandle field will be submitted to

the Geosphere Journal by Geological Society of America and currently under preparation.

CHAPTER 1: Dip variations of the North America and North Caribbean plates dominate the tectonic activities of the Puerto Rico-Virgin Islands and adjacent areas

[This chapter has been submitted to "*Geosphere*". Dr. G. Randy Keller and Dr. Xiaoyu Guo are co-authors for this paper]

Chapter 1: Dip variations of the North America and North Caribbean plates dominate the tectonic activities of the Puerto Rico-Virgin Islands and adjacent areas

ABSTRACT

The M 7.0 Haiti earthquake of 2010 in the Greater Antilles is a reminder that the northeastern Caribbean is at a high risk for seismic and tsunami hazards. The Greater Antilles consists of the Hispaniola micro-plate and Puerto Rico-Virgin Islands to the east, which are situated between two subduction zones with the Puerto Rico trench to the north and the Muertos trough to the south. Although there is no active volcanism on Puerto Rico, earthquake depths and previous seismic tomography results imply that the slabs of Caribbean and North American Plates exist at depth. However, how far east Muertos Trough subduction of the North Caribbean Plate has extended has not been fully addressed. In addition, the Puerto Rico-Virgin Islands is bounded by extensional regimes to both the west (Mona Passage) and east (Anegada Passage). The cause of the extension is still under debate. In this paper, we use new 3D seismic tomography and gravity data to carry out an integrated study of the geometry of the subducting slabs of the North American and North Caribbean Plates. The results indicate that both slabs have an increase of dip westward, which is strongly controlled by the subduction rollback of the North American Plate. These variations affected the tectonic evolution of the Puerto Rico-Virgin Islands. Thus, the results of this research advance our understanding of the kinematic evolution of the Puerto Rico-Virgin Islands and associated natural hazards.

INTRODUCTION

The Greater Antilles (GA) separate the Caribbean Plate from the North American plate to the north (Fig. 1.1). The eastern GA consists of two micro-plates, the Hispaniola micro-plate (HM) and the Puerto Rico-Virgin Islands (PRVI) micro-plate (Jansma & Mattioli, 2005) (Fig. 1.1). The North American subduction zone (NASZ) bounds the GA to the north with the Puerto Rico Trench (PRT) occupying the eastern part of the NASZ. The southern boundary of the HM and PRVI coincides with the Muertos Trough (MT), which is due to subduction of the Northern Caribbean Plate (Fig. 1.1). The North Caribbean subduction zone (NCSZ) is not as long as the NASZ, and it is currently only documented in the central and western portions of the GA (ten Brink, 2005).

The Mona Passage (MP) is situated northwest of the PRVI (Fig. 1.1). It is connected with the Great Southern Puerto Rico fault zone (GSPRFZ) by the Cerro Goden fault zone (Mann et al., 2005a; Chaytor and ten Brink, 2010) (Fig. 1.1). GSPRFZ is the principal structural feature along the southern coast of Puerto Rico and consists of several parallel to sub-parallel sinistral faults oriented NW-SE. The GSPRFZ originally experienced sinistral displacement from the Eocene to Oligocene (55-35 Ma), and horizontal movement continued as late as the early Miocene (*Rodríguez-Martínez, 2007).* Initial rifting of the MP to the northwest of the GSPRFZ started in the Oligocene (Mann et al., 2002). The Anegada Passage (AP) is located between the PRVI and the Lesser Antilles-St. Croix. It extends from the northern Lesser Antilles to the north of St. Croix (Fig. 1.1), and cuts the late Neogene strata (Speed and Larue, 1991). St. Croix was originally part of the PRVI. It rifted away and was uplifted in the Neogene during

the opening of the AP (Gill et al., 1989). The northern coast of Puerto Rico contains exposures of a relatively small part of the carbonate platform during late Neogene tectonic uplift (Gestel et al., 1998). Deposition of a carbonate platform in most of the PRVI began in the early Oligocene to Holocene and overlies a stable and sinking island arc. Based on previous paleomagnetic studies, the Neogene carbonate platform in Puerto Rico experienced 25° of counterclockwise (CCW) rotation in late Miocene-Pliocene time (Mann et al., 2002; 2005a). Present-day GPS data show that the CCW continues and that the rotation pole migrated to 67.10W, 16.61N (ten Brink and López-Venegas, 2012) (Fig. 1.1).

The Northern Caribbean Plate (NCP), as well as the HM and PRVI, is generally moving NNE relative to the North American Plate (NAP) but with slight variations of direction and rate (Mann, 2005a; ten Brink and López-Venegas, 2012; Benford et al., 2012). As a result, large sinistral strike-slip faults and normal faults were produced in this the eastern Greater Antilles (Fig. 1.1). The question of what caused these differential movements within the western and eastern PRVI has not yet been fully resolved, and several models have been proposed (Jolly et al., 2007; Mann et al., 2002, Mann et al., 2005a; van Gestel et al., 1998; Granja Bruña et al., 2009). ten Brink and Granja Bruña (2009) proposed that bivergent-thrusting exists on both sides of the PRVI. The numerical modeling of Sokoutis and Willingshofer (2011) suggests the subducting slabs have varied dip angles and depths. In addition, previous research (ten Brink, 2005; Meighan & Pulliam, 2013) on the southward subduction of the NAP suggested that the North American subduction slab (NASS) splits in the eastern PRVI. So far, however, no models have been attempted to explain the variation along the North Caribbean

subduction zone (NCSZ), although the NCSZ and NASZ could both have affected the tectonic evolution of the PRVI. Therefore, in this paper, we employ new 3D seismic tomography results and gravity data to carry out an integrated study on the geometry of the subducting slabs along both the Northern American and Northern Caribbean plates. These results will provide new constraints on models of the kinematic evolution of the PRVI.

INTEGRATED STUDIES OF GRAVITY AND TOMOGRAPHIC DATA

Gravity Data

Gravity anomaly data used in this study were extracted from the International Center for Global Earth Models (ICGEM), and our land data was collected in western Puerto Rico in 2010. These data were combined, plotted and filtered with the Geosoft/Oasis Montaj processing and analysis package. The merged data set involves a combination of free-air anomalies offshore and simple Bouguer gravity anomalies onshore. The initial free air gravity anomaly data (Fig. 1.2) are strongly affected by the depth of seawater. As a result, deep-seated structures are masked by low gravity anomalies offshore. Therefore, we employed a traditional approach to remove the water effect by using bathymetry to apply a Bouguer correction in the marine areas using a density difference of 1.645 g/cc for the seawater. In addition, in order to highlight the long wavelengths and enhance the large-scale tectonic framework, upward continuation (to 30 km) was utilized (Fig. 1.3). Also in addition, an edge detection technique, e.g. tilt derivative (TD), was used to detect the large-scale geological structures and trends (Blakely and Simpson, 1986) (Fig. 1.4). This technique was applied to aid understanding the edge of the subduction zones and plate boundaries. As defined by

Cooper and Cowan (2006), the TD is the ratio between the total horizontal gradient (THG) and the absolute value of vertical derivative of the potential field. The TD is expressed as:

$$TD = \arctan (THG / abs (\partial f / \partial z)). \quad (1)$$

Where f is the potential field, $\partial f / \partial z$ measures the rate of change of potential field in the Z direction; THG is the total horizontal gradient, which is defined as:

$$THG = sqrt ((\partial f / \partial x)^2 + (\partial f / \partial y)^2). \quad (2)$$

Where $(\partial f/\partial x)$ and $(\partial f/\partial y)$ measure the rate of change of potential field in the X and Y directions, respectively. THG is created as a resultant grid.

TD is thus the angle between the THG (x and y directions) and the first vertical derivative. For typical sources, the maximum of the TD is over or near the source edge, and the minimum is over the source (Cooper and Cowan, 2006). TD performs almost equally well with both the deep and shallow sources (Cooper and Cowan, 2006). In addition, lineaments produced by the TD generally run parallel to contact boundaries (Nasuti et al., 2012). The edges of the subduction zones are shown clearly in Figure 1.3. Because the total horizontal gradient decreases faster than vertical derivative along the dip of the subduction zone, the rust linear anomalies on both sides of the eastern PRVI are interpreted as the footprints of the subducting slabs from both the North American and North Caribbean Plates, respectively.

Three tectonic units, the NAP, the HM-PRVI, and the North Caribbean Plate (NCP), are separated by two distinct gravity gradients (Figs. 1.3 and 1.4). Positions of these two subducting slabs are well delineated on the tilt derivative map **(**Fig. 1.4**)**. The PRT and MT are generated from the subduction of the NAP and NCP, respectively, and

the east-west broad gradient zones on both sides of the Greater Antilles (GA) can be interpreted as the signature of the upper portion of the subducting slabs. The two slabs nearly merge in the middle of the Virgin Islands (65^{o} W) (Figs. 1.3 and 1.4). The northern boundary of the NAP's gradient fits most segments of the PRT but shifts to the north of the Bahamas platform to the west due to a buildup thickness of the more than 5km thick carbonate platform of the Bahamas (Jansma, 1981). As the boundary between GA and NCP, the MT coincides with the gradient zone bounding the northern NCP. The eastern gradient of the North Caribbean subducting slab (NCSS) crosses St. Croix and is blocked by the Virgin Islands (Fig. 1.4).

The average Simple Bouguer anomaly values of the PRVI after upward continuation are higher than those of the HM and increase to the east **(**Fig. 1.3**)**, which is consistent with the Moho depth decreasing eastward (Lin and Huerfano, 2011). In addition, trends of the gravity gradient vary from N-S to E-W across the MP from east to west, which are primarily E-W west of the MP and this difference indicates a significant variation crustal and upper most mantle structure. (Figs. 1.3 and 1.4). The Main Ridge in the southern PRT (Fig. 1.1) caused rupture of NASS (ten Brink, 2005) (Fig. 1.4). The NNW-trending anomaly high(labeled M in Figs. 1.3 and 1.4) in the north of Puerto Rico Island could be due the North American subducting slab (NASS) has compressed in a nearly east-west direction by the anti-clockwise rotation of PRVI (ten Brick and López-Venegas, 2012)(Fig. 1.4). The distribution of earthquakes in this area (Fig. 1.1) shows the correlation with the activities of NASS. So the NNW-trending anomaly low between MR and PRVI is due to the split of North American subducting slab. In the western PRVI, a continuous anomaly is shown to connect the MP with the

GSPRFZ (Fig. 1.4).

Tomographic Data

Previous tomographic studies have indicated that there is no subduction of the northern Caribbean Plate beneath the eastern PRVI (McCann, 2010; Mendoza and McCann, 2005). However, this result is questionable due to the limited coverage of seismic sources. In this study, the passive seismic data downloaded from the IRIS Data Management Center are distributed across the whole PRVI and the two subducting zones, ranging from 16^{o} N to 21^{o} N latitude and 70^{o} W to 62^{o} W longitude (Fig. 1.1). The seismic stations in this area were operated during different time frames, and thus, the earthquake data whose first arrival travel-time were picked span from 2000 to 2010. By using the 1-D velocity model of (McCann, 2007) (Table 1.1), the sources were relocated based on the first arrival picks using the SEISAN software package (Ottemöller et al., 2013). This initial 1-D, P-wave velocity model for the tomographic calculations was based on previous 1-D and 3-D models (McCann, 2000; Mendoza and McCann, 2005; Ficher and McCann, 1984). In this study, this initial model was also employed for the tomographic calculations of travel times that were made using the Fast Marching Tomography (FMTOMO) method (Rawlinson and Urvoy, 2006), which is a Fortran 90 software package for 3D travel-time tomography. It is one of the research products developed by Prof. Nick Rawlinson at Australian National University. The FMTOMO code is designed to simultaneously invert multiple travel time datasets for 3D velocity variations and interface structure. FMTOMO combines forward modeling and inversion, the forward traveltime modeling is solved by the fast marching method (FMM), and the inversion is a fitting of observations by the adjustment of model

parameters. The inversion uses a non-linear iterative process with the assumption of local linearity. The FMM and inversion are run repeatedly with constraints to reconcile the non-linear relationship between velocity and traveltime perturbations. A second relocation of hypocenters was undertaken using the FMTOMO code in a 3D velocity model due to the importance of accurate determination of earthquake hypocenters. In this study, the top and bottom of the 3D model were placed at 5 km above sea level and 185km below the sea level respectively. After relocation, the hypocenters that were outside of the grid were deleted. Finally, a total of 217 relocated events were included in the velocity calculation (Fig. 1.1).

In order to estimate the resolution of the tomography model derived, we performed checkerboard tests (Figs. 1.5). The synthetic dataset was generated using a one-layer model without interfaces. The background velocity within the model was set to 8.5 km/s, and a checkerboard pattern with amplitude of 1.5 km/s was added over the 3D model with a velocity grid whose dimensions were 0.42°x0.67°x19km (Figs. 5A and 5B). Thereafter, synthetic travel times were generated by FMTOMO through this model, which was first modified by adding uncertainties of +/- 0.1s as required by the FMTOMO code. The starting model was created without perturbations and is in the same velocity background (Table 1.1). The inversion of the synthetic arrival time residuals met the convergence minimum value after 6 iterations. The horizontal slices (Figs. 1.5C and 1.5D) show that the data cover most of the research area with good resolution. The cross-sections have better resolution beneath the PRVI above 50km depth (Figs. 1.5E-1.5G).

Our final P wave velocity model was calculated after 3-D inversion using the

original 1-D starting model. The variations of velocities above the dashed lines in our checkerboard test results (Figs. 1.5E-1.5G) are reliable. Owing to the numbers of deep seismic data, only 20 events are deeper than 50km, the tomography at 50 km depths only shows the geometry of two slabs beneath PRVI (Figs. 1.5F and 1.5G). Our results are shown in Figure 1.6, where high-velocity anomalies are blue and low-velocity anomalies are red. Most of geological components can be identified in P wave tomography results (Fig. 1.6). The NASS splits along the eastern Main Ridge and crosses the Puerto Rico Trench (Figs. 1.6D, 1.6E). The NASS beneath the west of the Main Ridge has a higher dip angle than that of other segments along this subduction zone (Figs. 1.6A-1.6C). Along the 65W longitude, the northern tip of the eastern NCSS reaches the Virgin Islands, which is evidenced by tomographic and gravity data (Figs. 1.4 and 1.6G). The two slabs almost meet in the middle Virgin Islands (Fig. 1.6E). The distance between the tips of these two subduction slabs increases toward the west (Figs. 1.6A-C). The high velocity zone bounding the southeastern PRVI represents the Anegada Passage zone of rifting, which separates St. Croix from the PRVI (Figs. 1.6D and 1.6E).

The Moho depth beneath Puerto Rico decreases eastward (Lin and Huerfano, 2011). The architecture of the Moho beneath the PRVI is flat and undeformed in the eastern PRVI (Figs. 1.6A, 1.6B and 1.7B**)**. The left-lateral Great Southern Puerto Rico Fault Zone (GSPRFZ) and Great Northern Puerto Rico Fault zone (GNPRFZ) coincide with sharp velocity discontinuities in Figure 1.6D, which cut through the Moho depth of western Puerto Rico (Mann et al., 2005b) and separate the Puerto Rico into three different igneous provinces (Figs. 1.6B and 1.7C). The southwestern igneous province

is composed of basalt, serpentinized peridotite and andesite. The central igneous province between the GSPRFZ and GNPRFZ consists of plutons and volcanic strata. The northeastern igneous province is composed of lava and lava breccia (Jolly et al., 2008). The high velocity area bounding the MP and GSPRFZ can be continuously traced northwest of Puerto Rico (Figs. 1.6D and 1.6E). High and low velocity zones alternate in the north of Puerto Rico (Figs. 1.6D and 1.6E) and may be caused by the compression due to the Main Ridge. The same pattern is shown in the gravity data (Figs 1.3 and 1.4). The contact zone between these two slabs varies westward. Both slabs increase in depth and the distance between the tips widens to the west. Our results clearly show the geometry of the two subduction zones. The tomographic images show that Puerto Rico has been separated by two main fault zones into three geological segments. The Mona Passage and Anegada Passage are displayed well as low velocity zones.

2D Gravity Modeling and Tomographic Profiles

The 2D gravity modeling and tomographic cross-sections along three longitudes were constructed to show the geometry of the main tectonic structures across the PRVI (Figs. 1.7A-1.7C). This integrated modeling was based on bathymetry, gravity values, earthquake hypocenters, and 3D tomography results. The locations of the NAP, NCP and PRVI are determined by tomography results and earthquake hypocenters. The intracrustal structures were determined by gravity values and previous researches.

In the integrated models, the dips of both the NCSS and NASS increase westward (Figs. 1.7A-1.7C), which is also suggested by the bathymetric variations of the onshore-offshore slopes of the PRVI, where the slope of the western PRVI is steeper

than that of the eastern PRVI. Because of the steep subduction angle, the PRT has a steeper slope than the MT (Figs. 1.1 and 1.7A-1.7C) (Gvirtzman and Stern, 2004; Sokoutis and Willingshofer, 2011). We interpret this variation in subduction angle of the NCSS to be a result of the roll back of the NASS. The plate kinematics of the PRVI are controlled by the dynamic movements of the NASS and NCSS. The horizontal stresses are different in different locations because of the dip-angle variations of two subducting slabs. Thus, dip-angle variations of the NCSS can account for the differential direction and velocity of motion between the eastern Hispaniola micro-plate (HM) and the PRVI.

Based on the distribution of earthquakes (Fig. 1.1), our interpretation is that the eastern NCSS has probably been locked because of its continuous extension beneath St. Croix but with a low rate of seismic activity. As shown in Figure 1.7A, the NCSS overlies the NASS with a relatively low dip angle in the east. As a result, the movement of the NCSS creates large stress along the contact with the eastern PRVI, and thus, movement of St. Croix Island could have been blocked by the NCSS. Therefore, the Anegada Passage started rifting due to the relatively stable eastern PRVI and northward extension due to the roll back of the NASS. In the central portion of the NASS and NCSS interaction (Fig. 1.6B), the NASS has a steeper dip, which provides enough space for the NCSS to move northward without being blocked by the NASS (Fig. 1.7B). As a result, more shallow earthquakes along the south coast of the PRVI are generated. With continuous increase of the dip angle of the NCSS and NASS westward (Fig. 1.7C), deeper earthquakes beneath the western PRVI and eastern HM are generated.

With respect to the NASS, it is split into two segments with an opening slab window around the Main Ridge (MR) due to its low density (ten Brink et al., 2009) and

thus resistance to subduction. This split is suggested by the seismic quiet zone between the MR and PRVI and the MR boundary with earthquake clusters on each side (ten Brink, 2005). The NASS consists of two segments with different dip angles that are bounded by the Main ridge (ten Brink et al., 2009) (Figs. 1.7A-C). Today, the NCP, as well as the Hispaniola micro-plate (HM) and PRVI, are generally moving NNE relative to the NAP. However, the PRVI is moving more northeasterly and relatively faster than the HM (Mann, 2005a; ten Brink and López-Venegas, 2012; Benford et al., 2012). The direction and rate of the HM movement are altered due to the existence of the Bahamas Carbonate Platform to the north (Fig. 1.1), which in turn generates resistance to subduction of the NASS beneath the northern HM. In addition, we interpret the faster rate of NE movement in the eastern PRVI relative to the area west of the MR (Rogers and Mann, 2007) is causing the rifting along the Mona Passage. The cause of variation is crust of PRVI moving eastward due to larger scale plate movement to the east of the study area.

CONCLUSIONS

We created a 3D tectonic cartoon to better illustrate the geometric relationships between the Greater Antilles and adjacent areas regarding the variations in subduction between the North American and North Caribbean plates and the resulting kinematic evolution (Fig. 1.8). This is the first time that integrated tomographic imaging and 2-D gravity modeling across both the PRVI and the two bounding subduction zones has been employed to refine their geometry and tectonic evolution. Our analysis provides details on the geometry of the subducting slab of the eastern NCSS and its interactions with the PRVI. Our results indicate that the NASS experiences slab roll back and an increase in the dip of the subduction zone from east to west. These variations cause the dip angle of the NCSS to also increase westward, which in

agreement with distribution of earthquake hypocenters. The active boundaries of this microplate are the sources of seismic activity in this region, i.e. the Puerto Rico Trough to the north and the Muertos Trough to the south, and the Anegada Trough rifting zone to the east, and the Mona Passage rifting region to the west. All regions have potential events greater than M7.0 according to the recorded history of the island (Ascencio, 1980; Moya and McCann, 1992; Macari, 1994). Large landslide scraps and cliffs near the Puerto Rico Trench and Muertos Trough could be the potential sources of tsunami risk on both sides of Puerto Rico Island (Grindlay et al., 2005a; Grindlay et al., 2005b; ten Brink, 2004). Especially, the north of the island is particularly severe. The deepest part of the Puerto Rico Trench drops to 8.3 km northwest of the island. The distributions of earthquakes are in 3 regions, one in the north of the Puerto Rico Island, one in the north of Virgin Island (both of them are in the south of the Puerto Rico Trench), and the third one is in the southwest of the island. The results of this research should contribute to understanding the kinematic evolution of the PRVI and the associated natural hazards.

Table 1.1. Initial 1-D P wave velocity model.

Vp(km/s)	Top of Layer (km)
6.45	-5
7.13	17
8.01	31

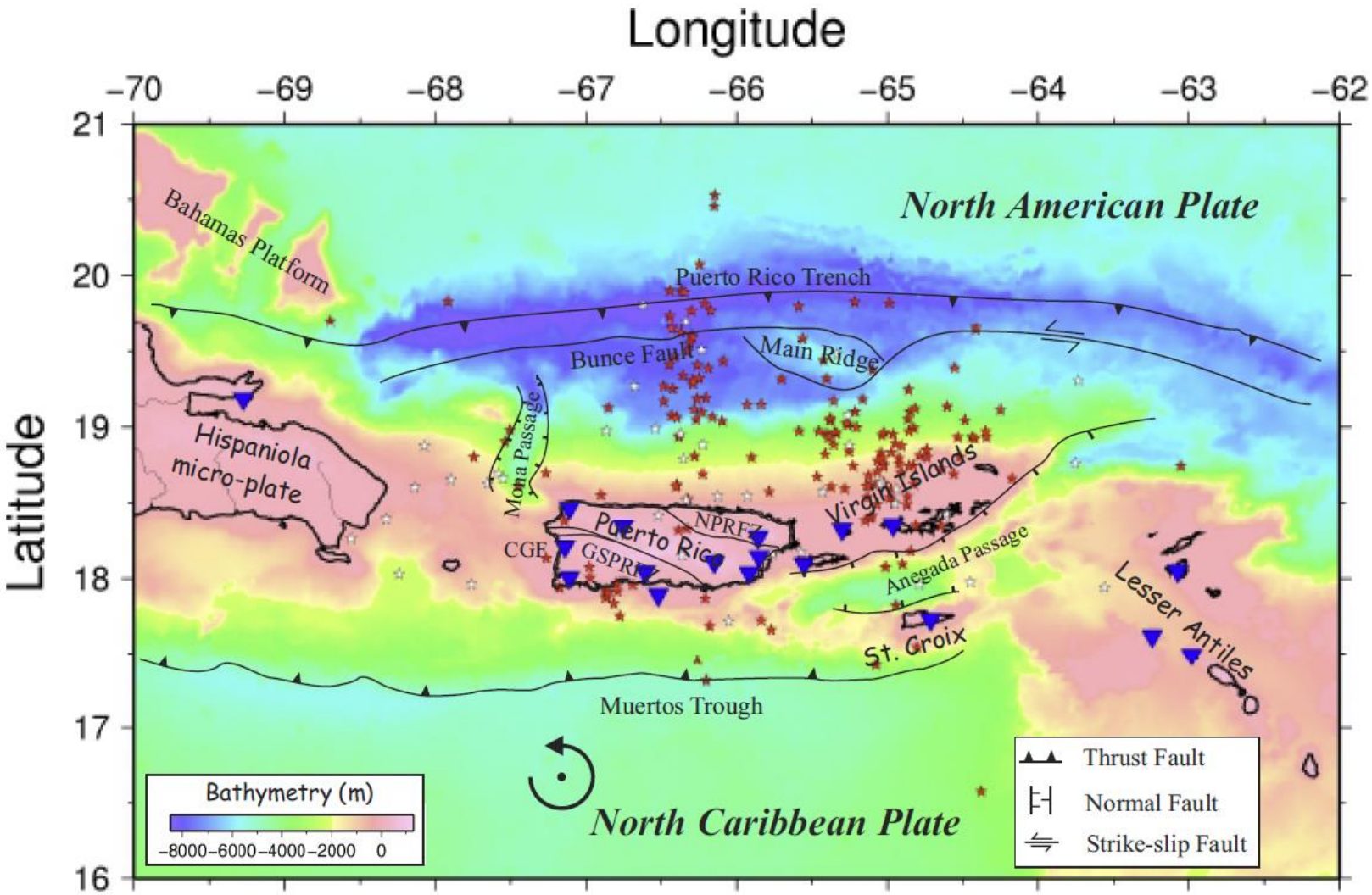
Longitude
−70
−69
−68
−67
−66
−65
−64
−63
−62
Latitude
21
20
19
18
17
16
North American Plate
Bahamas Platform
Puerto Rico Trench
Bunce Fault
Main Ridge
Hispaniola
micro-plate
Mona Passage
Puerto Rico
NPRFZ
CGF
GSPRF
Virgin Islands
Anegada Passage
St. Croix
Lesser Antiles
Muertos Trough
North Caribbean Plate
Bathymetry (m)
−8000 −6000 −4000 −2000 0
Thrust Fault
Normal Fault
Strike-slip Fault

Figure 1.1. Bathymetry map overlain with tectonic features along the northern margin of the Caribbean Plate (modified after ten Brink et al. 2009 and Granja Bruña et al., 2009, ten Brink and López-Venegas, 2012). Black solid lines are fault zones; blue triangles are broadband stations; red circles are earthquakes shallower than 20km and white circles are earthquakes deeper than 20km; black dot with arrow is the rotation pole. GSPRFZ: Great Southern Puerto Rico fault zone; GNPRFZ: Great North Puerto Rico fault zone; CGF: Cerro Goden fault.

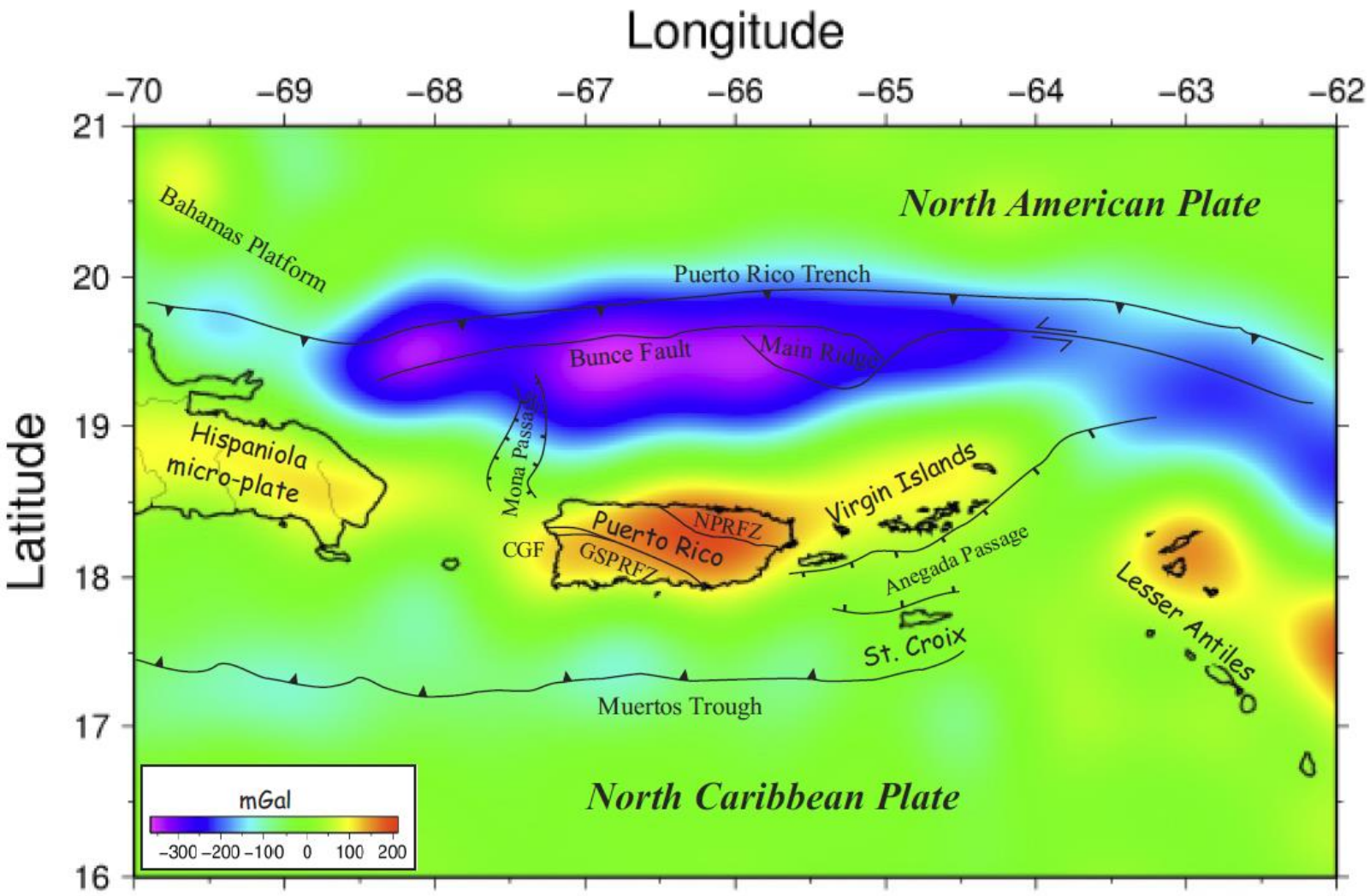

Figure 1. 2. Free Air gravity anomaly

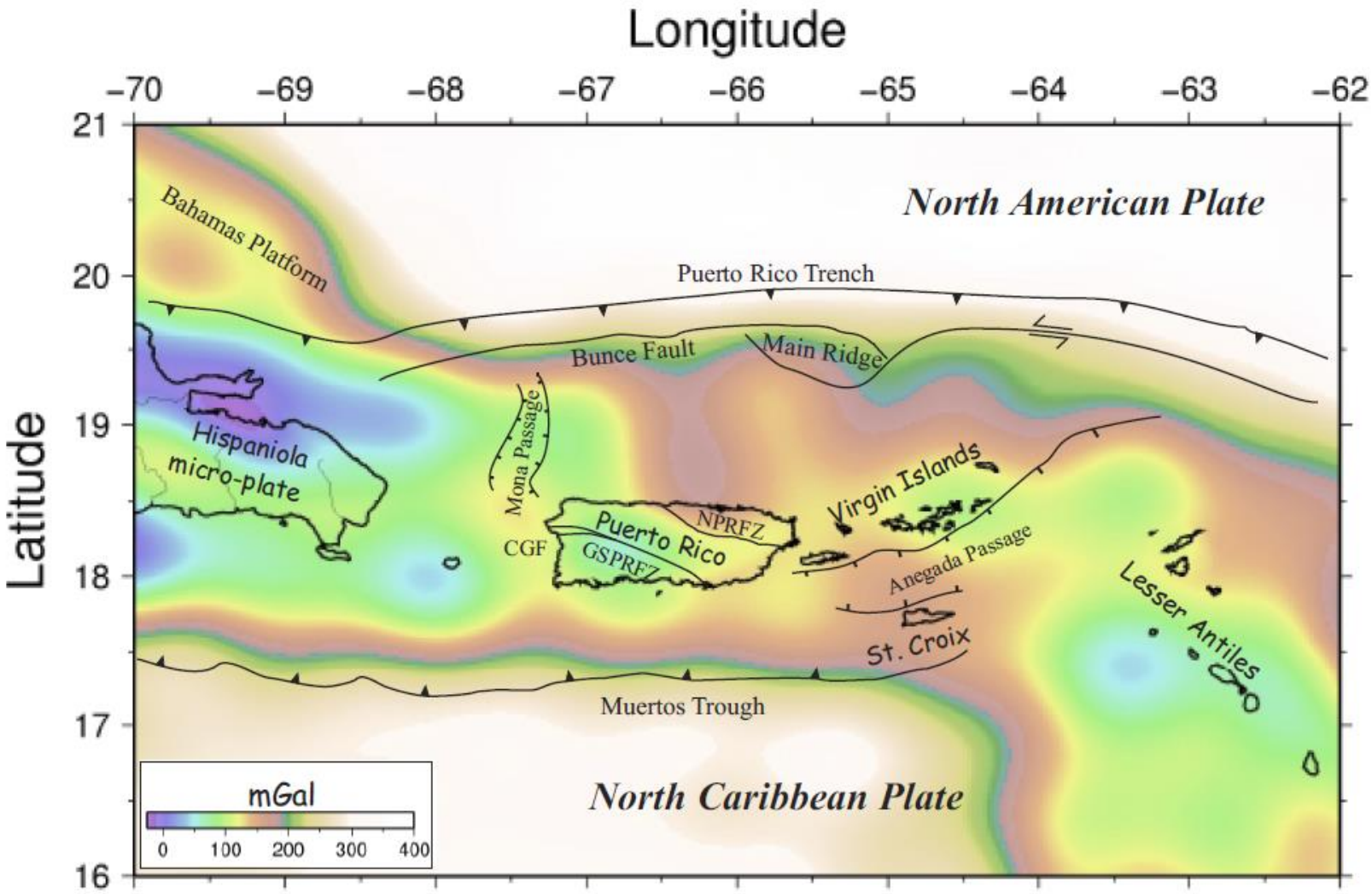

Figure 1.3. Simple Bouguer Anomaly with 30km upward continuation after traditional approach (see text).

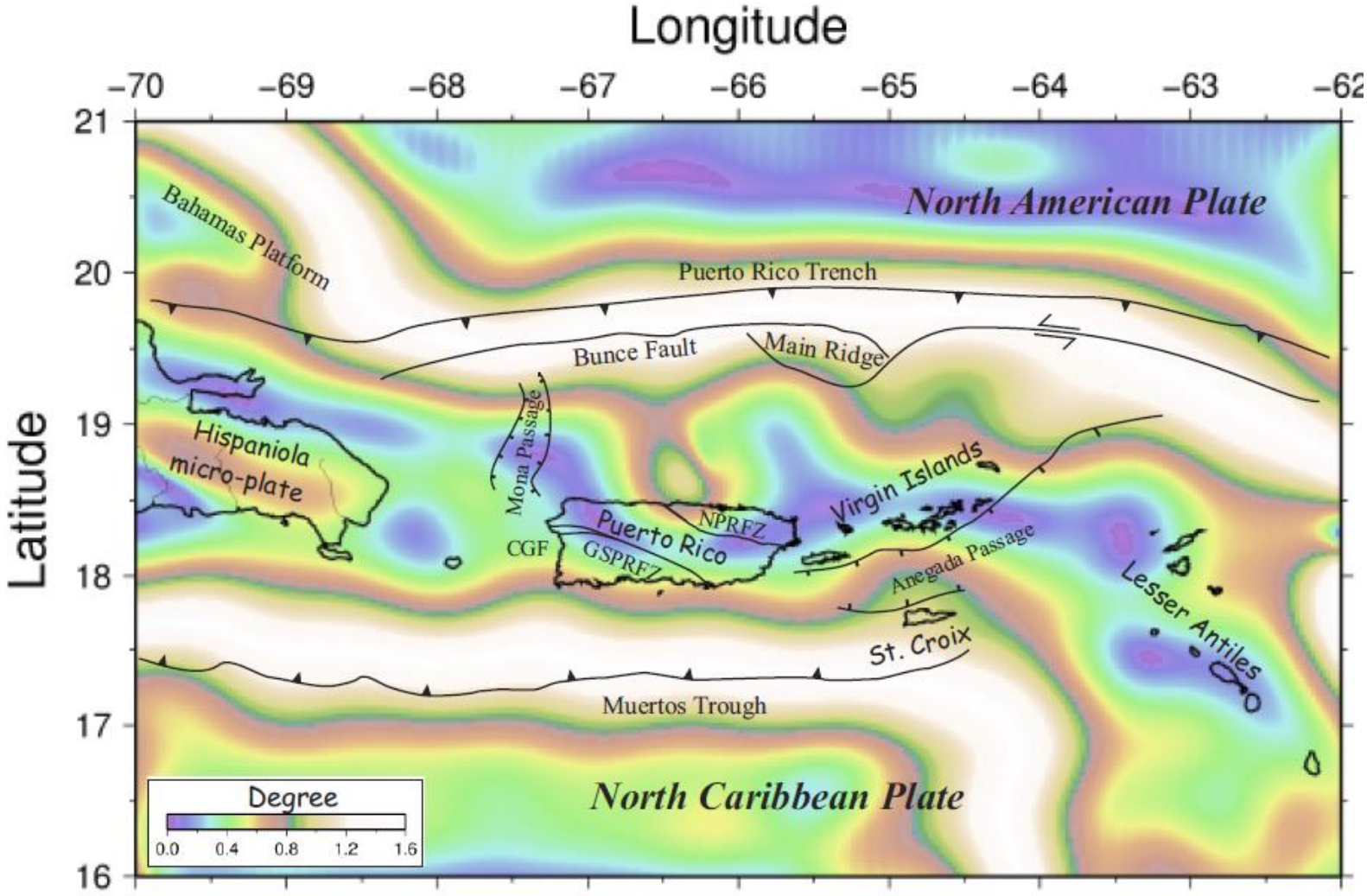

Figure 1.4. Tilt derivative map of the simple Bouguer anomaly with 30km upward

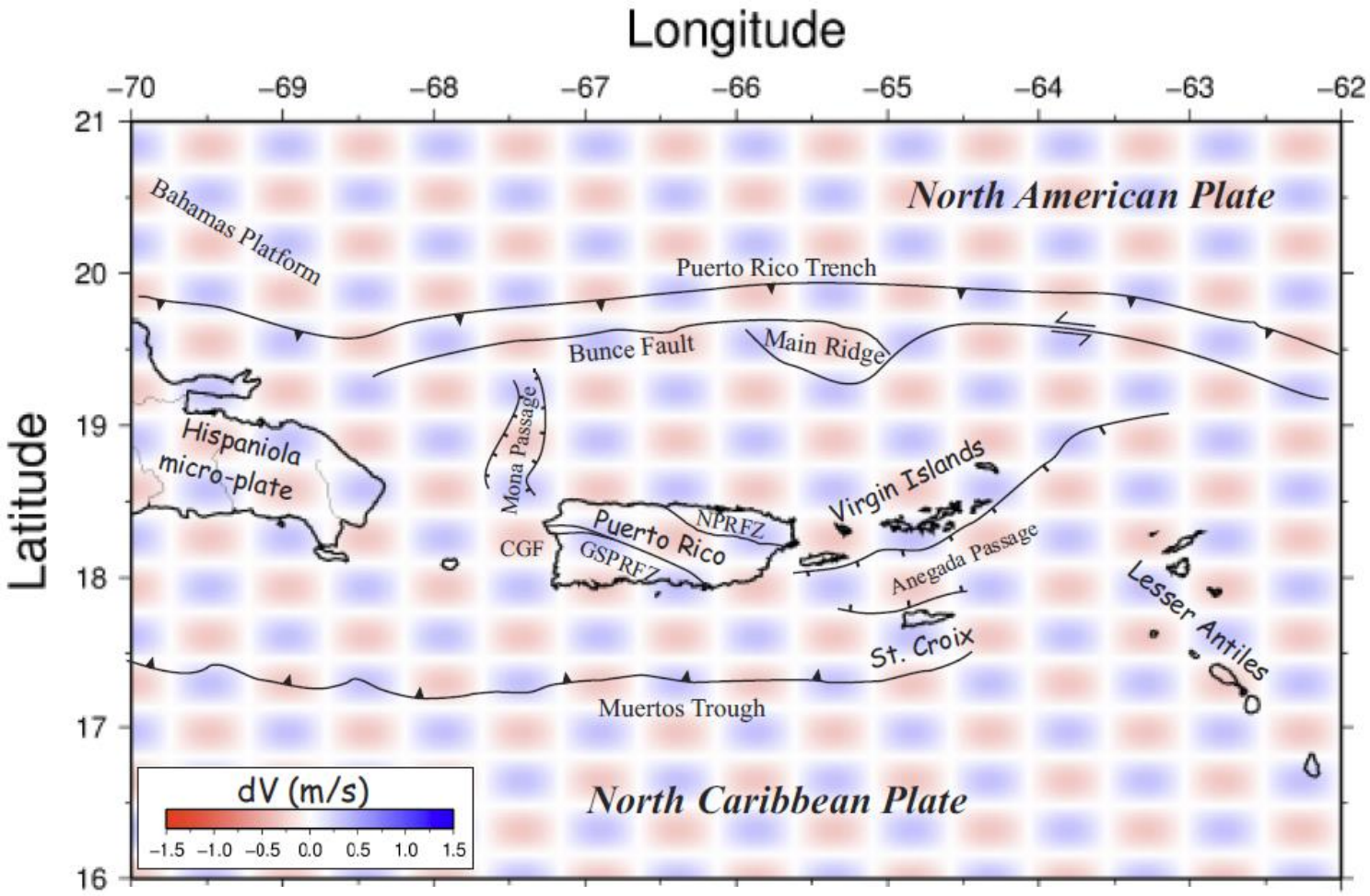

Figure 1.5. Checkerboard resolution tests for the travel-time tomography, A) Horizontal slice through the retrieved model (10km depth). Positive and negative velocity perturbations are

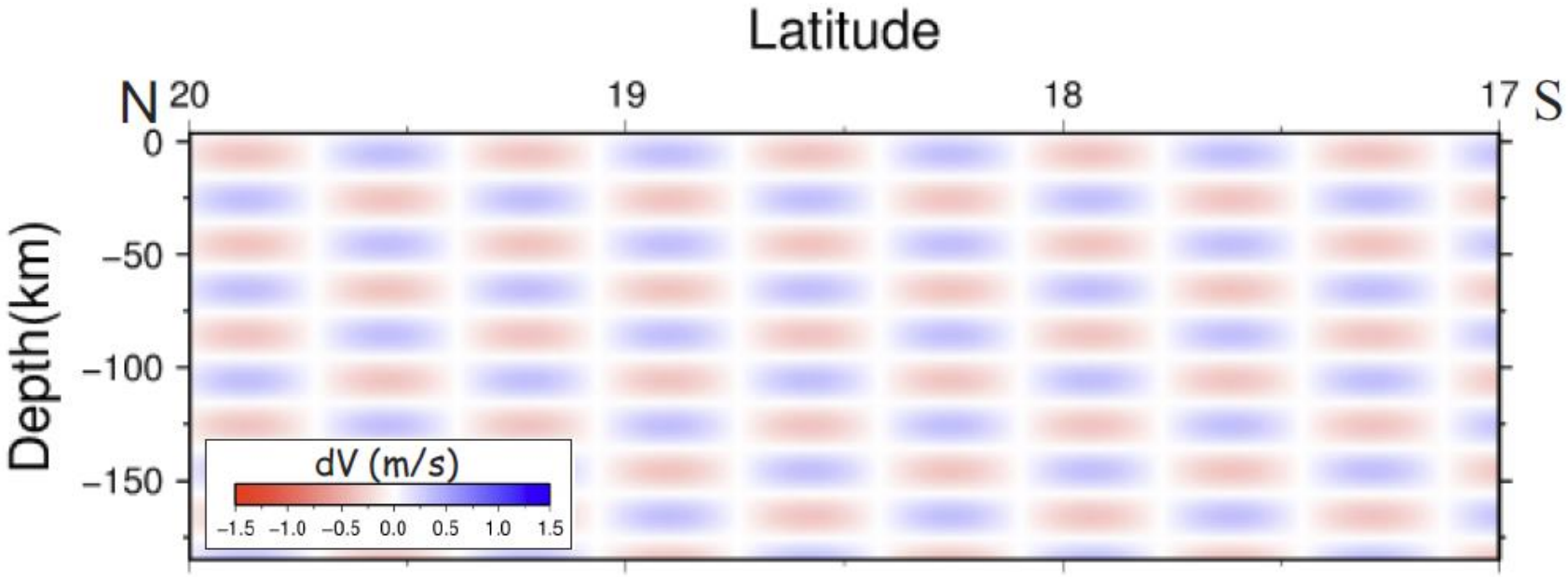

Figure 1.5. Checkerboard resolution tests for the travel-time tomography, B) A vertical slice through the retrieved model (67^{o} W).

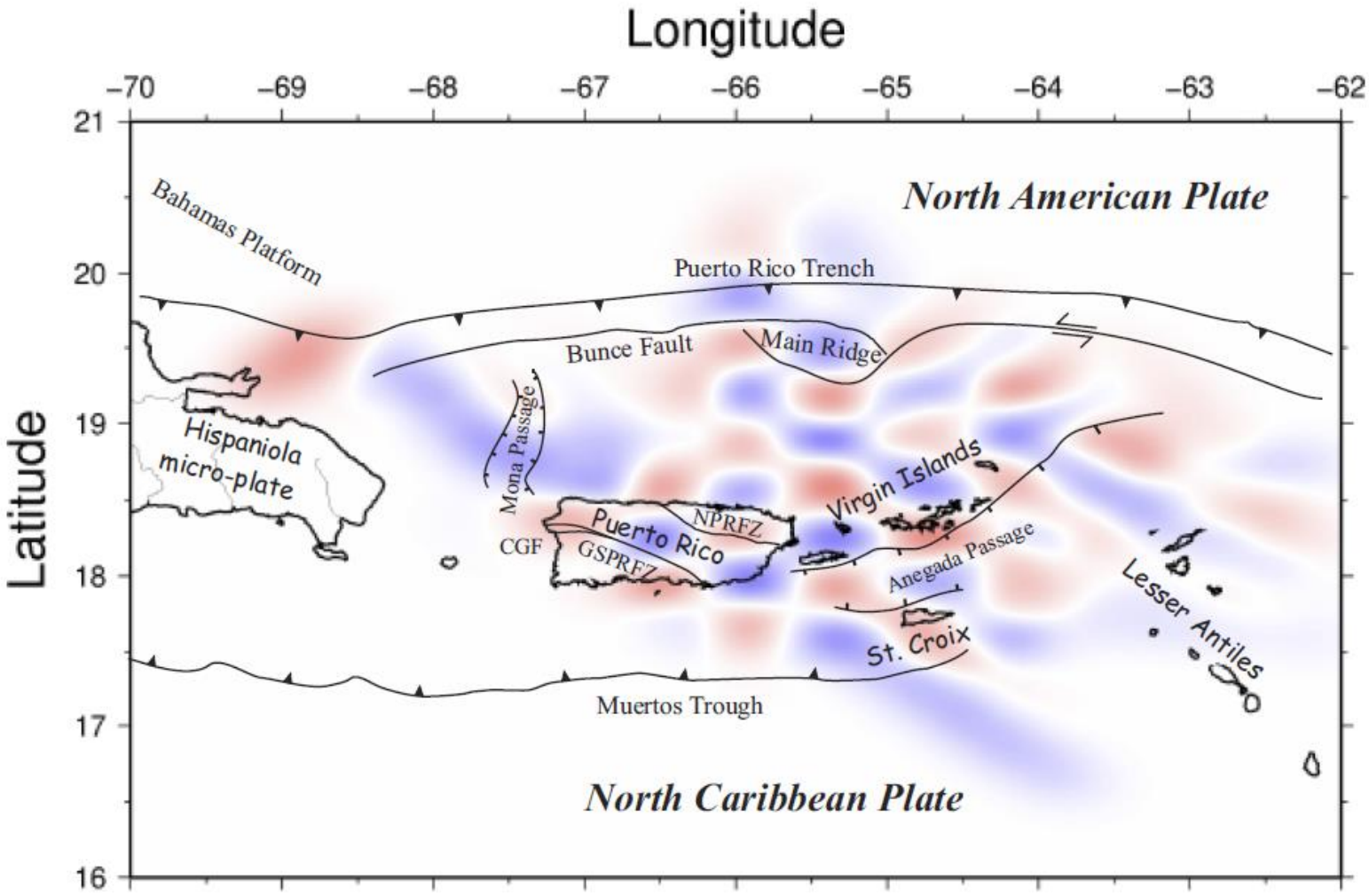

Figure 1.5. Checkerboard resolution tests for the travel-time tomography, C) Checkerboard resolution tests tomographic inversion at 10km depth.

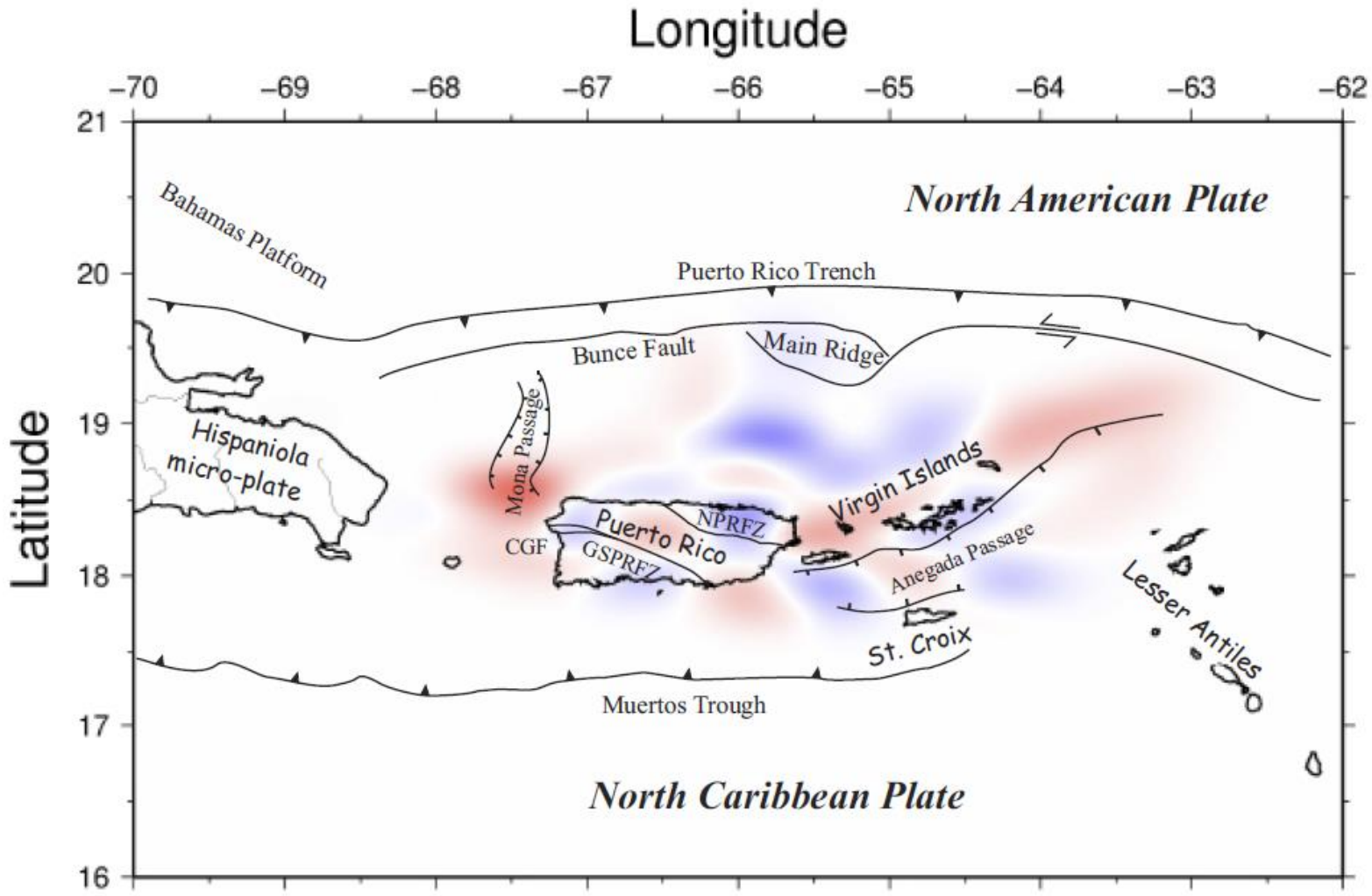

Figure 1.5. Checkerboard resolution tests for the travel-time tomography, D) tomographic inversion at 30km depth.

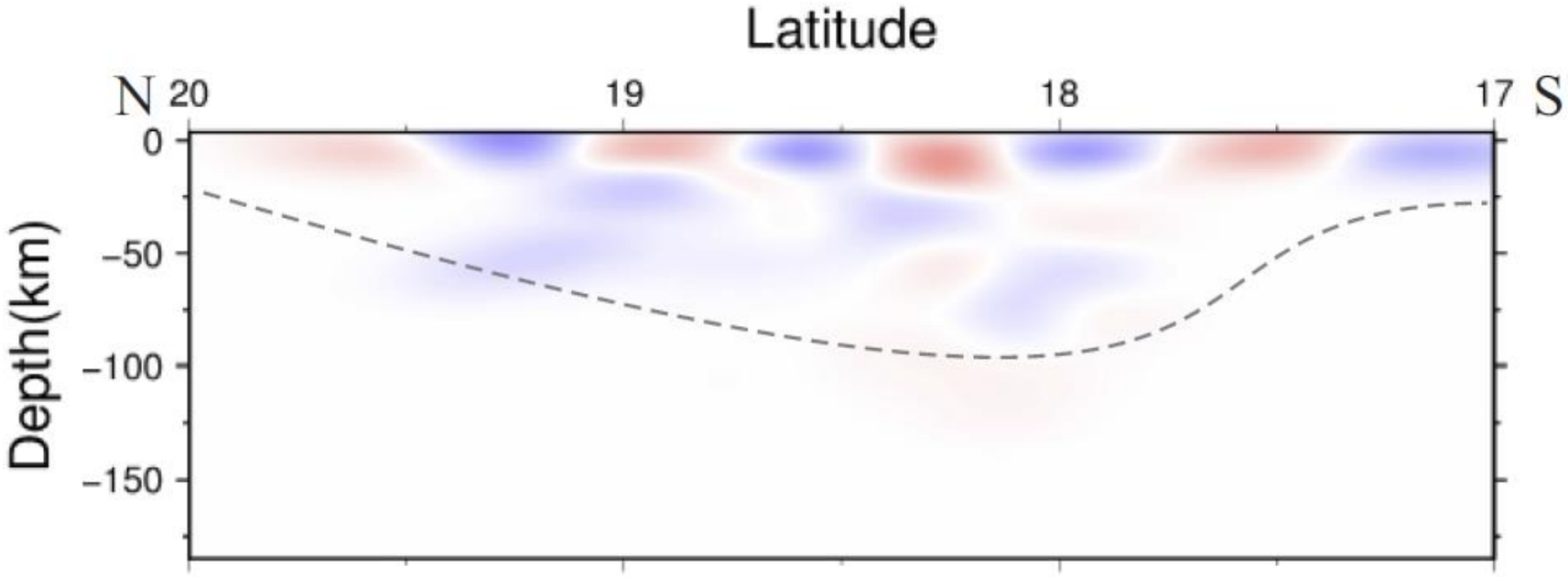

Figure 1.5. Checkerboard resolution tests for the travel-time tomography, E) tomographic inversion 65^{o} W. The variations of velocities above the dashed lines in our checkerboard test

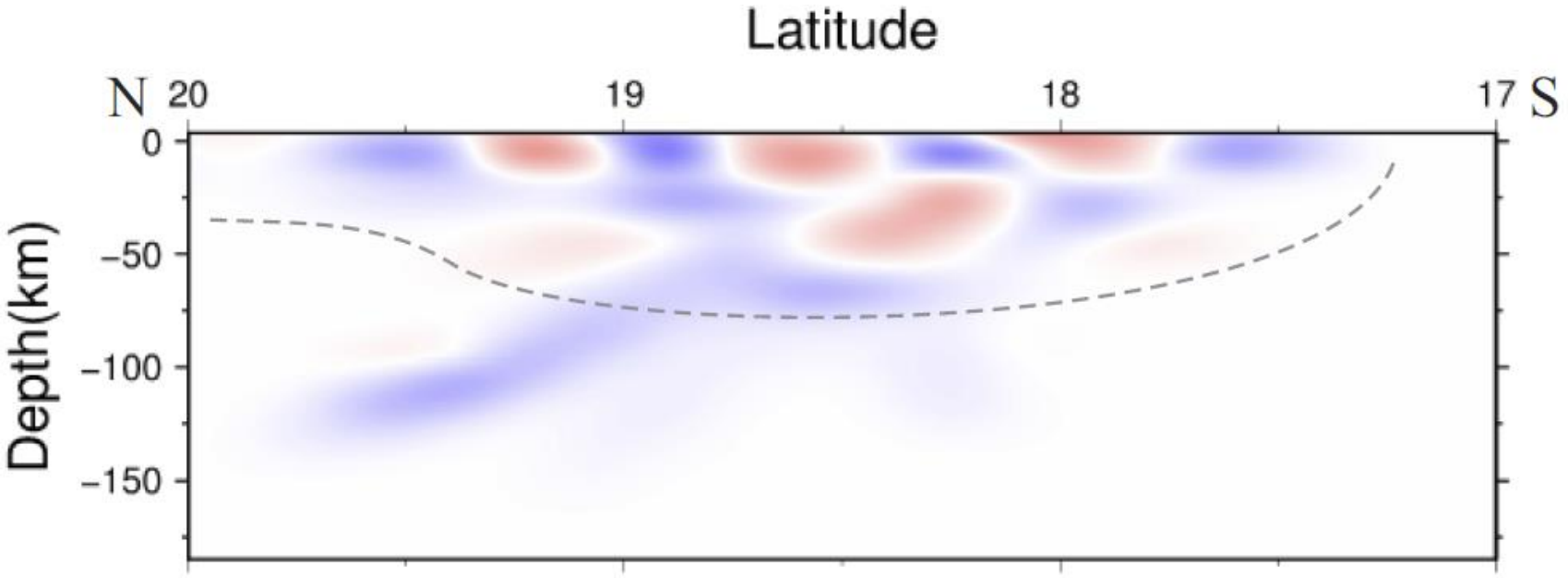

Figure 1.5. Checkerboard resolution tests for the travel-time tomography, F) tomographic inversion 66^{o} W.

The variations of velocities above the dashed lines in our checkerboard test results are reliable.

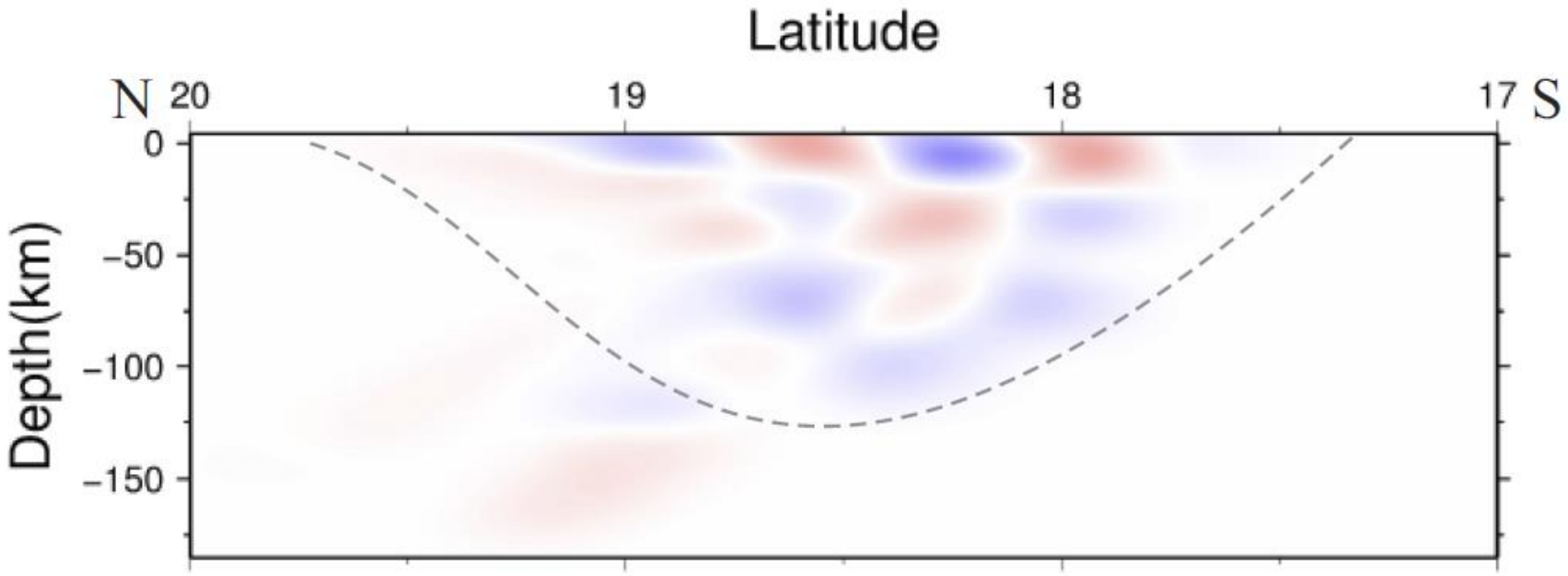

Figure 1.5. Checkerboard resolution tests for the travel-time tomography, G) tomographic inversion 67^{o} W.

The variations of velocities above the dashed lines in our checkerboard test results are reliable.

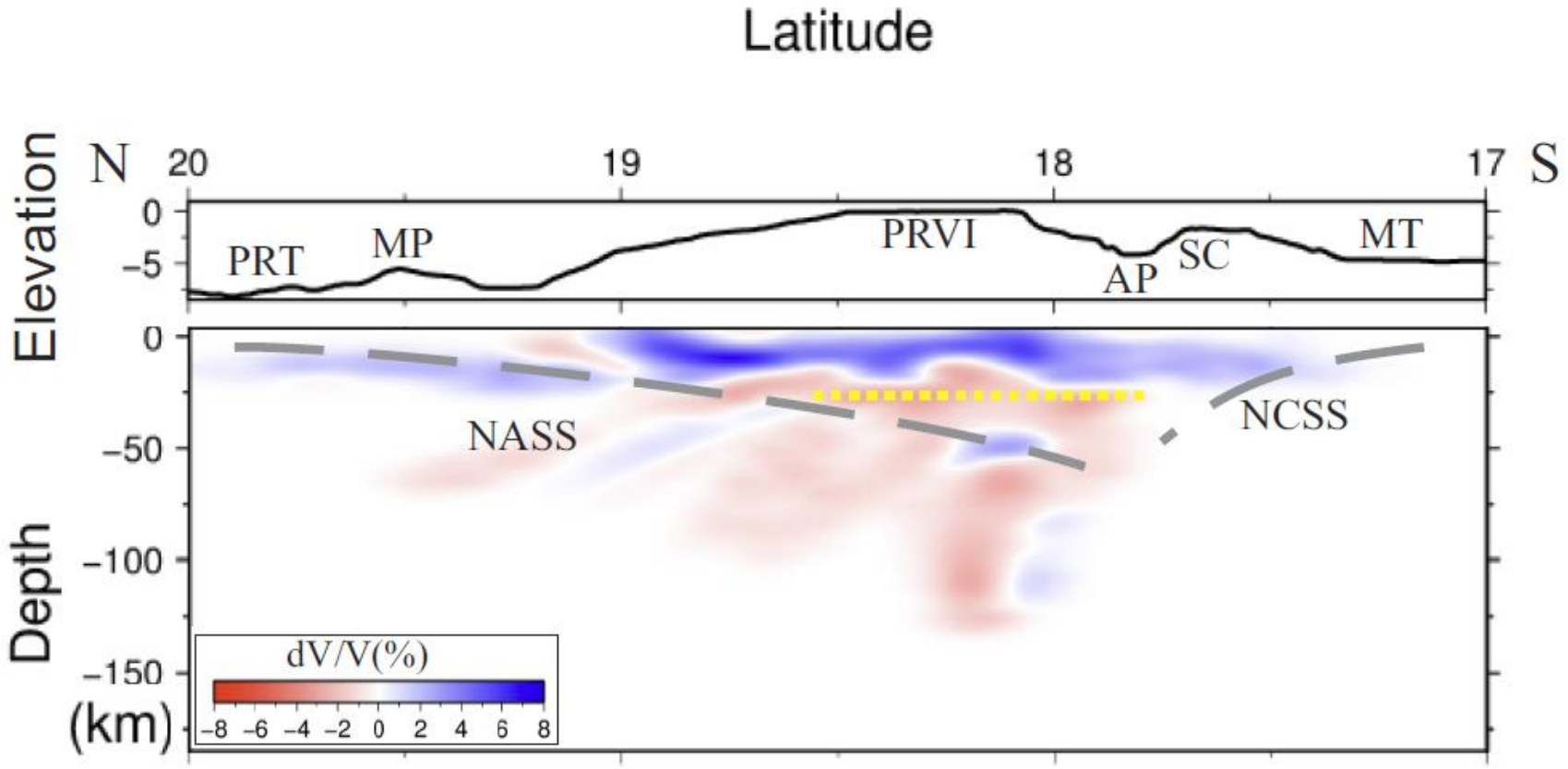

Figure 1.6. A) N to S profiles of the P wave model at 65.5°W. Gray dashed lines are the top of the subducting slabs, and yellow dashed lines are the estimated positions of the Moho (Lin and Huerfano, 2011), PRT: Puerto Rico Trench, MP: Mona Passage, PRVI: Puerto Rico Virgin Island, AP: Anegada Passage, MT: Muertos Trough, NASS: North American subducting slab, NCSS: North Caribbean Subducting slab, SC: St. Croix.

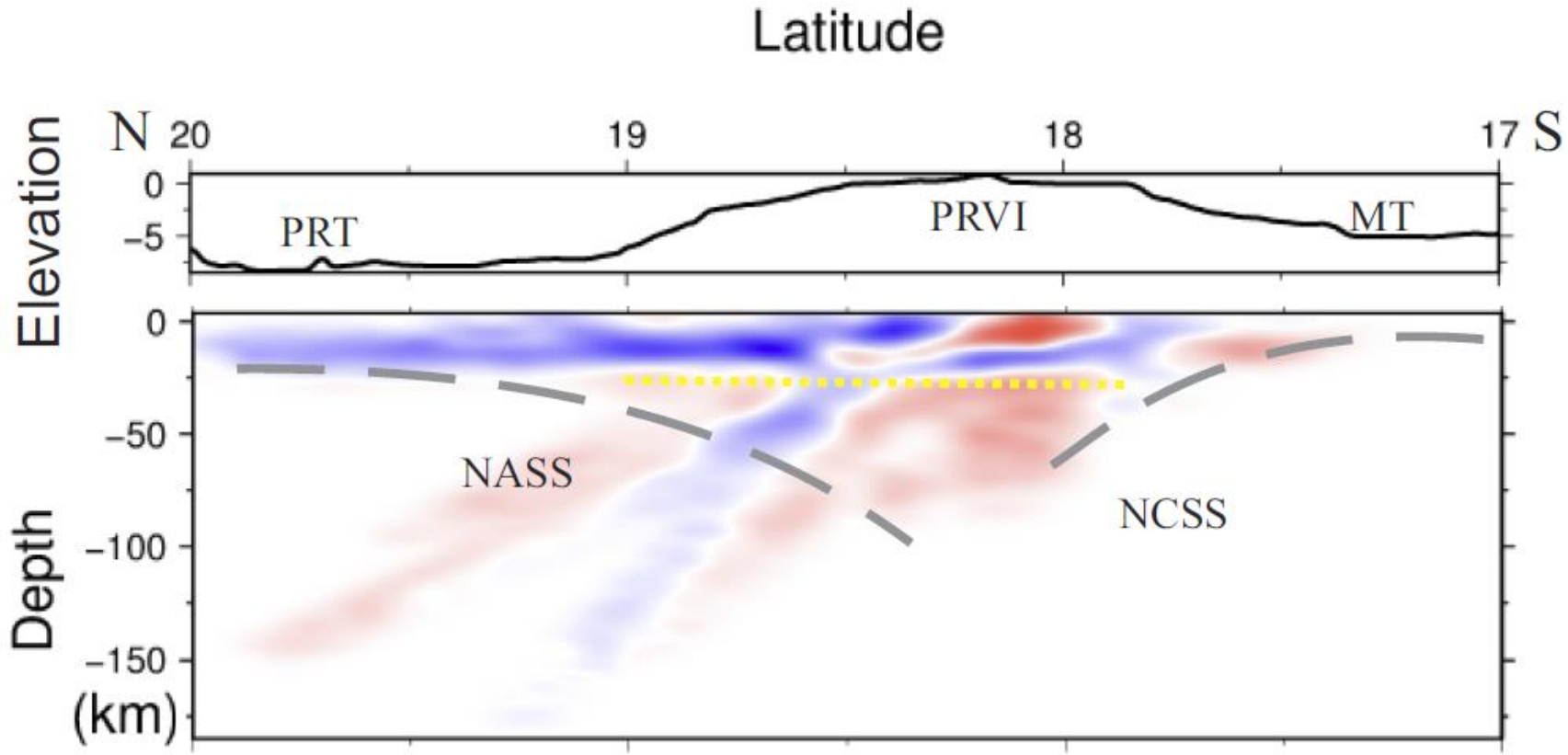

Figure 1.6. B) N to S profiles of P wave model at 66.5^{o} W

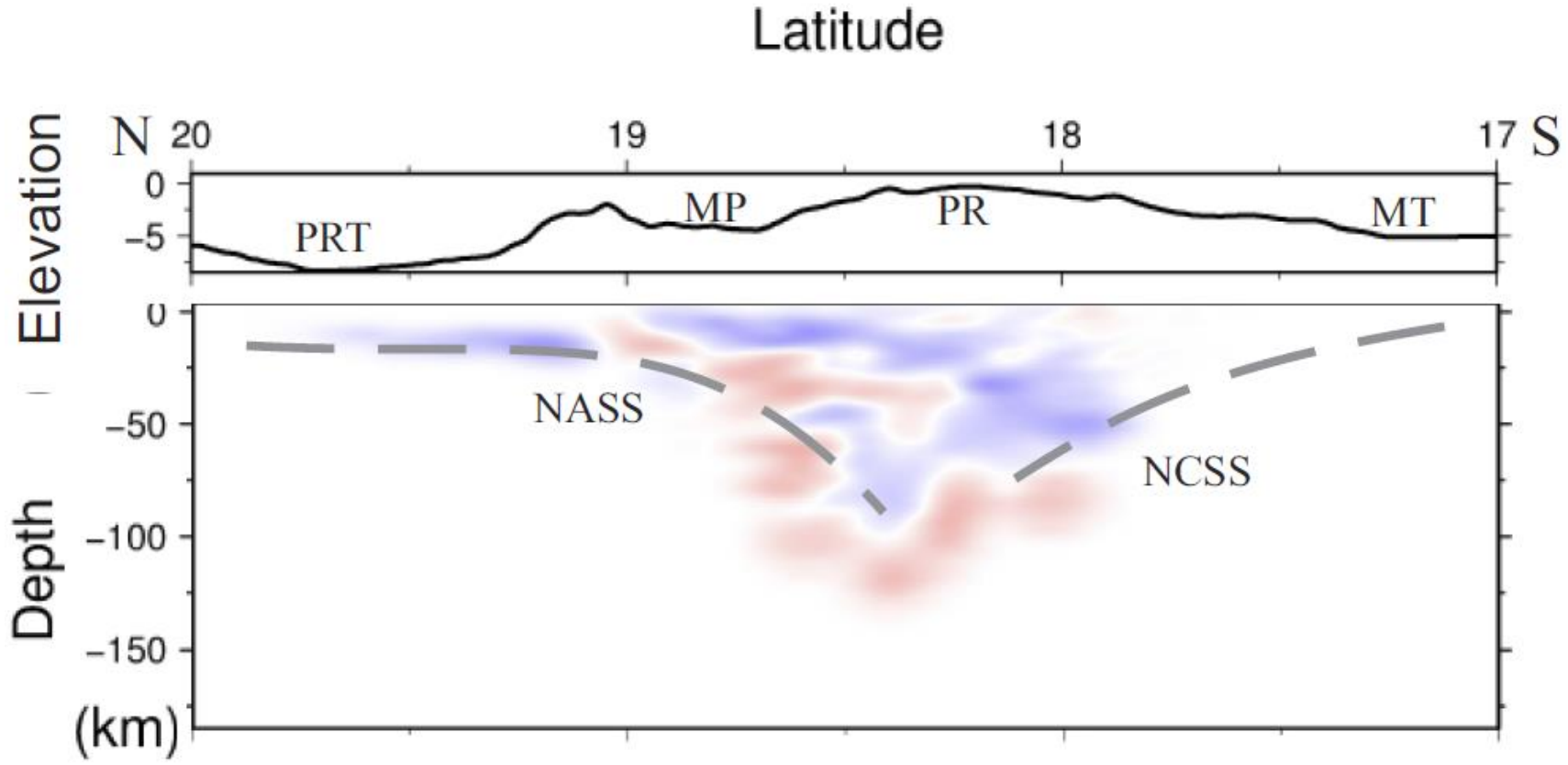

Figure 1.6. C) N to S profiles of P wave model at 67.5° W.

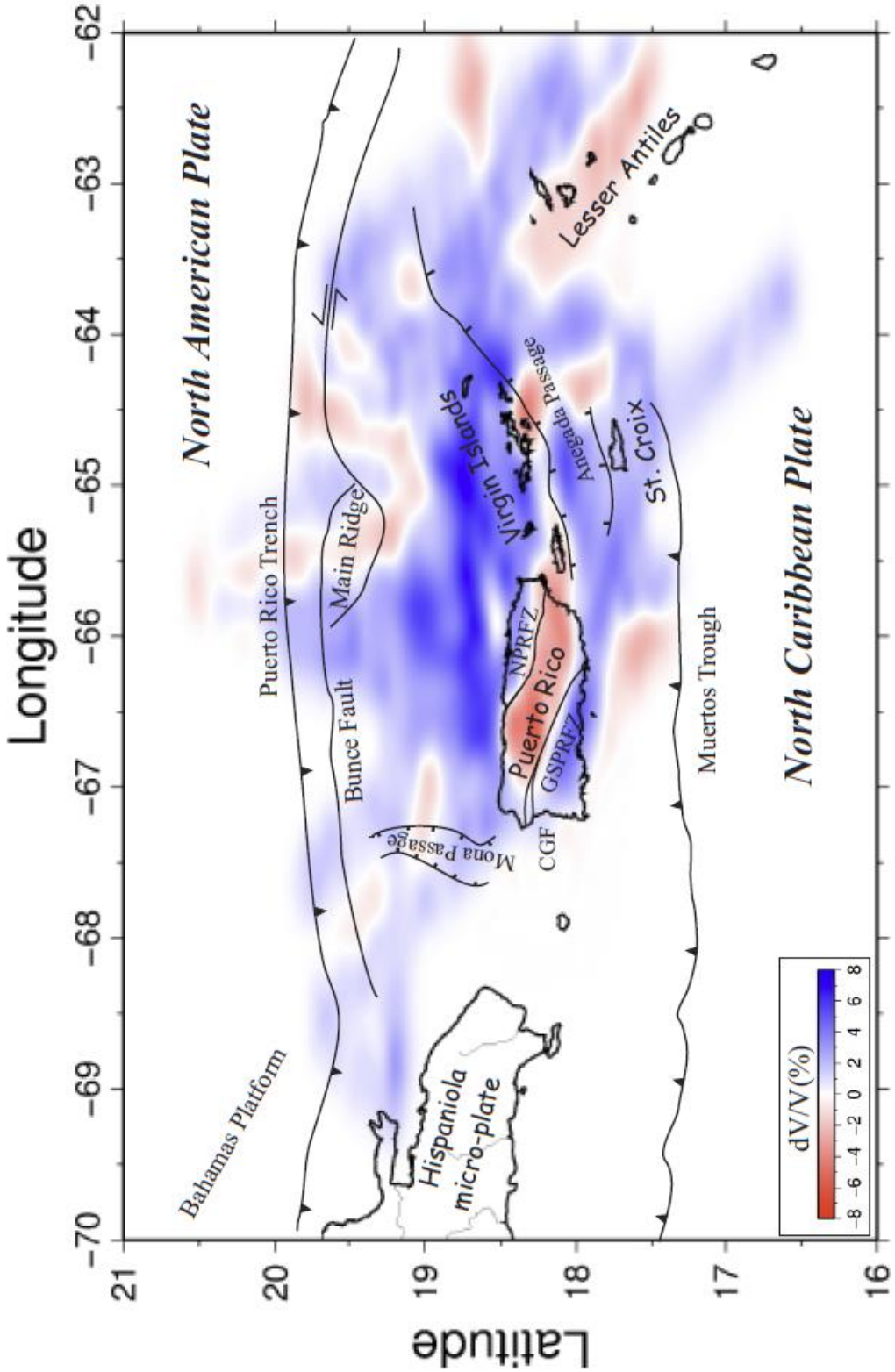

Figure 1.6. D) P wave tomography at 10km

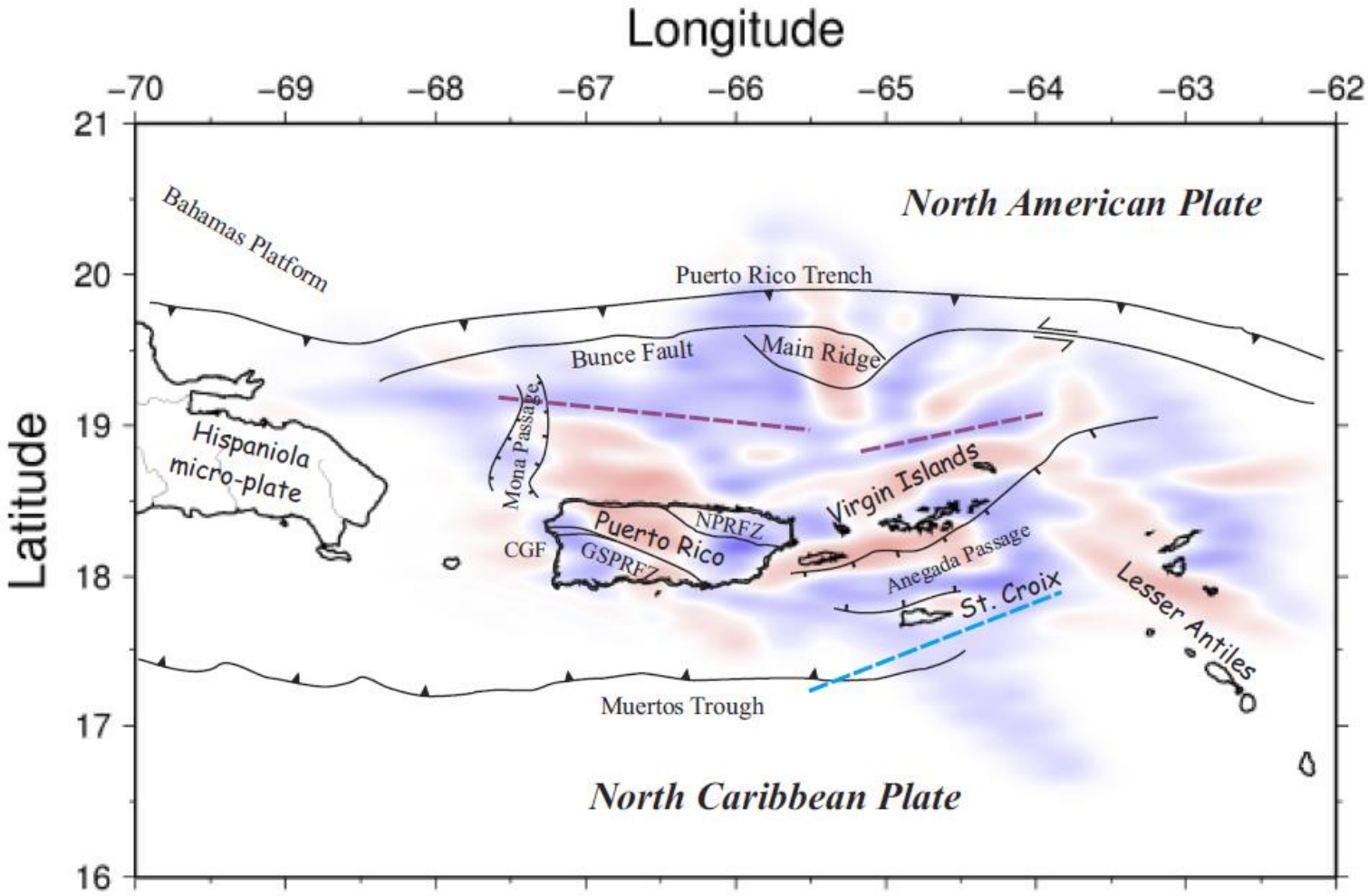

Figure 1.6. E) P wave tomography at 20km depth. Red dashed lines are the edge of NASS at this depth, and the blue dashed line is edge of NCSS at this depth.

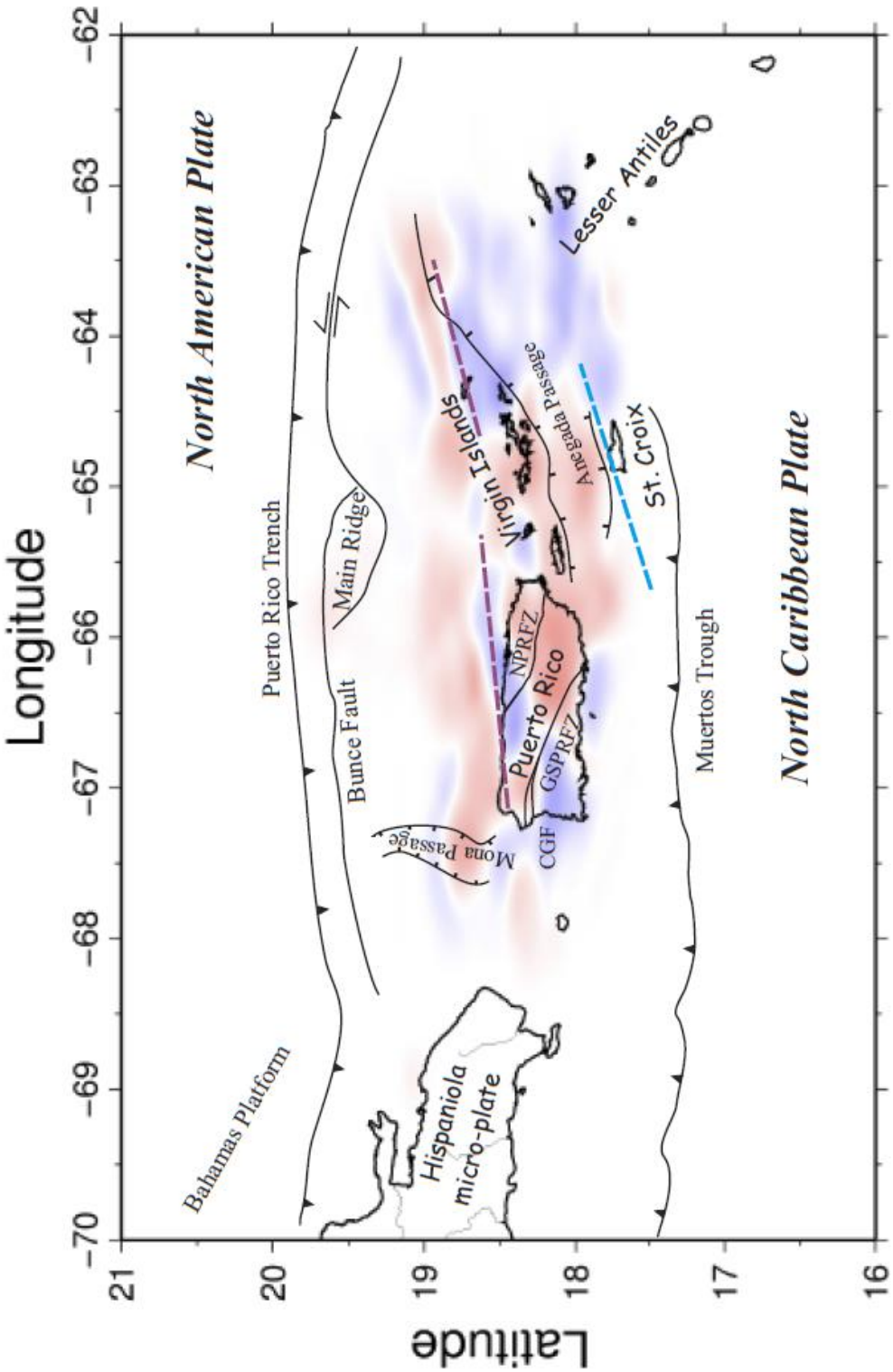

Figure 1.6. F) P wave tomography at 30km

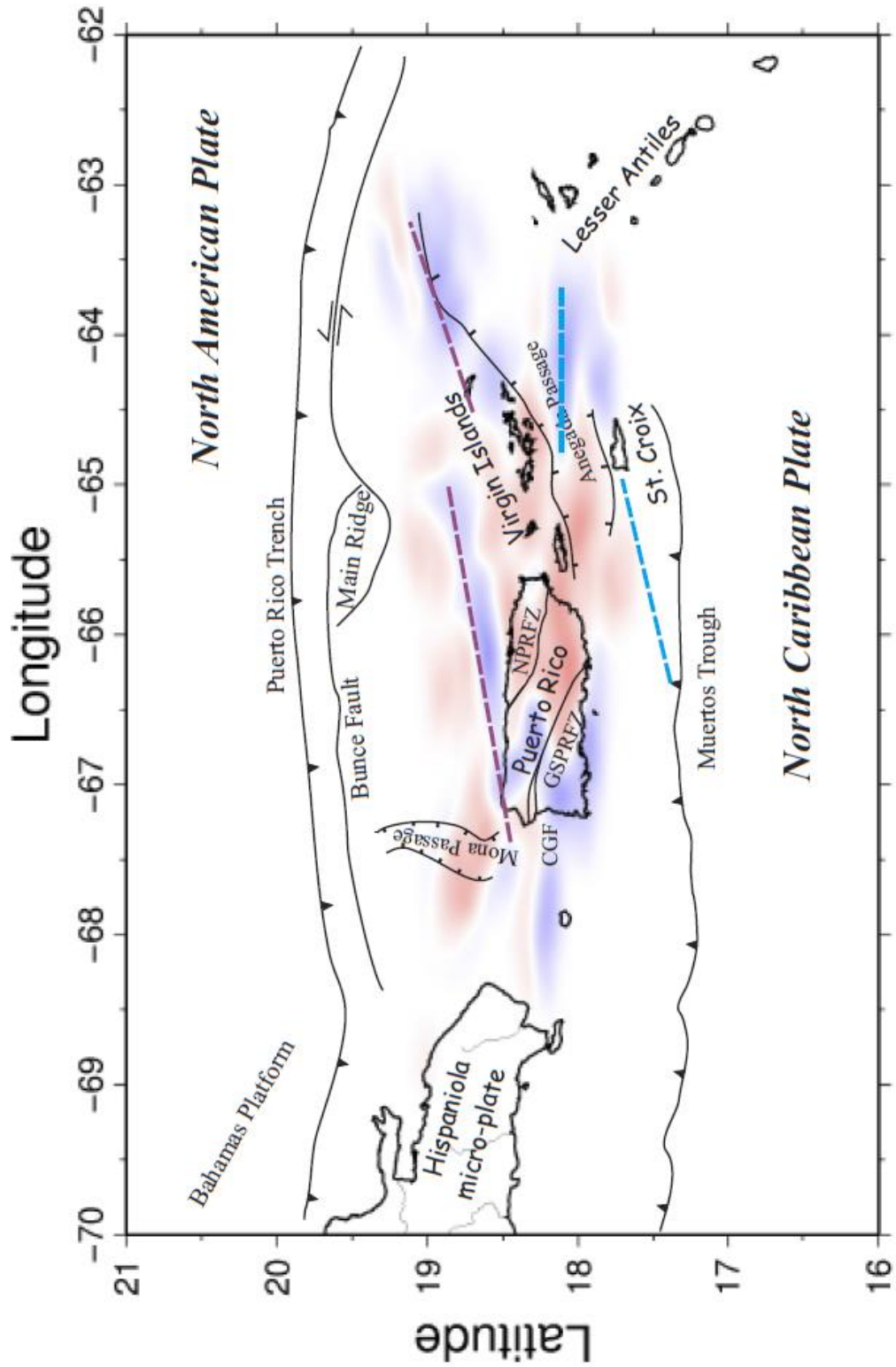

Figure 1.6. G) P wave tomography at 40km

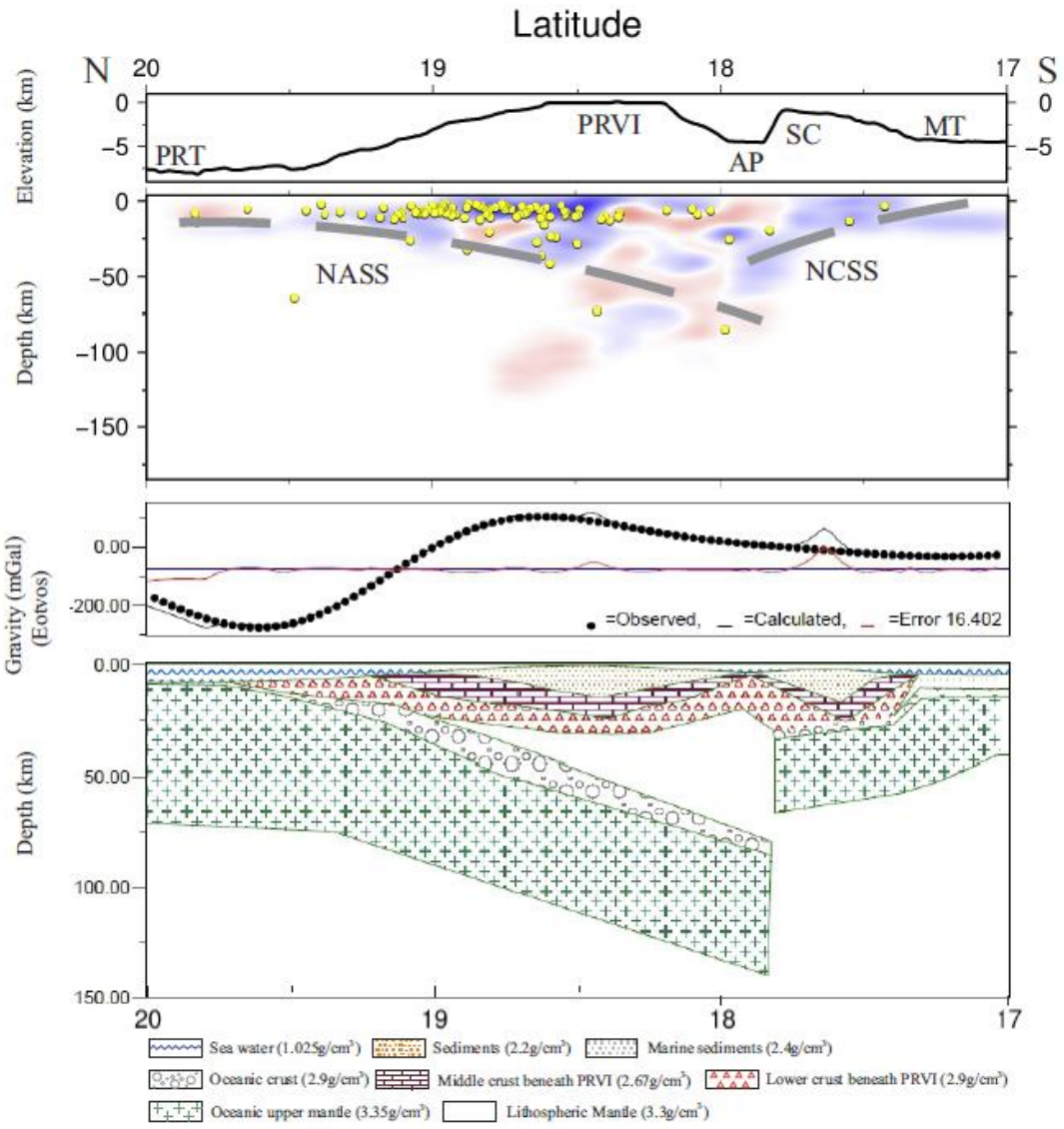

Figure 1.7. A) N to S vertical slice through the P wave tomographic model and a gravity model at 65°W. From top to bottom: Bathymetry, P wave tomography, Error of gravity model and 2-D gravity model. Gray dashed lines are interpreted tops of the subducting slabs. Yellow dots are earthquakes. PRT: Puerto Rico Trench, MP: Mona Passage, PRVI: Puerto Rico Virgin Island, AP: Anegada Passage, MT: Muertos Trough, NASS: North American subducting slab, NCSS: North Caribbean Subducting slab, SC: St. Croix.

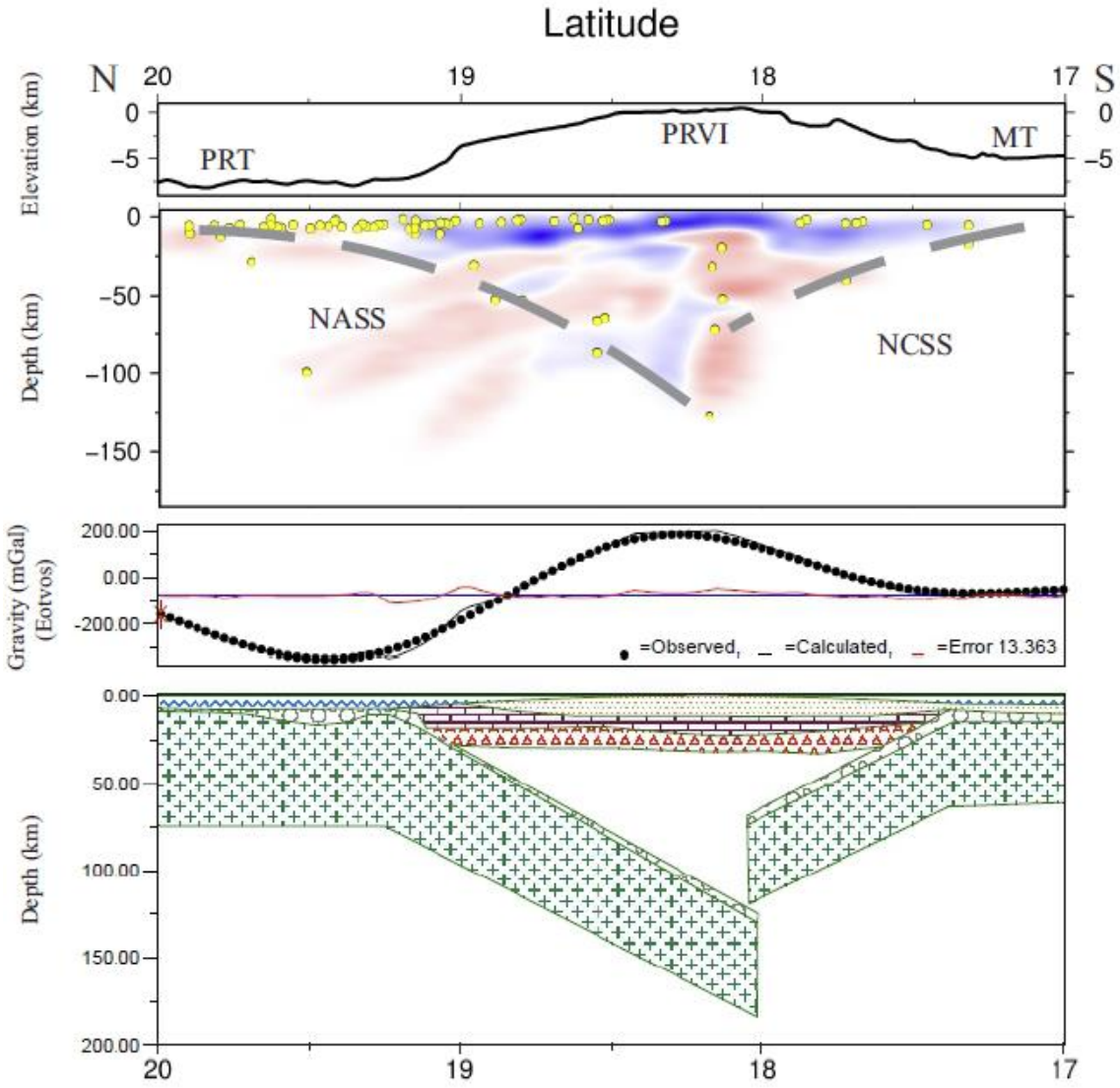

Figure 1.7. B) N to S vertical slice through the P wave tomographic model and a gravity model at 66°W. From top to bottom: Bathymetry, P wave tomography, Error of gravity model and 2-D gravity model. Gray dashed lines are interpreted tops of the subducting slabs. Yellow dots are earthquakes. PRT: Puerto Rico Trench, MP: Mona Passage, PRVI: Puerto Rico Virgin Island, AP: Anegada Passage, MT: Muertos Trough, NASS: North American subducting slab, NCSS: North Caribbean Subducting slab, SC: St. Croix.

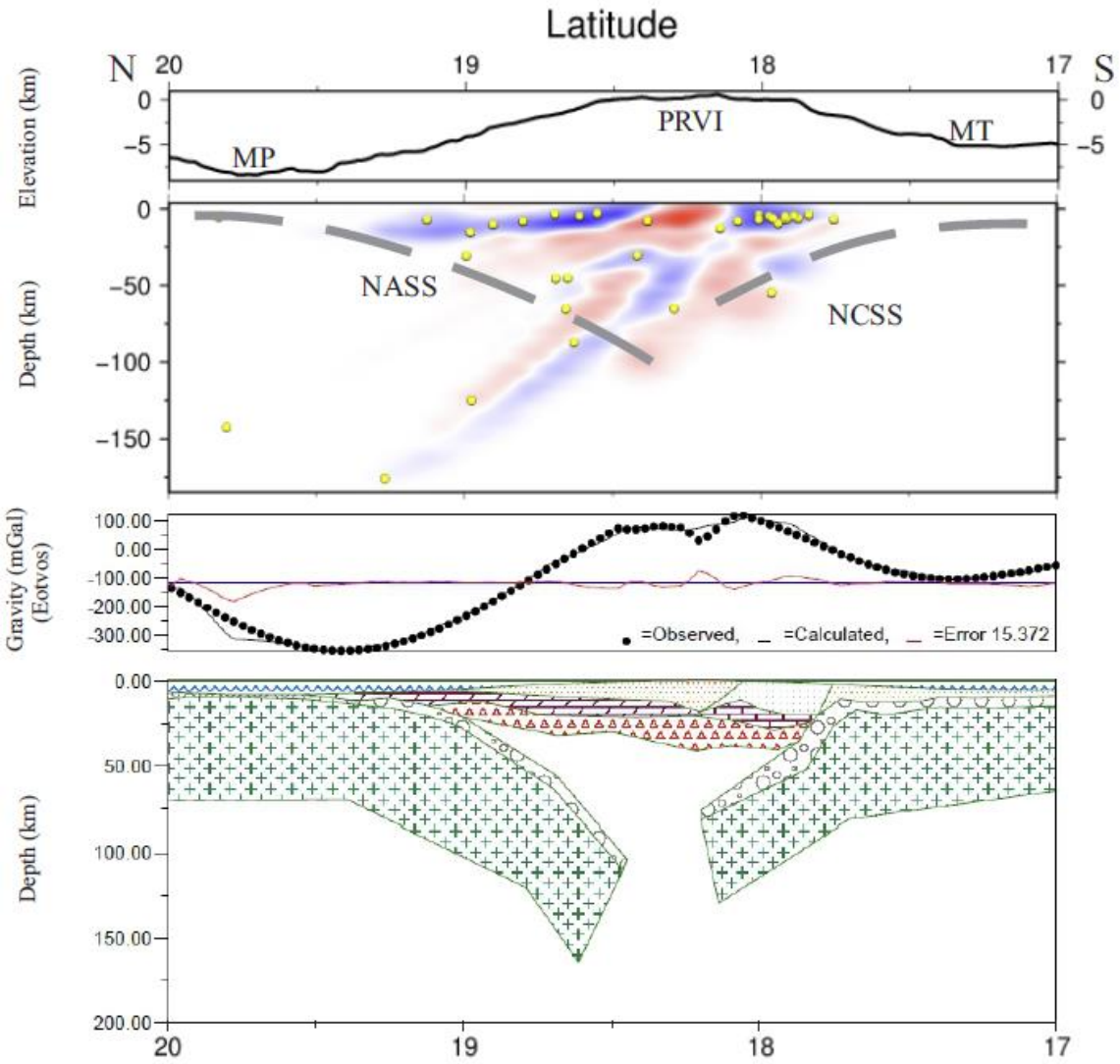

Figure 1.7. B) N to S vertical slice through the P wave tomographic model and a gravity model at 66°W. From top to bottom: Bathymetry, P wave tomography, Error of gravity model and 2-D gravity model. Gray dashed lines are interpreted tops of the subducting slabs. Yellow dots are earthquakes. PRT: Puerto Rico Trench, MP: Mona Passage, PRVI: Puerto Rico Virgin Island, AP: Anegada Passage, MT: Muertos Trough, NASS: North American subducting slab, NCSS: North Caribbean Subducting slab, SC: St. Croix.

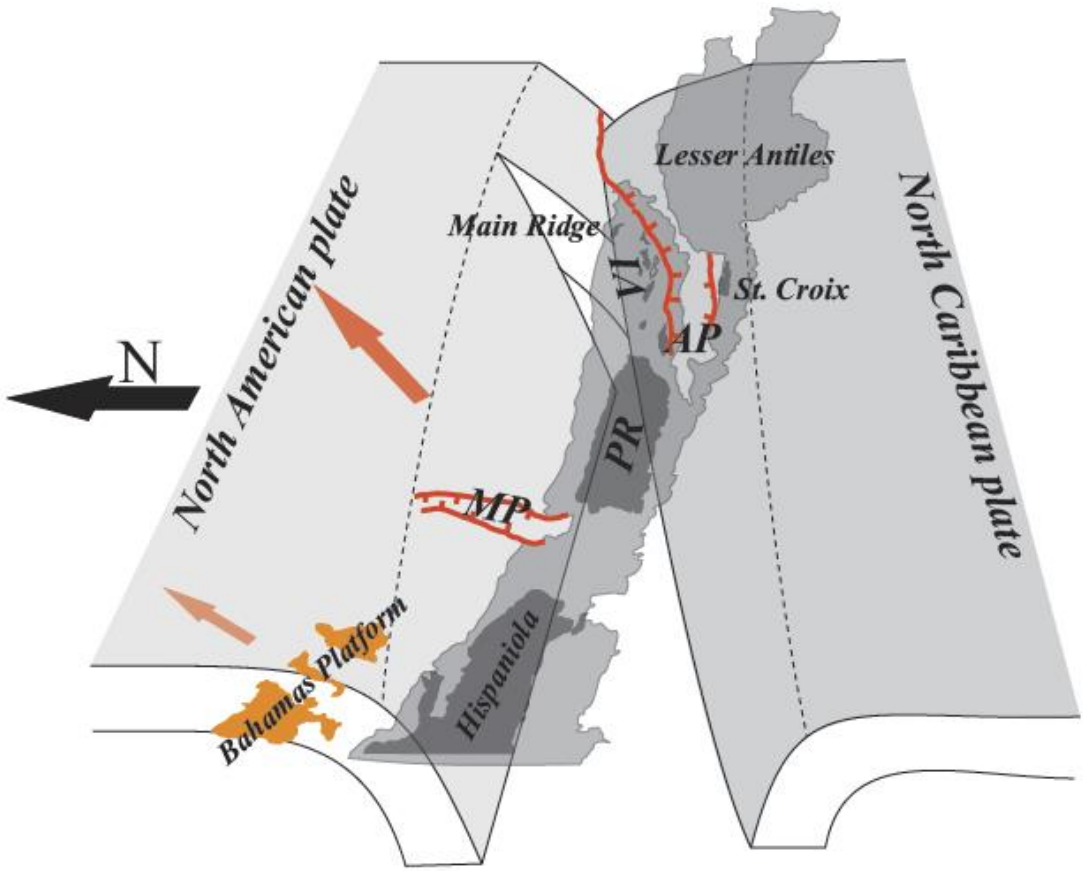

Figure 1.8. Hypothesized model; the PRVI sits between two subducting slabs, the dip angles of the two subducting slabs increase from east to west. The North American plate splits in the eastern PRVI (modified after ten Brink, 2005). North arrow is black. Brown arrows show the moving directions of PRVI and HM respect to the North American Plate. The light gray area in central is above 2km bathymetry line. MP: Mona Passage, PRVI: Puerto Rico Virgin Island, AP:

REFERENCES CITED

Ascencio, E., 1980, Western Puerto Rico Seismicity: U.S. Geological Survey Open-File Report 80-192.

Benford,B., DeMets, C. and Calais, E., 2012, GPS estimates of microplate motions, northern Caribbean: evidence for a Hispaniola microplate and implications for earthquake hazard: Geophysical Journal International, v. 191, no. 2, p. 481–490, doi: 10.1111/j.1365-246X.2012.05662.x

Blakely, R.J., and Simpson, R.W., 1986, Approximating edges of source bodies from magnetic or gravity anomalies: Geophysics, v. 51, p. 1494-1498.

Chaytor, J.D., ten Brink, U.S., 2010, Extension in Mona Passage, Northeast Caribbean: Tectonophysics, v. 493, no. 1-2, p. 74-92, doi:10.1016/j.tecto.2010.07.002.

Clinton, J.F., Cua,G., Huérfano,V., von Hillebrandt-Andrade, C.G., and Cruzado, J. M., 2006, The current state of seismic monitoring in Puerto Rico: Seismological Research Letters, v. 77, no. 5, p. 532-543, doi: 10.1785/gssrl.77.5.532.

Cooper, G.R.J., Cowan, D.R., 2006, Enhancing potential field data using filters based on the local phase: Computers & Geosciences, v. 32, no. 10, p. 1585-1591, doi: 10.1016/j.cageo.2006.02.016.

Dolan, J.F., Mullins, H.T., Wald, D.J., 1998, Active tectonics of the north-central Caribbean: Oblique collision, strain partitioning, and opposing subducted slabs: Geological Society of America Special Paper, v. 326, p. 1-61, doi: 10.1130/0-8137-2326-4.1.

Ficher, K.M., and McCann W.R., 1984, Velocity modeling and earthquake relocation on the Northeast Caribbean: Bulletin of the Seismological Society of America, v. 74, p. 1249-1263.

Gill I.P., Hubbard, D.K., McLaughlin, P., and Moore, C.H., 1989. Sedimentological and tectonic evolution of Tertiary St. Croix: Terrestrial and marine geology of St. Croix, US Virgin Islands, West Indies Laboratory, Spec. Pub. 8., p. 49–72.

Granja Bruña, J.L., ten Brink, U.S., Carbó-Gorosabel A., Muñoz-Martín, A., and Gómez Ballesteros, M., 2009, Morphotectonics of the central Muertos thrust belt and Muertos Trough: Marine Geology, v. 263, p. 7-33, doi: 10.1016/j.margeo.2009.03.010.

Grindlay, N.R., Hearne, M., and Mann, P., 2005a, High Risk of Tsunami in the Northern Caribbean: Research Focuses on Active Plate Boundary Faults and Potential Submarine Landslides: Eos Transactions of the American Geophysical Union, v. 86, p. 121.

Grindlay, N., Mann, P., Dolan, J., and van Gestel J.P., 2005b, Neotectonics and subsidence of the northern Puerto Rico-Virgin Islands margin in response to the oblique subduction of high-standing ridges, in Mann, P., editor, Active Tectonics and Seismic Hazards of Puerto Rico, the Virgin Islands, and Offshore Areas: Geological Society of America Special Paper 385, p. 31-60.

Gvirtzman, Z., *and* Stern, R. J., 2004, Bathymetry of Mariana trench-arc system and formation of the Challenger Deep as a consequence of weak plate coupling: Tectonics, *v.* 263, no. 2, p. 7-33, doi: 10.1029/2003TC001581.

Jansma, L.F., 1981, Mesozoic carbonate platforms and banks of the eastern North American margin: Marine Geology, v. 44, p. 97-117.

Jansma, P.E., and Mattioli, G.S., 2005, GPS results from Puerto Rico and the Virgin Islands: Constraints on tectonic setting and rates of active faulting. Active Tectonics and Seismic Hazards of Puerto Rico, the Virgin Islands, and Offshore Areas: Geological Society of America Special Paper, no. 385, p. 13-30, doi:10.1130/0-8137-2385-X.13.

Jolly, W.T., Lidiak, E.G., and Dickin, A.P., 2007, Bimodal volcanism in northeast Puerto Rico and the Virgin Islands (Greater Antilles Island Arc): Genetic links with Cretaceous subduction of the mid-Atlantic ridge Caribbean spur: Lithos, v.103, p. 393-414, DOI:10.1016/j.lithos.2007.10.008.

Jolly, W.T., Lidiak, E.G., and Dickin, A.P., 2008, The case for persistent southwest-dipping Cretaceous convergence in the northeast Antilles: Geochemistry, melting models, and tectonic implications: Geological Society of America Bulletin, v. 120, p. 1036-1052, doi:10.1130/B26207.1.

Lin, G.Q., and Huerfano V.A., 2011, Improving Three-dimensional Seismic Velocity Models and Earthquake Locations for Puerto Rico and the U.S. Virgin Islands: Collaborative Research between University of Miami and University of Puerto Rico in Mayaguez: US Geological Survey External Research No. G10AP00020 and G10AP00021.

Macari, E.J., 1994, A Field Study in Support of the Assessment for Liquefaction and Soil Amplification in Western Puerto Rico: Puerto Rico Earthquake Safety Commission, 35p.

Mann, P., Calais, E., Ruegg, J.C., DeMets, C., Jansma, P.E., and Mattioli, G.S., 2002, Oblique collision in the northeastern Caribbean from GPS measurements and geological observations: Tectonics, v. 21, no. 6, p. 7-1-7-26, *doi*:10.1029/2001TC001304.

Mann, P., Prentice, C.S., Hippolyte, J.C., Grindlay, N.R., Abrams, L.J., Dávila, D.L., 2005a, Reconnaissance study of Late Quaternary faulting along Cerro Goden fault zone, western Puerto Rico: GSA Special Papers, v. 385, p. 115-13, doi: 10.1130/0-8137-2385-X.115.

Mann, P., Hippolyte, J.C., Grindlay, N.R., and Abrams, L.J., 2005b, Neotectonics of southern Puerto Rico and its offshore margin: Geological Society of America Special Paper, v. 385, p. 173-214, doi: 10.1130/0-8137-2385-X.173.

Meighan, H.E., and Pulliam, J., 2013, Seismic anisotropy beneath the northeastern Caribbean: implications for the subducting North American lithosphere: Bulletin de la Societe Geologique de France, v. 184, no. 1-2, p. 67-76, *doi*: 10.2113/gssgfbull.184.1-2.67.

McCann, W.R., 2010, Estimating the lower limit of the seismogenic zone and rates of aseismic slip on the Puerto Rico Trench Megathrust using focal mechanisms and repeating earthquakes:, US Geological Survey External Research No. G09AP00070.

McCann, W.R., 2007, Improving the Seismic Hazard Model for Puerto Rico: A Reliable Microearthquake Catalog Through Seismic Velocity Modeling and Microearthquake Joint Location: US Geological Survey External Research No. 04HQGR0015.

Mendoza C., and McCann, W.R., 2005, Improving the Seismic Hazard Model for Puerto Rico through Seismic Tomography and a Reliable Microearthquake Catalog With Recalculated Magnitudes and Calibrated Hypocentral Error Estimates: US Geological Survey External Research No. 05HQGR001220.

Miller, H.G., and Singh, V., 1994, Potential field tilt – a new concept for location of potential field sources: Journal of Applied Geophysics, v. 32, p. 213-217.

Moya, J.C., and McCann, W.R., 1992, Earthquake Vulnerability Study of the Mayagüez Area, Western Puerto Rico, Comision de Seguridad Contra Terremotos, Department of Natural Resources., Puerto Rico, 43p.

Nasuti, A., Pascal, C., Ebbing, J., 2012, Onshore-offshore potential field analysis of the Møre-Trøngelag Fault Complex and adjacent structures of Mid Norway: Tectonophysics, v. 518-521, p. 17-28, doi:10.1016/j.tecto.2011.11.003.

Ottemöller, L., Voss, P., and Havskov, j., 2013, SEISAN earthquake analysis software for Windows, Solaris, Linux and MacOsX: Department Earth Science University of Bergen,Norway, 416 p.

Rogers, R.D. and Mann, P., 2007, Transtensional deformation of the western Caribbean-North America plate boundary zone. GSA Special Paper, no. 428, p. 37-64, doi: 10.1130/2007.2428(03).

Rodríguez-Martínez, J., 2007, Stratigraphy, structure, and geologic and coastal hazards in the Peñuelas to Salinas area, southern Puerto Rico: A compendium of published literature: U.S. Geological Survey Open-File Report 2007-1259, 27 p.

Smith, A.L., Schellekens, J.H., and Díaz, A.L.M., 1998, Batholiths as markers of tectonic change in the northeastern Caribbean: Geological Society of America Special Paper, v. 322, p. 99-122.

Sokoutis D. and Ernst W., 2011, Decoupling during continental collision and intra-plate deformation: Earth and Planetary Science Letters, v. 305, p. 435-444, doi: 10.1016/j.epsl.2011.03.028.

Speed, R.C., and Larue, D.K., 1991, Extension and transtension in the plate boundary zone of the northeastern Caribbean: Geophysical Research Letters, v. 18, p. 573-576.

ten Brink, U.S., and Lin J., 2004, Stress interaction between subduction earthquakes and forearc strike-slip faults: Modeling and application to the northern Caribbean plate boundary: Journal of Geophysical Research, v. 109, no. B12, p. B12310, doi: 10.1029/2004JB003031.

ten Brink, U. S., 2005, Vertical motions of the Puerto Rico Trench and Puerto Rico and their cause: Journal of Geophysical Research, v. 110, no. B6, p. B06404, doi: 10.1029/2004JB003459.

ten Brink, U.S., Stephen M. and Granja Bruña J.L., 2009, Bivergent thrust wedges surrounding oceanic island arcs: Insight from observations and sandbox models of the northeastern Caribbean plate: GSA Bulletin, v. 121, no. 11-12, p. 1522–1536, doi: 10.1130/B26512.1.

ten Brink, U.S. and López-Venegas Alberto M., 2012, Plate interaction in the NE Caribbean subduction zone from continuous GPS observations: Geophysical Research Letters, v. 39, p. L10304, doi:10.1029/2012GL051485.

van Gestel, J.P., Mann, P., Dolan, J.F., and Grindlay, N.R., 1998, Structure and tectonics of the upper Cenozoic Puerto Rico Virgin Islands carbonate platform as determined from seismic reflection studies: Journal of Geophysical Research, v. 103, p. 30505-30530.

CHAPTER 2: Integrated analysis of the uplift of Longmen Shan area in eastern Tibetan Plateau

[This chapter has been submitted to "*Earth and Planetary Science Letters*". Dr. G. Randy Keller, Rui Gao, Dr. Xiaoyu Guo and Dr. Xiaosan Zhu are coauthors for this paper]

Chapter 2: Integrated analysis of the uplift of Longmen Shan area in eastern Tibetan Plateau

ABSTRACT

The mechanism for uplift of the Tibetan Plateau is still a matter of debate. There are two main models: 1) extrusion, and 2) lower crustal flow. These two models have been tested by surface observations, but questions about the uplift remain. In addition, the devastating 2008 M_s 7.9 Wenchuan earthquake along the Longmen Shan Fault Zone (LMSFZ) reminds us that the tectonic activity within the eastern Tibetan Plateau is complex and hazardous. It is accompanied by the dramatic uplift of the LMSFZ, but no significant convergence (<4 mm/yr) against the Sichuan basin is observed. In order to investigate the mechanism for uplift of LMS area in the eastern Tibetan Plateau, we explored the lithospheric structure across the Songpan-Ganzi terrane, LMS and western Sichuan basin by undertaking an integrated analysis of deep seismic profiling, gravity, magnetic, and geologic data. Based on our new results and previous research, the current crust is not thick enough to support current elevation, so a 2D numerical simulation was conducted using a crustal structure model based on recent seismic refraction and reflection profiles results to discover a reasonable mechanism. The seismic and gravity results show that the crust is composed of 3 distinct layers (upper crust, middle crust and lower crust). Among them, the numerical simulation results show the middle crust beneath the Songpan-Ganzi terrane need be most ductile, which is the key factor responsible for the crustal-scale faulting, earthquake behavior and periods of uplifting. In addition, the modeling results show the flexural stress by the

strong Sichuan block is the cause of the uplift and subsidence of the Moho.

INTRODUCTION

The Longmen Shan (LMS) mountain range, the site of the devastating May 12, 2008 Wenchuan (M_w = 7.9) earthquake, defines the eastern margin of the Tibetan Plateau and exhibits greater topographic relief than anywhere else on the eastern portion of the plateau (Fig. 2.1a). Before the Wenchuan earthquake, geodetic and geologic surveys measured extremely fast uplift of northeastern Tibet, which was preceded by the M_s 7.8, 1879 Minjiang and M_s 7.2, 1976 Huya earthquakes (Burchfiel et al., 2008; Liu et al., 1996). There has been considerable debate about the process by which the topography of the mountain belt and the Moho geometry are produced and maintained. Two end member models have been proposed: (1) brittle crustal thickening (extrusion), in which thrust faults with large amounts of slip that are rooted in the lithosphere caused uplift (Tapponnier et al. 1982), and (2) crustal flow, in which low-viscosity material in the lower crust extrudes outward from the Tibetan plateau and inflates the crust north and east of the Tibet (Royden et al., 1997). The fundamental element of the extrusion model is crustal shortening. The LMS thrust belt is the only evidence for significant shortening across eastern Tibet. However, shortening only occurs in an upper crustal scale and slowly (Hubbard and Shaw, 2009). Regarding the crustal flow model, accumulation of a large amount of material in the lower crust is needed to maintain the uplift for such a long time. However, there is no strong evidence that indicates where the original source of the lower crustal material is. Therefore, a new explanation is required for a thorough understanding of the uplift mechanism. In this project, an integrated analysis of seismic profiling, gravity, magnetic, and geologic data is

presented. Based on a crustal model based the integrated results, 2D numerical geodynamic simulations were performed to fully understand the regional tectonic activity and crustal structure that are associated with the kinematic evolution of the LMSFZ.

GEOLOGICAL SETTING

The strong correlation between the topographic relief and earthquakes (Fig. 2.1c) in the eastern Tibetan Plateau has attracted much attention (e.g., Hubbard and Shaw, 2009). The LMS belt is the transition zone separating the Sichuan basin from the eastern Tibetan Plateau not only topographically but also structurally (Godard et al., 2009). The LMSFZ is characterized by thin-skinned fold and thrust deformation (Chen and Wilson, 1996) and consists of three major faults; the Wenchuan fault to the west, the Beichuan fault in the middle, and the Pengguan fault to the east. The basement cored uplifts (Pengguan and Baoxing Massifs), that are exhumed along the LMS belt by the Beichuan thrust fault, are composed of Proterozoic granitoids and metamorphic rocks of the Yangtze craton (Cook et al., 2013). The basement overthrusts the Mesozoic sediments to the east and is bounded to the west by the Wenchuan fault (Robert et al., 2010). The western Sichuan basin to the east of the LMSFZ contains thick and relatively undeformed Mesozoic-Cenozoic terrestrial sedimentary strata (Kirby et al., 2002). The Songpan-Ganzi fold belt to the west of the LMSFZ is dominantly a deformed Triassic flysch sequence that overlays the Paleozoic sediments at least in the easternmost Tibetan Plateau (Yin and Harrison, 2000). The Paleozoic sediments were deposited on the basement when it was in a passive margin setting (Harrowfield and Wilson, 2005).

Reactivation of the LMS belt during Cenozoic is an important part of the big picture regarding the uplift of the Tibetan Plateau. According to Global Position System (GPS) measurements, there is no significant active convergence of the LMS belt relative to the Sichuan basin (Zhang, 2013). However, the 2008 Wenchuan earthquake indicates that significant stress accumulation occurs along the LMSFZ. Related to the minor convergence, the exhumation pattern has been debated at different scales. Evolution of elevation in this area has not yet been fully understood, although study of the Asian monsoonal climate (An et al., 2001) and different dating methods were employed to study it (Clark et al., 2005; Godard et al., 2009; Kirby et al., 2002). Fission track dating shows the Wenchuan and Beichuan faults could have been reactivated during the Cenozoic (Xu et al., 2008a). In addition, the Beichuan fault, which was activated during the 2008 Wenchuan earthquake, is the major active structure of the LMS since the late Miocene. It possesses an average uplift rate between 0.7 and 1.2 mm/a with an estimated initiation age between 5-12 Ma (Burchfiel et al., 2008). At a regional scale, two major rapid exhumation patterns have been proposed (Wang et al., 2012a), including a slow exhumation during the early Cenozoic and two episodes of rapid exhumation (30-25 and 8-15 million years ago). The exhumation is currently active at a rate less than 0.5 mm/a (Wang et al., 2012a). In the last century, most of the regional large earthquakes (magnitude >6, from USGS database) occurred in the relatively high topography of the LMS range front (Figs. 2.1b and 2.1d). The LMSFZ contains the highest density of the large earthquakes in this area, where most of the earthquakes had focal depths between 10- 30km (Fig. 2.1d). How much uplift occurred in the last 15 million years is unknown. We have carried out an integrated analysis and numerical

simulations to compare with the geological features in this area with the goal of informing an evolutionary model for the region.

SEISMIC REFLECTION AND REFRACTION DATA ACQUISITION

The SinoProbe-02 seismic refraction and reflection experiments are recent efforts to investigate the seismic structure of the lithosphere beneath the LMSFZ and adjacent areas (Dong et al., 2011), as well as, many other regions of China. The main target of this effort is to determine the regional crustal characteristics of this region and to establish its structural geometry with depth, and for the first time to image the crust of the eastern edge of Tibet, especially the extremely thick sediments. Additionally, this project is designed to detect the structural features of the transition zone from the eastern Tibetan Plateau (SGT) to the Yangtze Proterozoic block to detect the deep contact geometries.

In the autumn of 2011, the SinoProbe-02 working group, a consortium from the Institute of Geology at Chinese Academy of Geological Sciences and the University of Oklahoma, USA collected both deep seismic reflection and refraction profiles that extended from the SGT to the Sichuan basin (Fig. 2.1b). The 310 km long deep seismic reflection profile roughly extends NW-SE from the SGT to the Sichuan basin (Fig. 2.1b). In order to obtain high-resolution seismic images of the crust, three types of explosive sources (24 kg, 96 kg and 500 kg) were employed. The 24-kg, 96-kg and 500-kg shots were placed at intervals of 250 m, 1000 m and 50 km respectively. Each shot of the reflection line was recorded by 600 geophones on both sides with 50 m spacing. Processing steps for the seismic reflection profile data are summarized in Guo et al.

(2013), and these basic data processing procedures have been widely used in all of the SinoProbe-02 reflection profiles.

A 400km-long refraction and wide-angle reflection profile was also collected during this seismic experiment. A total of 355 TEXAN refraction instruments were deployed at a station spacing of 1.5 km. The elevation in the area varies from less than 500m in the basin area to more than 3,000m in the LMSFZ over a horizontal distance less than 50km, which made the deployment of Texan instruments and data acquisition challenging. Acquisition of seismic refraction data originally started with an attempt to achieve a straight-line spread, but owing to the severe topography, it was subsequently changed to follow a highway. The 12 sources for acquisition of the refraction data ranged in size from 2000 to 500 kg. Only 10 of the 12 shots were used in this study due to the low signal-to-noise ratio of the other two shots. Thus, coincident high-density and near-vertical reflection and crustal-scale refraction data provided the main data for our integrated study of velocity distribution and seismic structure of the lithosphere.

REFRACTION AND REFLECTION TOMOGRAPHY METHOD

Travel time picks

Identification of seismic phases was done manually by computer employing filtering and varying reduction velocities (Zelt and Forsyth, 1994). Four phases (P1, P2, PmP and Pn) were picked (Fig. 2.3), and all of them are P waves. P1 and P2 are intra-crustal reflections, while PmP and Pn are Moho and reflections upper mantle refracted phases, respectively. The upper crustal refracted phase (Pg) was not used in this project, because the stacking velocity information (Fig. 2.2a) from the reflection data at 50m

CDP intervals has higher resolution than that of the refraction data with 1500m intervals. The uncertainties of the picks were calculated by the ZP code (Zelt and Forsyth, 1994), the uncertainty for the PmP and the Pn arrival picks is less than 0.125s and is 0.05s for the intra-crustal reflection picks. The data were band-pass filtered between 3 and 10 Hz based on spectral analysis. Due to the complex geology and topography, the signal-to-noise ratio is low (Fig. 2.3). Thus, an initial velocity model (Fig. 2.2c) for both forward calculation and simultaneous inversion was constructed based on our stacking velocity data (Fig. 2.2a) and previous seismic surveys in the region (Wang et al., 2007; Wang et al., 2012b; Zhang et al., 2011; Zhang et al., 2013). We used forward modeling results (Figs. 2.3b and 2.3d) based on this model as the reference for picking phases. A particularly clear observation is that PmP picks (Fig. 2.3e) show that the Moho depth decreases from the SGT to the Sichuan basin, because Pn is observed as a first arrival after 200km from the source in Sichuan basin (Fig. 2.3e) and after about 250km from the sources in the SGT (Fig. 2.3a).

Resolution Test and ray coverage

Calculations of travel times and ray paths were made the using the Fast Marching Tomography Package (FMTOMO) (Rawlinson and Urvoy, 2006). FMTOMO is a Fortran 90 software package for 3D travel-time tomography. It is one of the research products of Prof. Nick Rawlinson now at University of Aberdeen. The FMTOMO code is designed to simultaneously invert multiple travel time datasets for 3D velocity variations and interface structure. With implementation of the FMTOMO code, travel-time grids are computed. In order to estimate the resolution of the tomography model derived, we performed checkerboard testing. The synthetic dataset was generated using

a four-layer model with three interfaces. To highlight the result of resolution test, the velocity model and interfaces were simplified from the initial model (Fig. 2.2c). In this model, the velocity layers are homogeneous and flat, the velocity of sediments is 5km/s, and the depth of Moho is 45km. A checkerboard pattern with amplitude 0.5 km/s was added over the 1D model with a velocity grid (0.44°x0.44°x10km) (Fig. 2.4a). Thereafter, FMTOMO was employed to calculate synthetic travel times through this model, which was first modified by adding uncertainties of +/- 0.1s. The inversion of the synthetic arrival time residuals met the convergence minimum value after 6 iterations. The vertical slice shown in Figure 2.4b shows that the data cover most of the research area with good resolution. The ray paths (Fig. 2.4c) were computed using the final velocity model. The upper two layers have dense ray coverage, and the LMS area has better coverage than the SGT. The upper mantle is sampled adequately. The traveltime residuals between the observed and computed travel times are shown in Figure 2.5, and most residuals for P2, PmP and Pn are less than +/-0.5s. The P1 phase residuals are somewhat larger.

Parameterization grid, starting model and calculation

The refraction line is crooked because of the steep relief and the Minjiang River (Minjiang fault zone), and due to concern for safety, we deployed the shots away from areas with high population density. Thus, 3D modeling was employed for the velocity calculations. The velocity grid cell size of the starting 3D model was 0.165° x 0.165° x 2.25km (longitude x latitude x depth) (see location in Fig. 2.1b). The top interface is 5.5km above sea level and the bottom is 85km below sea level. The velocity of the first layer is based on the deep reflection stacking data (Fig. 2.2). The initial Moho depth

was set based on the results of Wang et al. (2010a). The other velocity layers were initially homogeneous with the interfaces being horizontal (Fig. 2.3c). The tomography inversion was calculated from the upper crust to the upper mantle layer by layer. Only one layer is involved in the calculation of each step of the inversion, and all picks were used in the calculations. The top and bottom interfaces were fixed and did not take part in the inversion.

Final velocity and interfaces images

The final velocity model (Fig. 2.6a) has four layers, including the upper crust (mostly sediments), middle crust, lower crust, and upper mantle. The top layer is the sedimentary cover, which is divided into three segments by two major fault zones. The Ruo'ergai basin is located to the west of the Longriba fault zone, which is covered by thick Triassic flysch (Yin and Harrison, 2000). Additionally, the Triassic flysch covers most of the area between the Longriba fault zone and LMSFZ, and was deposited atop Paleozoic sediments at least in easternmost Tibet (Xiao et al., 2007). Cretaceous and Quaternary sediments were deposited in the Sichuan basin east of the LMSFZ (Liu et al., 2012; Richardson et al., 2008). In the upper crust of the area, the lowest velocities (~3.6 km/s) appear in the Sichuan basin. The highest velocities of the upper crust appear in the area between the Longriba fault zone and Minjiang fault, which is associated with adakitic type granitoids. These granitoids formed from the partial melting of Proterozoic basement (Zhang et al., 2006; Guo et al. 2013). The middle crust layer is relatively homogenous with a few lower velocity zones beneath the Ruo'ergai basin and LMSFZ. The thickest part of the middle crust is east of the Minjiang Fault, which is under compression from the west. The thickness of the lower crust decreases from west to

east. The lower crustal high velocity zone beneath the Ruo'ergai basin can be seen in the deep reflection data (Guo et al., 2013).

In order to show the 3D variations in the model interfaces, structural relief was obtained from the difference between the modeled depth and the average depth of each interface in 3-D (Fig. 2.6b). Thus, the interfaces could be displayed together in 3-D at the same scale for comparison. Figure 2.6b shows that the base of the sediments rises to the east of the LMS area, probably because of thrusting (e.g., Hubbard and Shaw, 2009). The middle crust appears to have absorbed the compression by shortening both to the NW and SE of the LMS (Fig. 2.6b), which uplifted the overlying sediments. In the lower crust, the thickness increases from the Sichuan basin to the Ruo'ergai basin (Fig. 2.6b) with the LMSFZ as a transition zone. Thus, the Moho depth increases as the elevation increases.

INTERPRETATION OF GRAVITY AND MAGNETIC DATA

The magnetic anomaly data was extracted from the World Digital Magnetic Anomaly Map (WDMAM) project (Maus et al., 2007). The WDMAM consists of all available near-surface and satellite magnetic anomaly data and is specified as a global 3-arc-minute resolution grid of the magnetic intensity at an altitude of 5 km above sea level. The magnetic anomaly after reduction to the magnetic pole is shown in Figure 2.7a. A series of relatively short-wavelength magnetic anomalies appear in the southwestern Songpan-Ganzi terrane and suggest upper-crustal northeast-trending fold belts, which probably resulted from the compression against the rigid Sichuan basin. These anomalies die out towards the northeast, which is consistent with a northeastward decreasing compression. The high positive anomalies that appear in these fold belts are

consistent with anomalies that are shown in the gravity data (Fig. 2.7b), which are associated with the Mesozoic plutons (Zhang et al., 2014). The broad high anomaly zone in the southeast is associated with the crystalline basement of the eastern Sichuan Basin. Linear high magnetic anomalies are coincident with the LMSFZ area that has high earthquake risk (Figs. 2.1b) due to existence of the active Beichuan fault between the Pengguan Massif, which is composed of both Precambrian granite and metamorphic rocks and the Sichuan crystalline basement (Cook et al., 2013; Guo et al., 2013b). The high magnetic anomalies in the West Qinling area are related to the granitoid intrusions that were associated with the amalgamation between the Qinling orogen and Yangtze block during Triassic time (Sun et al., 2002; Guo et al., 2012). In addition, no large-scale fault zone is evident within the Songpan-Ganzi terrane in the magnetic map (Fig. 2.7a), which indicates that the upper crust beneath the Songpan-Ganzi terrane has not been significantly involved in the Cenozoic deformation. Thus, uplift of the SGT was largely as a coherent block.

Gravity anomaly data used in this study were extracted from the International Center for Global Earth Models (ICGEM). These data were collected through a long-term archiving of existing global gravity field models, which allows calculation of gravity functions from the spherical harmonic models on freely selectable grids. Simple Bouguer gravity anomaly values that were calculated with a Bouguer reduction density value of 2.67g/cm^3 were downloaded and mapped with the Geosoft/Oasis Montaj processing and analysis package. However, according to the tomographic results of this study and the application of Gardner's rule (Gardner et al., 1974) for estimating density from seismic velocity, the density of the sediments is between 2.3g/cm^3 and 2.4g/cm^3.

As a result, the Bouguer correction was redone using a density of 2.35g/cm^3 for this study. The elevation values employed in this calculation were from the 3-arc-second resolution Shuttle Radar Topography Mission (SRTM). This digital topography has higher spatial resolution than that of the gravity data, so the new simple Bouguer gravity is somewhat noisy (Fig. 2.7b). After this reduction, the new simple Bouguer gravity anomalies in the SGT are ~30 mGal less negative than the original data.

The simple Bouguer gravity anomaly values clearly indicate a NW to SE decrease in Moho depth across the SGT and a strong gradient across the LMSFZ (Fig. 2.7b). The gradient is variable along the LMSFZ, and it is generally stronger to the southwest than to the northeast. These variations of the gravity gradient along the LMSFZ indicate that the southeastward-directed stress and shortening in the southwest is larger than in the northeast, which is consistent with the deeper Moho to the southwest (Wang et al., 2003). Local high anomaly values in the Songpan-Ganzi Terrane are associated with Mesozoic plutonic rocks (Kirby et al., 2002; Chen et al., 2009; Roger et al., 2004).

The 2D gravity modeling was done with the GM-SYS modeling package. Each interface in the gravity model below the upper crust was derived from the tomographic results. An average P-wave velocity for each of these layers was calculated and densities for the layers were calculated from the P-wave velocity by using the Nafe-Drake's relationship for crustal layers (Brocher, 2005). The gravity forward model (Figs. 2.8a and 2.8b) shows that the trend of the simple Bouguer anomaly is consistent with that of the Moho depth, indicating it is strongly controlled by the variations of crustal thickness. After minor iterations of the upper crust in the gravity model guided by the seismic results, it is clear that the thickness of the Triassic Songpan-Ganzi flysch

increases from east to west, where the deepest part is about 12km. Aided by thrusting, the base of the sediments deepens beneath the LMSFZ and shallows towards both the easternmost Sichuan basin and Songpan Ganzi Terrane, respectively (Fig. 2.8b). The upper crustal higher density lens that appears under the sediments in the Minjiang fault and Longriba fault zone area is probably associated with partial melting of the Proterozoic basement during the Mesozoic (Zhang et al., 2006) and is a high velocity of the upper crust in the tomographic model (Fig. 2.9). Both the middle and lower crust have variable thicknesses probably due to the eastward compression against the rigid Sichuan basin of the area. The thickest middle crust appears immediately west of the LMSFZ, while the thickest lower crust appears beneath the Songpan-Ganzi terrane. Therefore, we suggest that the thickening of the middle crust west of the LMSFZ is caused by the eastward compression, which is blocked by the stable lithosphere of the Sichuan basin.

Based on our tomography and gravity results, the crustal thickness is around 50km in Longmen Shan area and the average elevation is about 3000 m. However, according the previous research by Wang et al. (2010b), the typical crustal thickness of 40 km for continental crust must include an additional thickness of 28 km to support an average elevation of 4000 m. Thus, in our case of the Longmen Shan area whose average elevation is ~3000m, a crustal thickness of ~60km is needed to support the current elevation. In order to test this idea, we calculated the elevation with the layer thicknesses and density the integrated gravity model (Fig. 2.8b) with the assumption of isostatic balance. The initial crustal thickness is unknown, so based on average crustal thickness globally (e.g., Zandt and Ammon, 1995), we used a range of original crustal

thickness. Based on our crustal structure results, which define a 3-layer crust, the equation to estimate elevation can be written as:

$$H = [(h_c-h_o)\rho_m+ h_o\rho_c- h_s\rho_s- h_{mc}\rho_{mc}- h_{lc}\rho_{lc}]/\rho_s \ , \quad (1)$$

where H is the elevation calculated at intervals of 1.5 km along the profile, h_c is the Moho depth based on the integrated gravity model, h_o is the initial crustal thickness (30 km, 35 km, and 40 km), h_s is thickness of the sediments, h_{mc} is the thickness of the middle crust, and h_{lc} is the thickness of the lower crust. The corresponding densities are ρ_m (density of mantle), ρ_c (average crustal density (Wang et al., 2010b), ρ_s (the density of the sediments), ρ_{mc} (the density of the middle crust), and ρ_{lc} (the density of the lower crust). In equation (1), the top of the original crust is at sea level and the crust is assumed to be 35 km thick.

Figure 2.8c shows the elevation with 35 km original crustal thickness is the most approximate result comparing with current average elevation in Sichuan basin. Our results show that the Moho depth is ~40 km in the Sichuan basin that is part of the Yangzi block. This value is consistent with our isostatic equation given that the average elevation in the basin is 700-800m. The region west of the LMS was a passive margin until the late Triassic (e.g., Guo et al., 2013), so 35 km is a reasonable value for the original crustal thickness. In this region, the calculated elevation is lower than the current elevation indicating that the current crustal thickness (<55km) is not enough to support current elevation only by buoyancy. Thus, flexural stress due to convergence with the strong Sichuan block is a possible reason to provide the extra support for the higher elevation.

NUMERICAL MODELING

Methods

The uplift is ongoing along Eastern margin of the Tibetan Plateau, and several geodynamic modeling efforts have been undertaken in this area to test different uplifting mechanisms (Sun et al., 2013; Clark and Royden, 2000; Chen et al., 2013). These models simulated the lithospheric scale deformation. However, we have relatively high resolution crustal scale reflection and refraction data in our study area so we constructed a 2D model to simulate the uplift on a crustal scale. In order to test two major uplifting models (Tapponnier et al. 1982; Royden et al., 1997), we decided to employ the open source *Gale* finite element-based code distributed by the Computational Infrastructure for Geodynamics (CIG) project. The models were run with the Gale 2.0.1 code (Moresi et al., 2003), which is appropriate for parallel layer and two- or three-dimensional simulations. *Gale* simulates problems with large deformation and irregular boundaries. It starts with a collection of particles to track material properties and can be used for modeling orogenesis, rifting, and subduction. The starting model (Fig. 2.9) was based on the structural model derived from tomography (Fig. 2.6a) and gravity results (Fig. 2.8b). Thus, three initial models were constructed with four layers, including the upper crust, middle crust, lower crust and lithospheric mantle. The LMSFZ is located within the Yangtze block, so it was sufficient for the area west of the LMSFZ to have the same generalized structure as the Sichuan Basin area (Guo et al., 2013a, 2013b).

Our simulation focused on the reactivation of the LMSFZ during late Cenozoic. According to previous research, the LMSFZ dips ~45^{o} towards the west (e.g., Shen et al., 2009) (Fig. 2.9). In our four layered models, we defined densities determined by the gravity modeling results and rheological properties. The crustal thickness was set at 45 km (Lease et al., 2011), and each crustal layer is 15km thick and 400km wide, while the lithospheric mantle is 40km thick. The mantle viscous deformation is accommodated by dislocation and diffusion creep (Evans and Kohlstedt, 1995), those are strain rate dependent rheology. In the Gale code, the viscosity has been written as

$$\eta_m = \acute{\varepsilon}^{(1/n-1)} \exp(T_0/nT)/2A^{(1/n)} \quad (2)$$

where η_m is the mantle viscosity, $\acute{\varepsilon}$ is the strain rate, T_0 is the initial temperature, T is the temperature, and A and n are constants. The temperature was calculated using the normal geothermal gradient (25^{o}c/km) (Wood and Hewett, 1982). The viscosity was set between 10^{16}Pa s to 10^{22}Pa s (Clark and Royden, 2000; Arrial and Billen, 2013). The Drucker-Prager yield criterion (Drucker and Prager, 1952) was used for determining whether the crustal material has failed or undergone plastic yielding, and it has the form:

$$\sqrt{J} = Ap + B, \quad (3)$$

$$A = 2\sin\phi/\sqrt{3}(3-\sin\phi) \quad (4)$$

$$B = 6C\cos\phi/\sqrt{3}(3-\sin\phi) \quad (5)$$

$$\eta_{c} = (Ap+B)/\sqrt{\dot{\varepsilon}} \quad , \quad (6)$$

where p is the pressure, J is the stress, C is the cohesion, ϕ is the angle of internal friction and η_c is crustal viscosity. If the η_c is less than minimum viscosity, then η_c is set to the minimum viscosity.

Previous research shows that the middle or lower crust has the capacity to flow during geologic time because of low viscosity (Block and Royden, 1990; Wdowinski and Axen, 1992). Our tomography results and other research (Liu et al, 2014; Wang et al., 2010b; Li et al., 2014a) suggest the middle crust with low velocity has the greatest likelihood of low viscosity. Based on the channel flow model proposed by Clark et al. (2000) and the previous research by Huang et al (2014), we employed different viscosity parameters for the middle crust in three models (Fig. 2.9).

In these models, the observed shortening rate is 3mm/yr (Zhang et al., 2004), and we set the west boundary to move with this constant velocity and the east boundary to be fixed. The top surface of the model is flat and the initial is elevation is 0. The bottom surface is static and is loaded by gravity caused by the overlying layers. The bottom stress boundary condition equals to the total mass weight of the material above the bottom of the initial model (Fig. 2.9); this means the pressure on the bottom of the model is always the same through the simulation. Thus, the elevation can only be supported by buoyancy and lateral compression. According the previous research by Wang et al (2012), eastern Tibet experienced a two-phase growth of high topography during 30-25 Ma and from 10-15 Ma until the present. Thus, we set the shorting to be a constant 18 Ma, which is the average of these values. The purpose of this numerical simulation is to answer these questions: (1) Can uplift be driven only by shortening at the current shortening rate? (2) Why did most large earthquakes (Figure 2.1) take place at a similar depth? (3) Does the low viscosity of the middle crust is the only factor responsible for this uplift?

Results

The three model simulations were captured at intervals of 5 to 18 Myr. The simulation results are the strain rates of three models in Figure 10a, and the results for pressures are shown in Figure 2.10b. The resulting elevations are shown in Figure 2.10c. In Figure 2.10a, the strain rate increases slowly in model I, and the area with the largest strain rate appears as a V shape beneath the LMSFZ. The area west of LMSFZ acts as a coherent block, without a major variation in strain rate between the main crustal layers. The strain rate increases more rapidly in model II than in model I, and strain accumulates in the middle crust. At 18 Ma, the largest strain rate occurs along the LMS fault surface. Compared to the other models, the strain increases mostly strongly beneath the LMSFZ. In model III, the high strain area extends deeper and also extends beneath the Sichuan Basin. In models II and III, strain is high in the middle crust east of the LMSFZ. However, model II has more strain accumulation in the west beneath the Songpan-Ganzi terrane than do the other two models.

In Figure 2.10b, all model results show a concentration of pressure along the Moho, resulting in offsets of the Moho and several thrust faults as observed in the seismic reflection presented by Guo et al. (2013). The most intense faulting appears beneath the LMSFZ in both Model II and Model III, which has been observed in previous studies (e.g. Zhang et al., 2009, Guo et al., 2013a). The Moho depth is approximately the same beneath the Sichuan Basin and Songpan-Ganzi Terrane in Model III, and Moho depth beneath the LMSFZ is much deeper than others. However in Models I and II, the Moho depth is shallower beneath the Sichuan Basin than in the Songpan-Ganzi Terrane. Models II and III show more crustal deformation. In the region of the Moho, the largest pressure changes occur along the LMSFZ in Model III.

In Figure 2.10c, all the results show that these three models with different viscosity can result in different elevations. However, all models contribute to the LMS uplift. Before 10 Ma, the three models have similar relief and elevations. The extremely high elevations to the west are caused by the model boundary effect. However after 10 Ma, Model III has a higher slip rate at the front of the LMS area than is present in Models I and II. Model II, on the other hand, creates a deeper basin and higher elevation to the west of the LMS area. Uplift basically ceased in Model I after 10 Ma, but in Models II and III, uplift continued after 10 Ma. Model II displays the most variation in uplift with the strongest uplift occurring between 15 and 18 Ma. Using balanced cross-sections derived from seismic reflection data, Li et al. (2014b) calculated a fault slip rate of 0.25 mm/yr. Based on a 31^{o} angle for the LMSFZ, we calculated a vertical uplift rate of 0.125 mm/yr. Model II predicts an average vertical uplift rate of 0.125 mm/yr, the uplift rate of model I is 0.105 mm/yr and the uplift rate of model III is 0.139 mm/yr. Thus, Model II best fits three different observations (Moho depth, earthquake focal depths, and uplift rate) derived from measured data.

DISCUSSION

Comparing with the geological observations, the numerical simulation results indicate the ductile middle crust beneath the Songpan-Ganzi Terrane is the most important factor responsible for earthquakes, faulting in this area and second phase of uplifting, and rigid Sichuan basin constrains the depth of Moho and support uplifting. Models II and III have high strain rate along the LMSFZ and relative high strain rate in middle crust, so these areas have the most potential for earthquakes. Models I and II produce Moho depths similar to our tomography result and faults cutting through Moho

that can be seen in deep reflection data (Guo et al. 2013). Models II and III produce the steep slope and high elevation along the LMSFZ. Based on these features, model II is most reasonable result. However, Model II also has its own defect, why the setup of initial viscosity condition within the middle crust of Songpan-Ganzi terrane is lower than the middle crust of Sichuan basin has. Thus, the final evolution model is a combination of Model I and Model II.

The LMS area is a weak zone that is easy to deform by shortening. The simulation started with same normal viscosity, the radiogenic heat production increases (Mareschal and Jaupart, 2013) with the crustal thickness of eastern Tibet increases with time, since the heat only can be transmitted by conduction, the interior region of the crust accumulates more heat (Robert et al., 2010). The lower crust usually has heat production that is less than the middle and upper crust (Mareschal and Jaupart, 2013), and the upper crust loses heat by the surface heat flux. Thus, the middle crust has a relatively high temperature and becomes more viscous. Then the viscosity of the middle crust west of LMSFZ changes to low viscosity, but the Sichuan basin is too rigid to be thicken, so the viscosity of the middle crust beneath Sichuan basin does not vary significantly.

Another high accumulation of strain rate appears along the western portion of the profile, which is coincident with the Longriba Fault zone (Fig. 2.9). The Longriba fault zone is located in the northeastern Songpan-Ganzi terrane, ~200 km northwest of the LMSFZ (Fig. 2.1) It was first discovered and discussed by Xu et al. (2008b), and it is associated with a sharp zone where GPS velocities decrease from west to east (Lv et al., 2003; Shen et al., 2005). The Longriba fault zone consists of two sub-faults, the

Longriqu fault to the west and the Mao'ergai fault to the east. These two sub-faults are ~30 km apart and show different senses of movement. The Longriqu fault features dextral thrusting, while the Mao'ergai fault features pure dextral shearing (Ren et al., 2013). A high velocity anomaly appears just east of the Longriba fault zone at ~10km depth in the P wave stacking velocities derived from the deep seismic reflection data (Fig. 2.2), as well as the combined P wave tomography result derived from refraction and wide-angle reflection data (Fig. 2.6a). This high velocity zone is consistent with the presence of Mesozoic adakitic granitoids, which are undeformed and intrude through the Triassic sediments. This type of granite produced highs on the magnetic anomaly map (Fig. 2.7a) and has been interpreted as being due to partial melting of the basement by compression (and possibly subduction) from the west (Zhang et al., 2006, 2014).

The recent deep reflection profile detected virtually no interfaces in middle crust (Guo et al., 2013a). However, based on P wave tomography results presented here (Fig. 2.6a), there are a several low velocity zones in the middle crust which are consistent with it being, a ductile feature as shown in the numerical modeling. Therefore, we propose that the middle crust is a distinct layer between the upper and lower crust. With the accumulation of extra heat by crustal thickening, the rheology of the middle crust at depths between ~10 and 25km became viscous.

CONCLUSIONS

The crustal structure across the study area has been resolved into three main layers; the upper, middle, and lower crust. The upper crust consists of Triassic flysch, Devonian to Cretaceous sediments, and the Mesozoic and Precambrian granites, as well

as, Eocene to Quaternary sedimentary deposits in the Sichuan Basin. The P-wave velocity model shows several low velocity zones in the middle crust. The average thickness of the middle crust is around 15 km, with the thickest part immediately west of the LMS belt. The lower crust is also thickened most beneath the LMSFZ. The P-wave tomography and gravity anomalies show that the Moho depth varies significantly from the Sichuan Basin to the Songpan-Ganzi terrane, especially beneath the LMSFZ.

Comparing the results of numerical simulation with the foci of earthquakes, surface topography, and Moho depth, we find normal continental crustal thickness (40-45km) is enough to produce the elevation of the eastern Tibetan Plateau with compression against the rigid Sichuan block and no extra material is needed for uplift. On the other hand, owing to the more ductile middle crust, elastic shortening energy is easier to accumulate. Once the accumulated elastic shortening energy reaches a critical level, it is released through weak zones, e.g. the LMSFZ and the Minjiang fault zone. This release produces large earthquakes, and more significantly, the uplift of eastern Tibet by thrusting. Meanwhile, due to the ductile middle crust beneath the Songpan-Ganzi terrane, the total rigid portion of the crust is thinning. Therefore, it becomes more difficult for the in-situ thinner upper and lower crust to resist the compression from the west. So the uplift in this area is due to these processes: 1) crustal thickening and shortening along the LMS area by compression from the west that is resisted by the relatively rigid Sichuan block, 2) extra heat accumulating by crustal thickening makes the middle crust more ductile, 3) the upper and lower crust continue shortening along the LMSFZ by thrusting, and 4) the middle crust is thickened and shortened by compression.

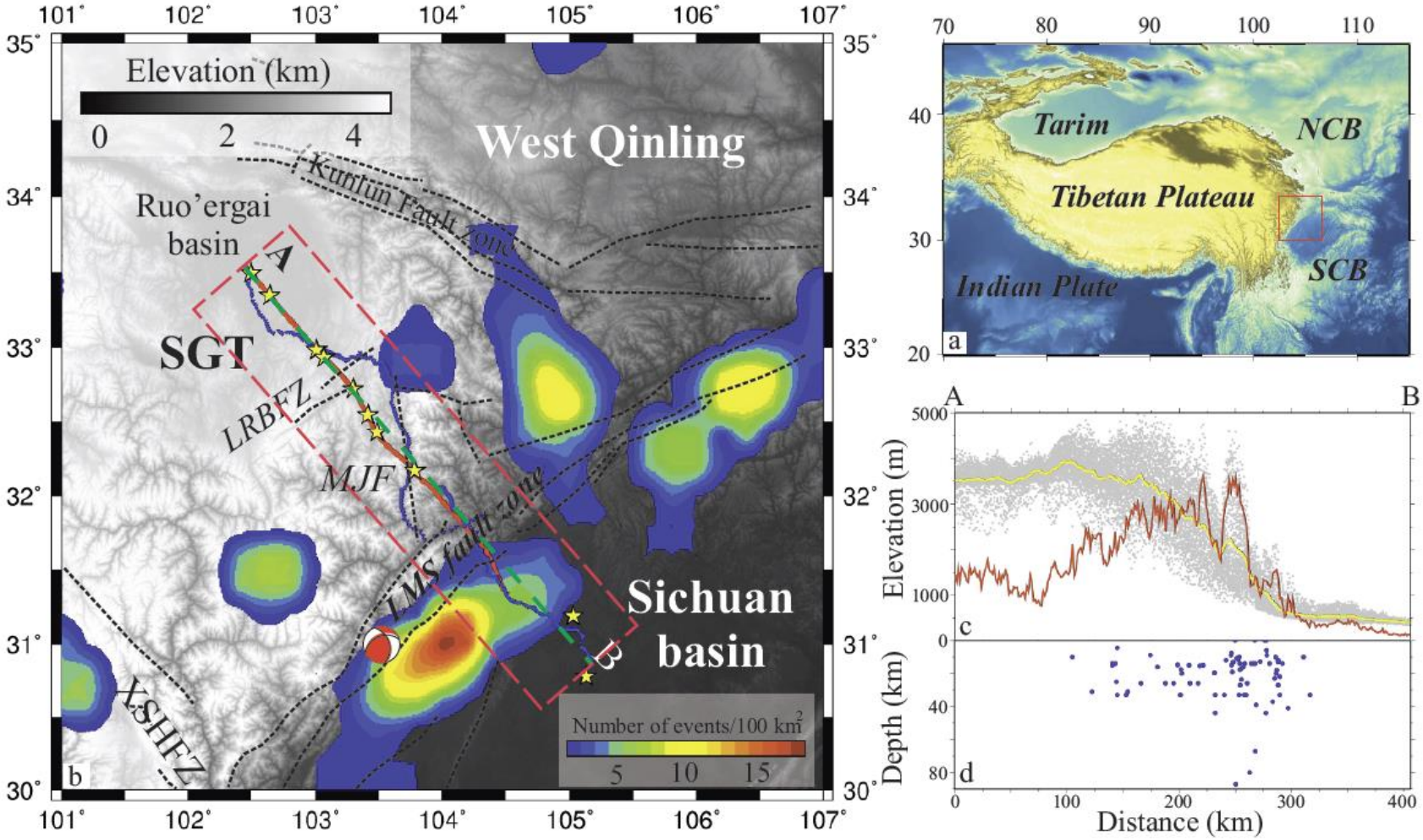
Elevation (km)
0
2
4
West Qinling
Kunlun Fault Zone
Ruo'ergai basin
A
SGT
LRBFZ
MJF
LMS fault zone
Sichuan basin
B
XSHFZ
Number of events/100 km²
5
10
15
b
101°
102°
103°
104°
105°
106°
107°
35°
34°
33°
32°
31°
30°
Tarim
NCB
Tibetan Plateau
SCB
Indian Plate
a
70
80
90
100
110
40
30
20
A
B
Elevation (m)
5000
3000
1000
0
c
Depth (km)
0
40
80
d
0
100
200
300
400
Distance (km)

Figure 2.1. (a) Regional topographic map of Tibetan Plateau, the red box shows the location of b. (b) Topographic map of the eastern Tibetan Plateau and Sichuan basin, which is overlaid with the earthquake distribution (magnitude>6) for the past 100 years. Red line is the location of deep reflection profile, blue triangles are the receivers of the refraction and wide-angle reflection profile, and yellow stars are the shot points for this profile. The red box is the location of elevation and earthquake data. The green dashed line is the location of all of the vertical profiles in this paper. (c) Gray dots are the projections of the elevations within the red box in b, yellow line is the average elevation of the gray dots, and the red line is the relief basing on the average elevation. (d) the projected depth of the earthquakes (magnitude>6) that occurred beneath the red box in b.

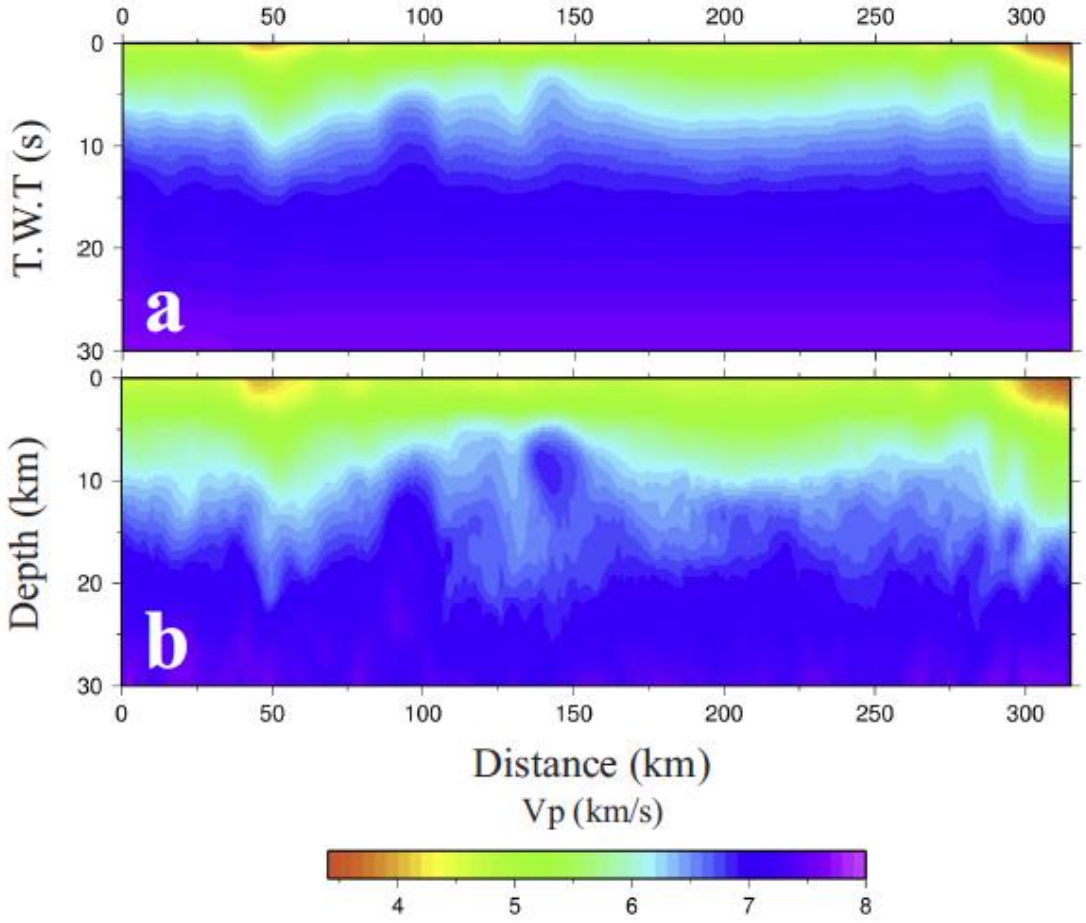

Figure 2.2. (a) Stacking velocity cross-section derived from the deep reflection data, (b) interval velocity was converted from stacking velocity employing the Dix formula (Dix C.H., 1955).

Layer	P wave velocity	Depth
Upper crust (Sediments)	Interval velocity of deep reflection data	10km
Middle crust	6.3km/s	25km
Lower Crust	6.8 km/s	Wang et al., 2010
Lithospheric mantle	8.0km/s	80km

Figure 2.2. (c) Starting model of P wave tomography.

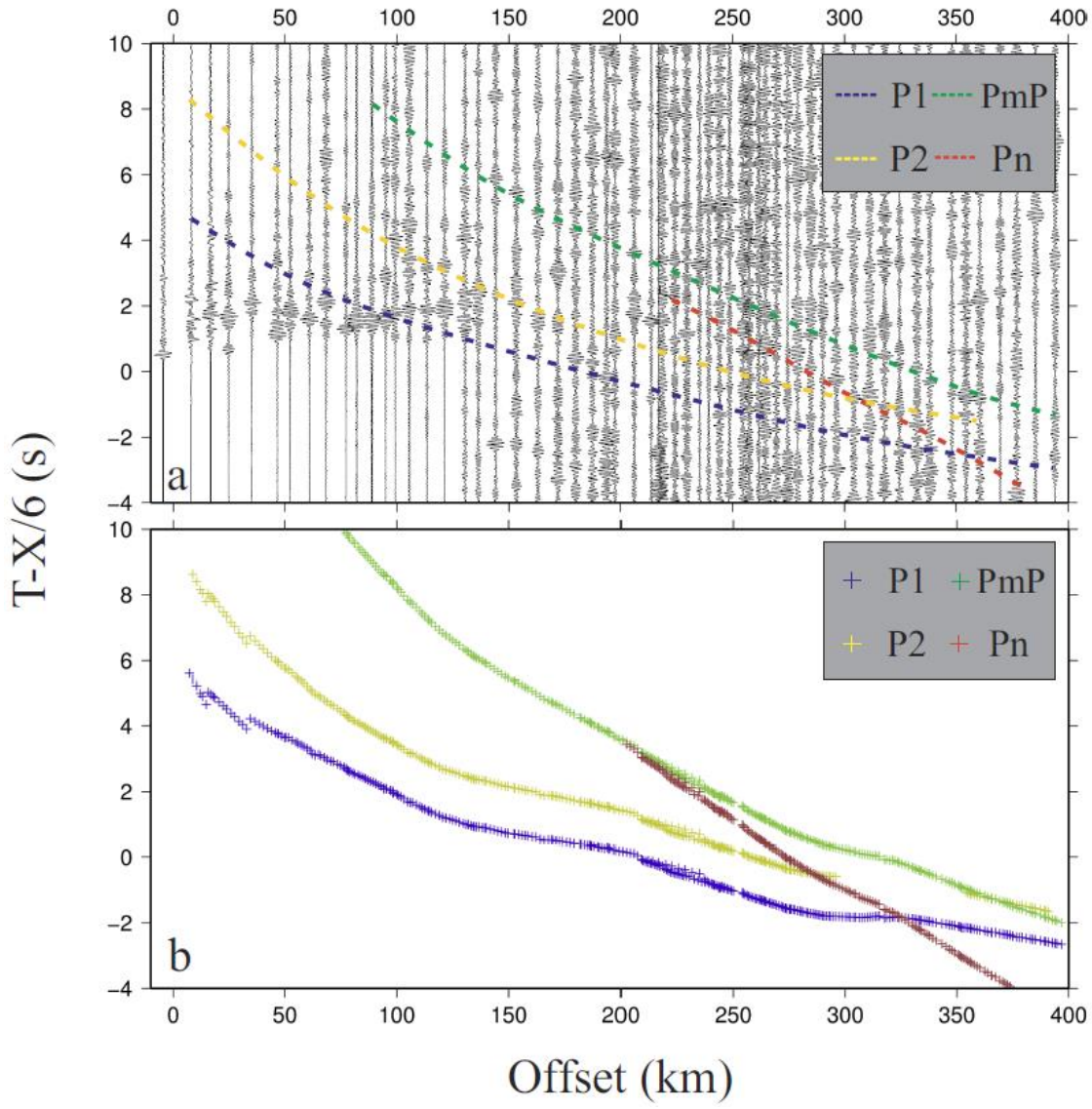

Figure 2.3. (a) Observed waveforms for shot 1 of the refraction and wide-angle reflection profile. (b) Plot of travel-time picks for shot 1. P1 and P2 are intracrustal reflections; PmP and Pn are Moho reflections and upper mantle refractions respectively. Blue crosses are P1, Yellow crosses are P2, Green crosses are PmP, and Red crosses are Pn.

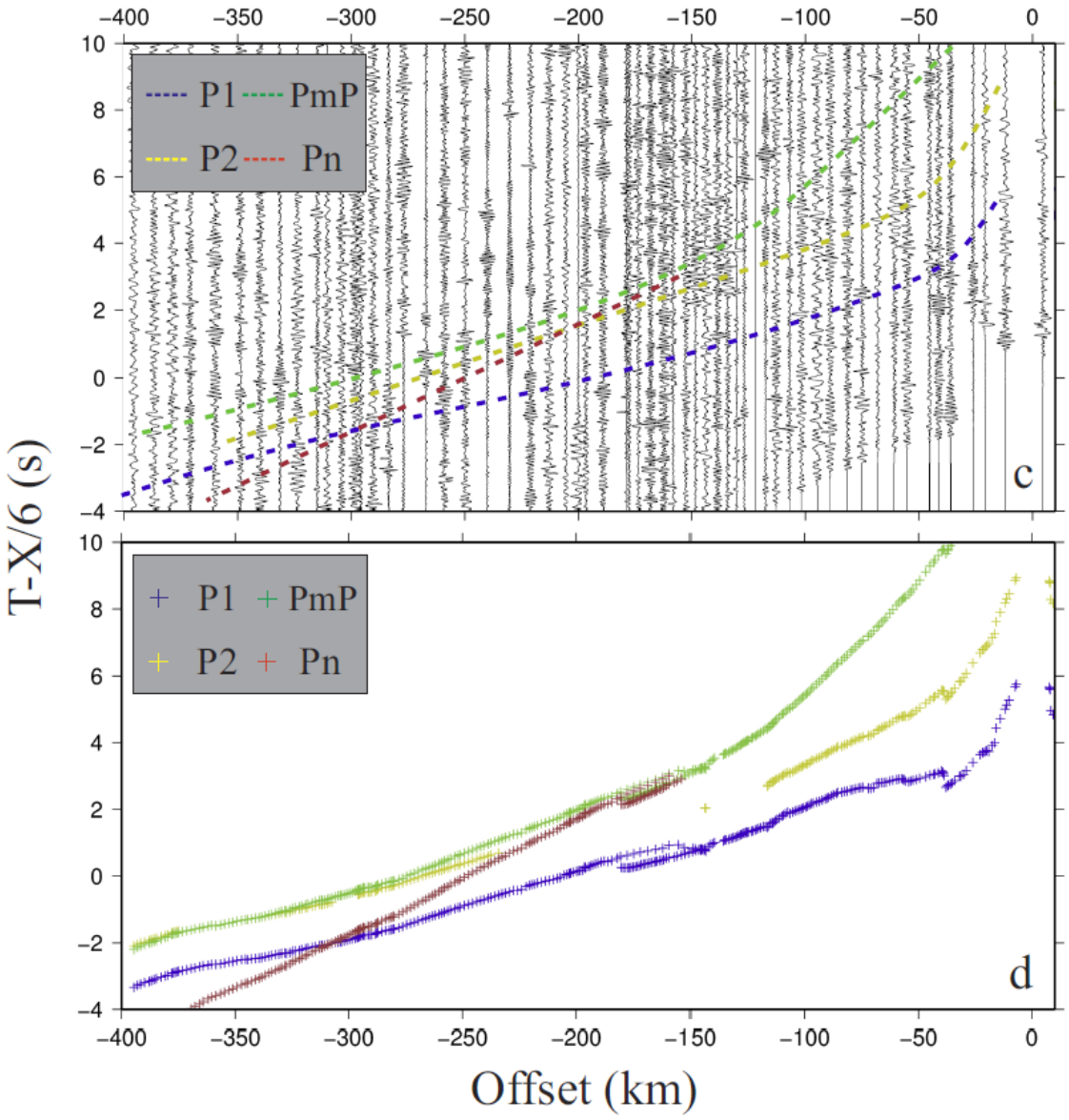

Figure 2.3. (c) Observed waveforms for shot 10. (d) Plot of travel-time picks for shot 10. P1 and P2 are intracrustal reflections; PmP and Pn are Moho reflections and upper mantle refractions respectively. Blue crosses are P1, Yellow crosses are P2, Green crosses are PmP, and Red crosses are Pn.

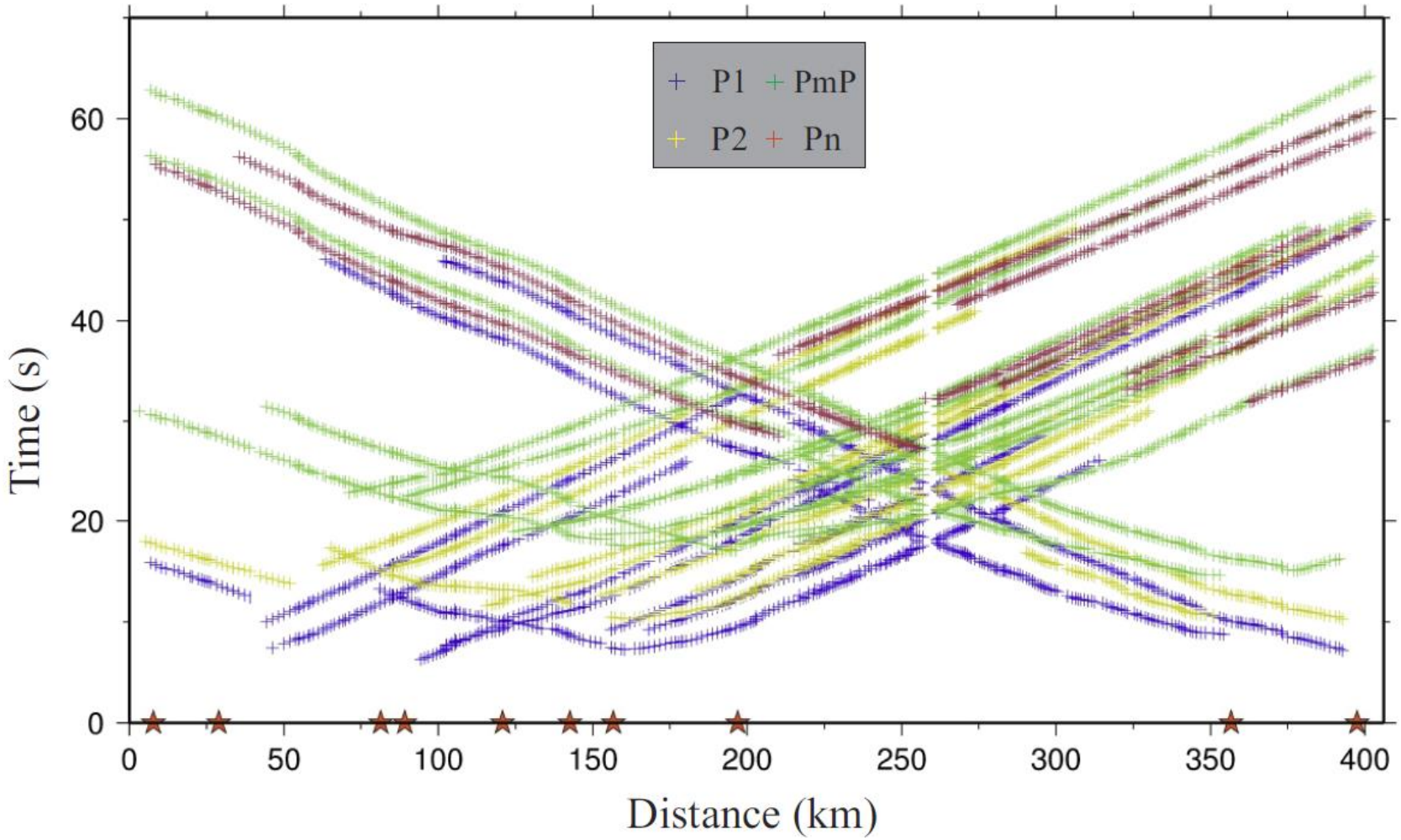
P1
PmP
P2
Pn
Time (s)
Distance (km)
0
20
40
60
0
50
100
150
200
250
300
350
400

Figure 2.3. (e) All the travel picks for the refraction and wide-angle reflection profile shots. Red stars are the shotpoints, Blue crosses are P1, Yellow crosses are P2, Green crosses are PmP, and Red crosses are Pn.

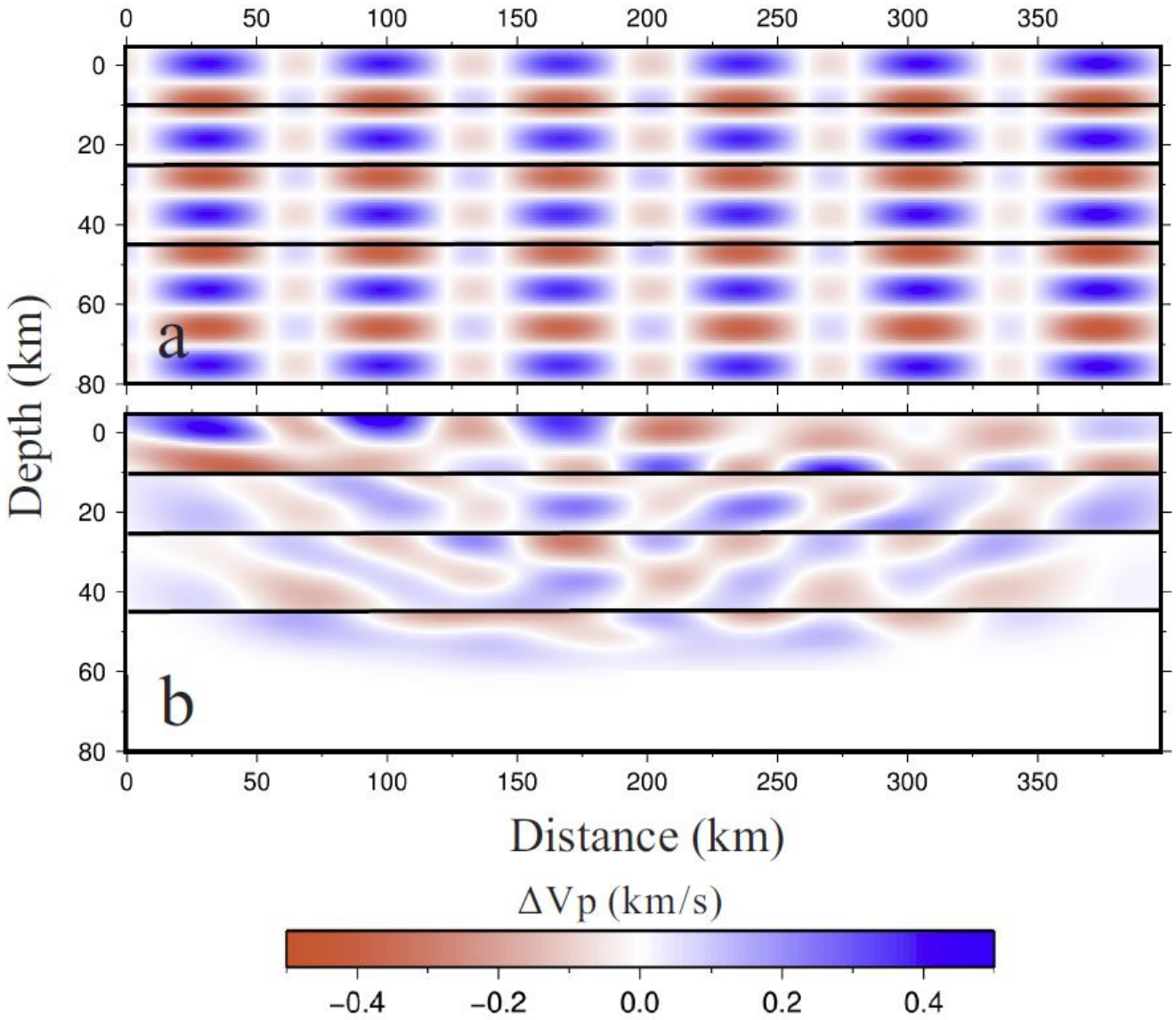
0
50
100
150
200
250
300
350
Depth (km)
a
b
Distance (km)
ΔVp (km/s)
−0.4
−0.2
0.0
0.2
0.4

Figure 2.4. (a) Initial velocity model for resolution test. The checkerboard pattern with amplitude 0.5 km/s was added over the 1D model with a velocity grid (0.44°x0.44°x10km), and the black lines are the boundaries of layers. (b) Results of resolution test. The data cover most of the area above 60km depth. Laterally, the middle part of the model (50km to 350km) also has good resolution.

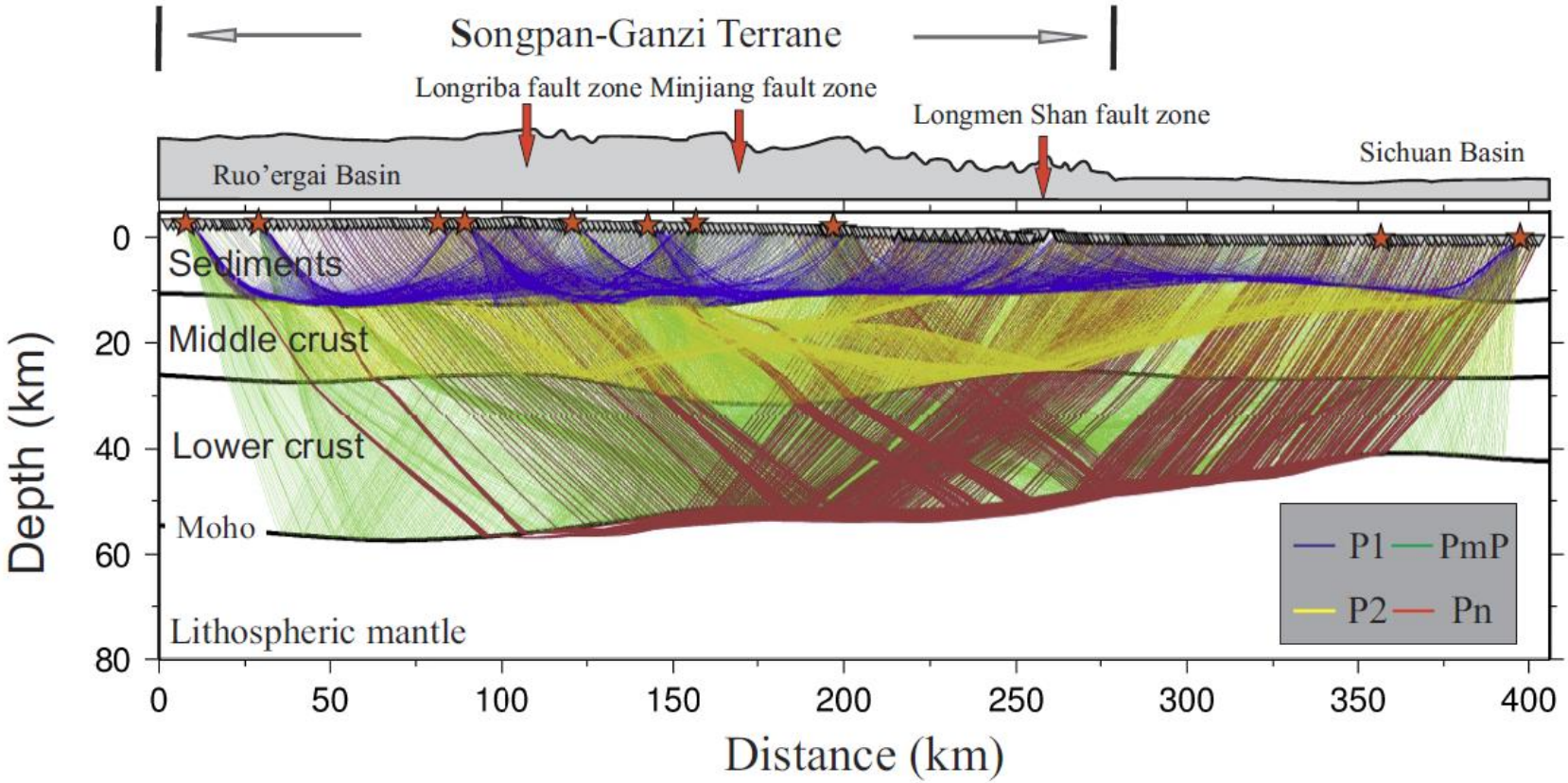
Songpan-Ganzi Terrane
Longriba fault zone
Minjiang fault zone
Longmen Shan fault zone
Ruo'ergai Basin
Sichuan Basin
Sediments
Middle crust
Lower crust
Moho
Lithospheric mantle
P1
PmP
P2
Pn
Depth (km)
Distance (km)
0
20
40
60
80
0
50
100
150
200
250
300
350
400

Figure 2.4. (c) Ray coverage for the final velocity model using refraction and reflection seismic tomography; Blue lines are P1 rays, Yellow lines are P2 rays, Green lines are PmP rays, and Red lines are Pn rays.

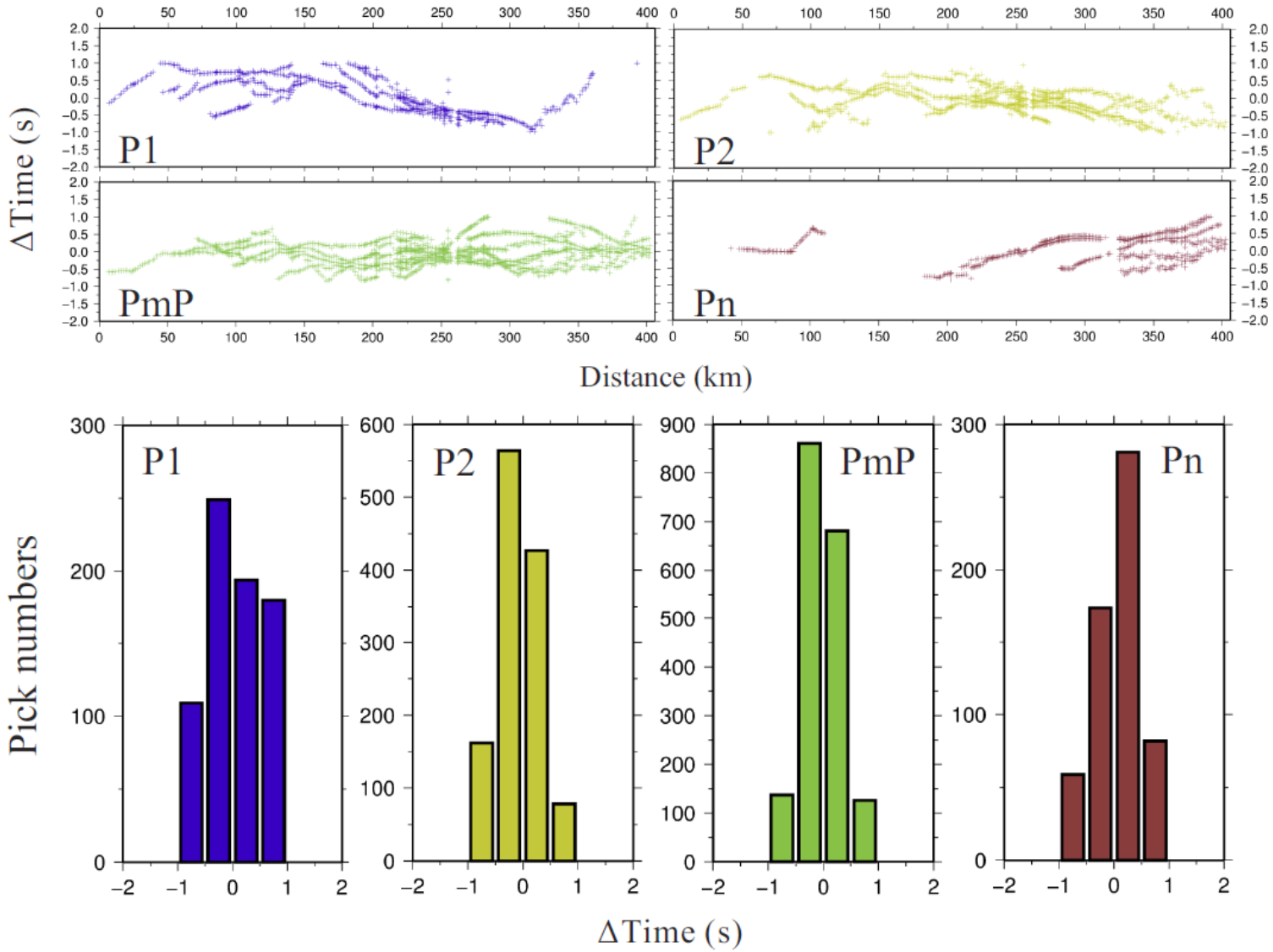
P1
P2
PmP
Pn
ΔTime (s)
Distance (km)
Pick numbers
ΔTime (s)

Figure 2.5. Traveltime residual plot. Blue is P1, yellow is P2, green is PmP, red is Pn. The upper frame shows the residuals of the picks for each phase, and the bottom frame shows histograms of the residuals that show that virtually all the picks are fitted to within -1s to 1s and most are fitted to within -0.5s to 0.5s

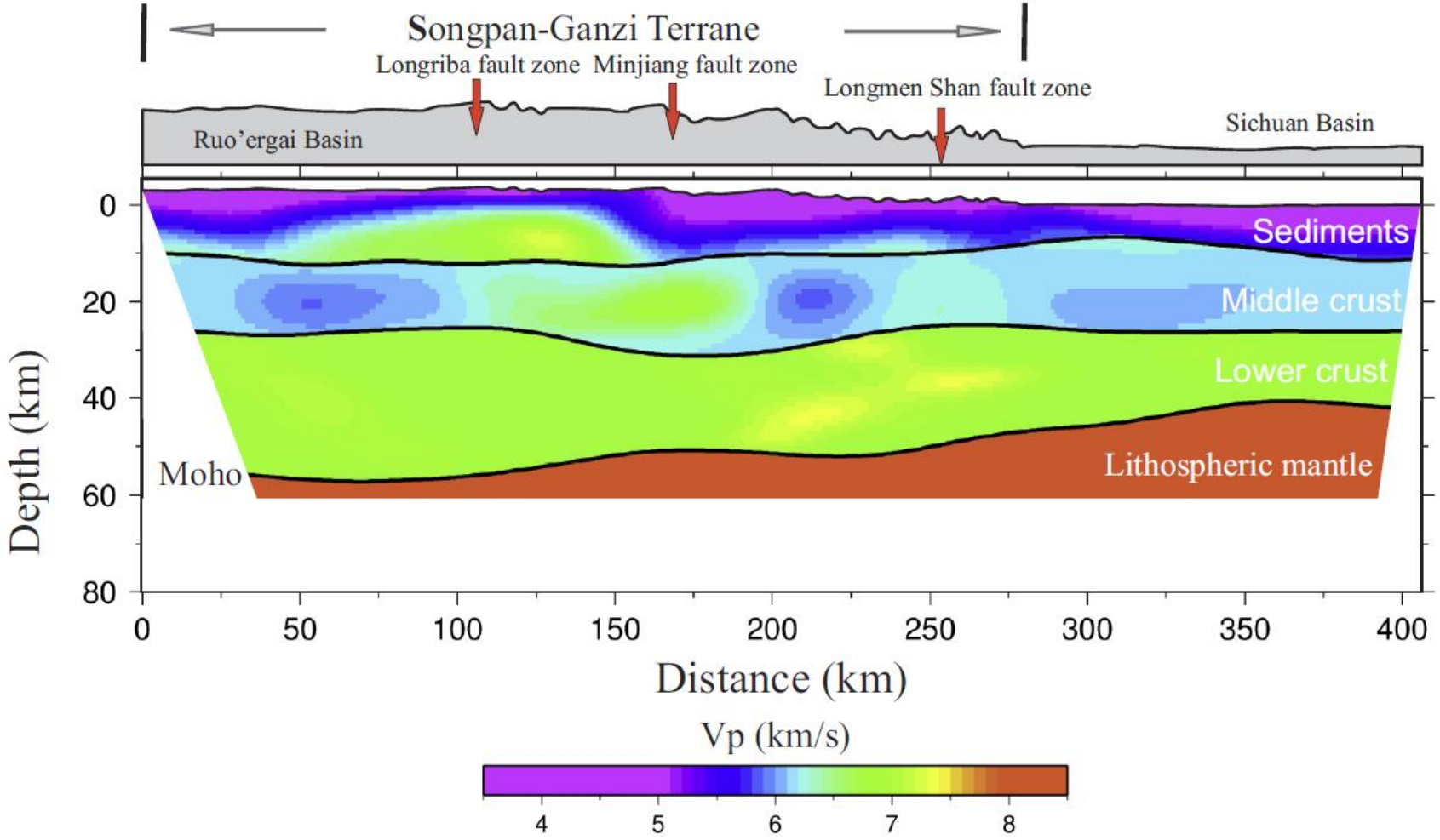

Figure 2.6. (a) Final velocity model derived from the combined stacking velocity and travel-time tomography.

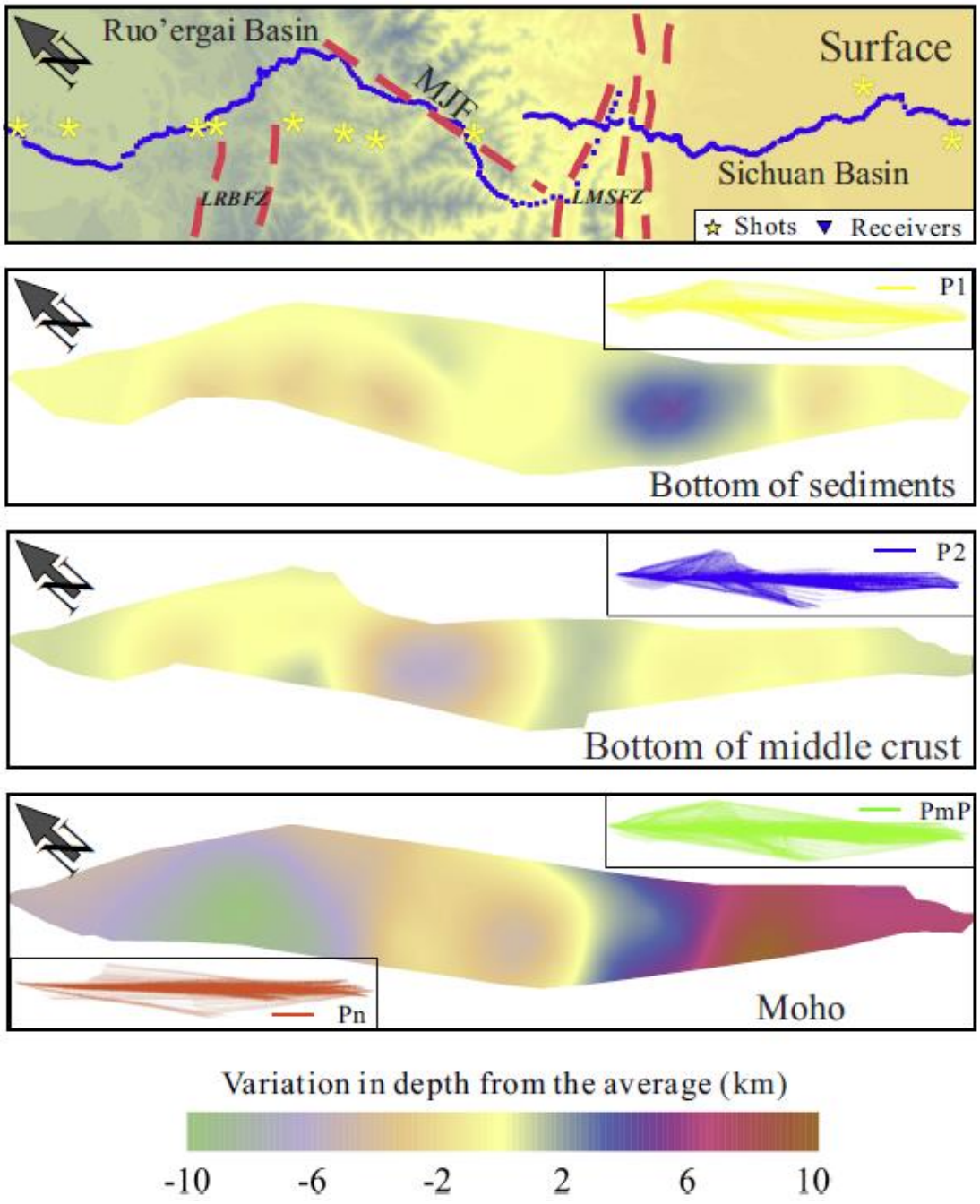

Figure 2.6. (b) Relief of interfaces from the surface to the Moho derived from the 3-D tomography. Topographic surface; yellow stars are shotpoints, small inverted black triangles are the receiver locations, bottom of upper crust (sediments), (c) bottom of middle crust, Moho. Yellow rectangles mark the approximate extent of the region with acceptable resolution.

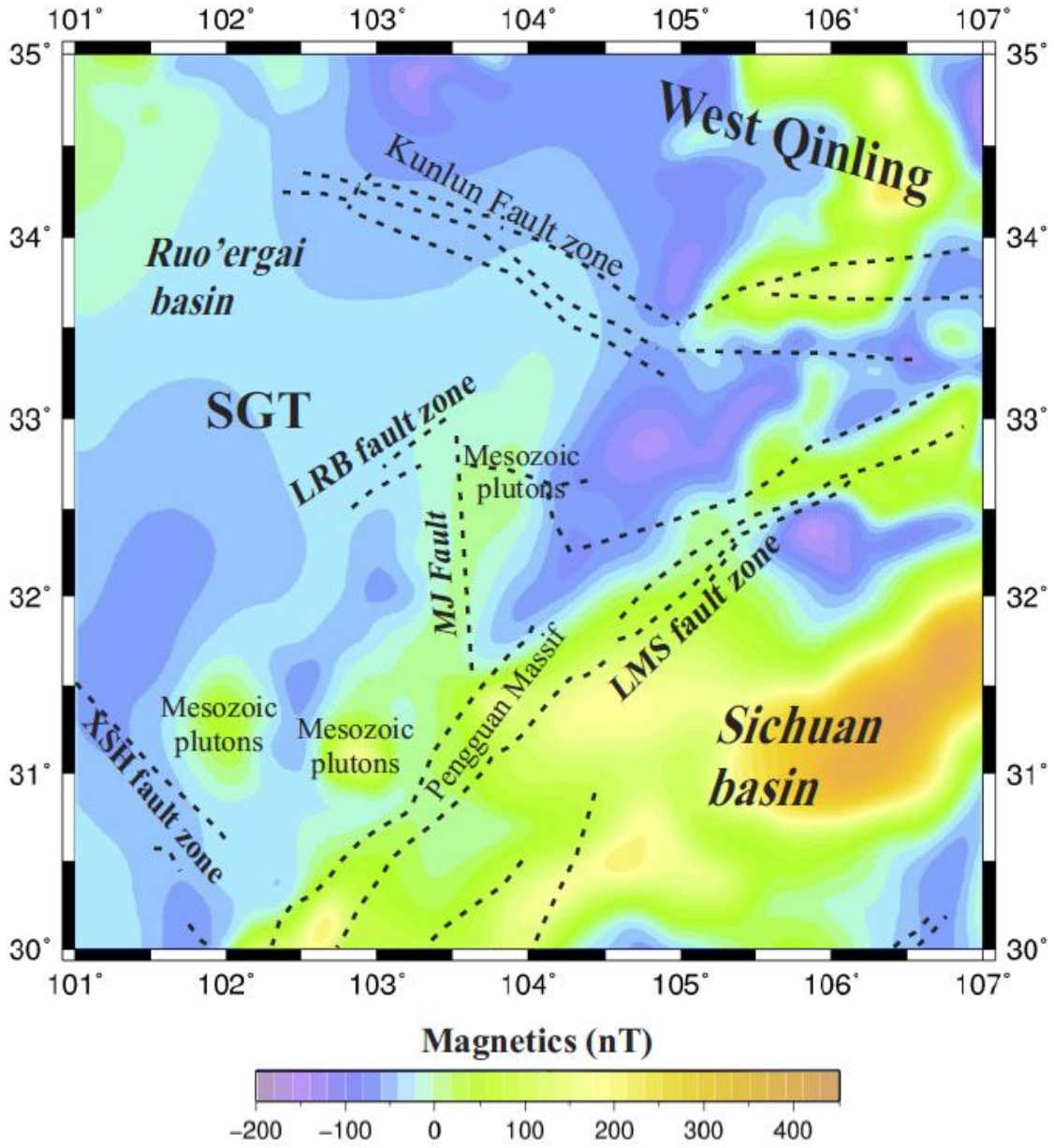

Figure 2.7. (a) Magnetic anomaly map based on data from the World Digital Magnetic Anomaly Map (WDMAM) project (Maus et al., 2007).

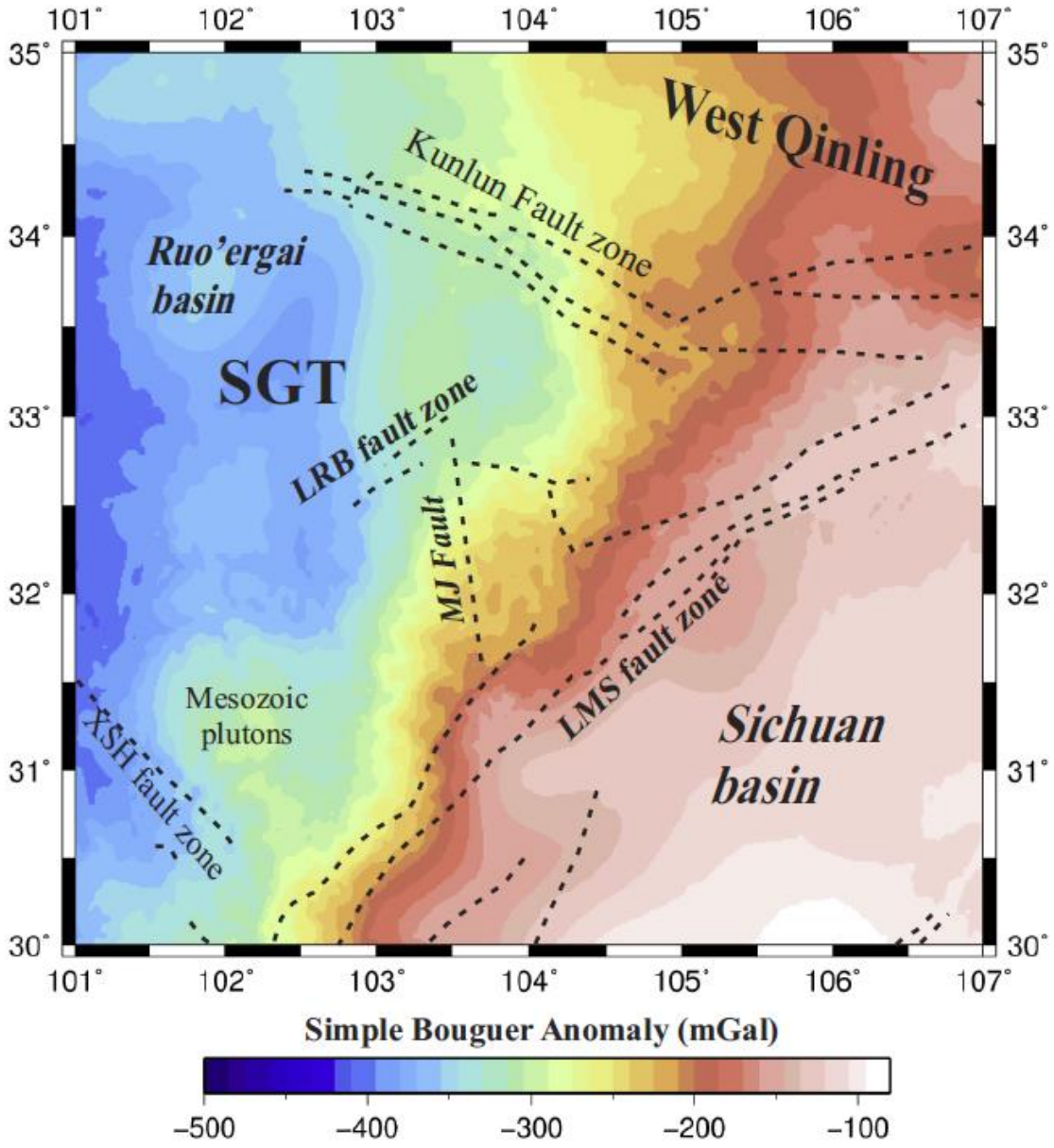

Figure 2.7. (b) Simple Bouguer gravity anomaly map based on data from the International Center for Global Earth Models (ICGEM).

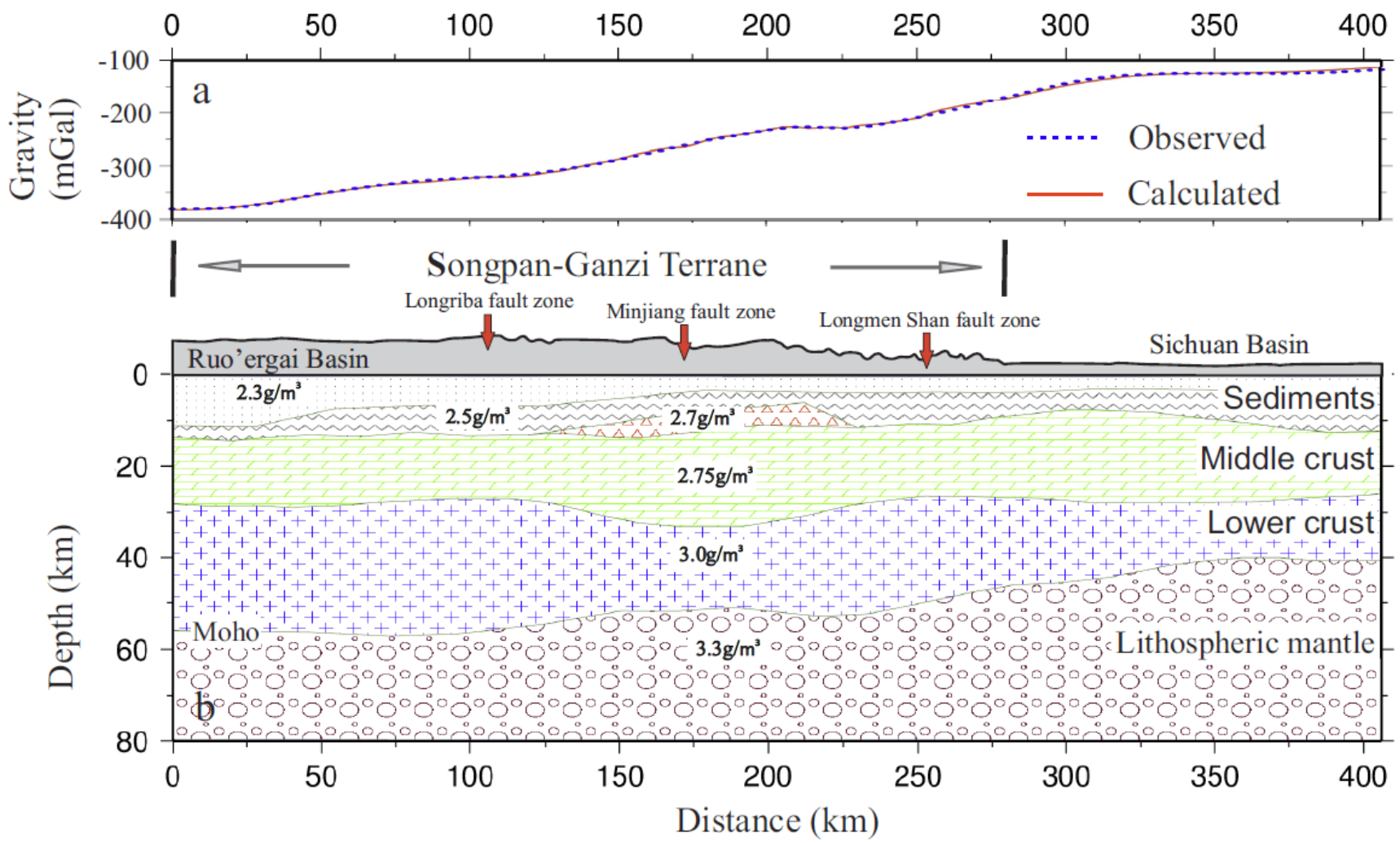
Gravity (mGal)
a
Observed
Calculated
Songpan-Ganzi Terrane
Longriba fault zone
Minjiang fault zone
Longmen Shan fault zone
Ruo'ergai Basin
Sichuan Basin
2.3g/m³
2.5g/m³
2.7g/m³
2.75g/m³
3.0g/m³
3.3g/m³
Sediments
Middle crust
Lower crust
Moho
Lithospheric mantle
b
Depth (km)
Distance (km)

Figure 2.8. (a) Observed and computed Bouguer anomalies. (b) Final 2D integrated gravity model density model. The middle and lower crust boundaries were derived from the seismic model and only the upper structure was iterated to achieve and fit between the observed and calculated gravity values.

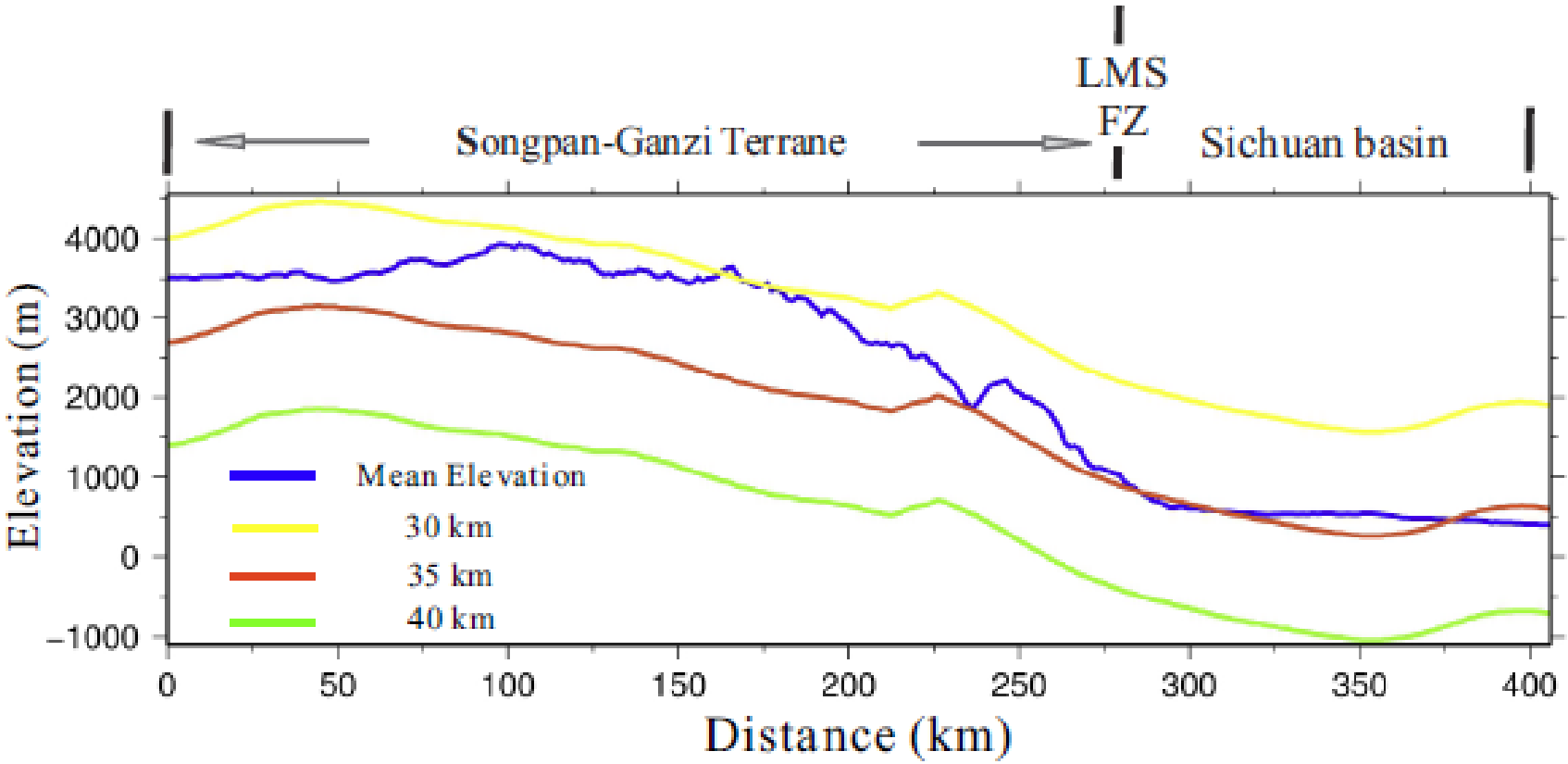
LMS
FZ
Songpan-Ganzi Terrane
Sichuan basin
Elevation (m)
4000
3000
2000
1000
0
−1000
Mean Elevation
30 km
35 km
40 km
0
50
100
150
200
250
300
350
400
Distance (km)

Figure 2.8. (c) Isostatic elevation and current mean elevation crossing LMSFZ. The calculated isostatic elevations is basing on different original crustal thickness. The blue line is current mean elevation, the yellow, red, and green lines are calculated isostatic elevations with 30 km, 35 km and 40 km original crustal thickness.

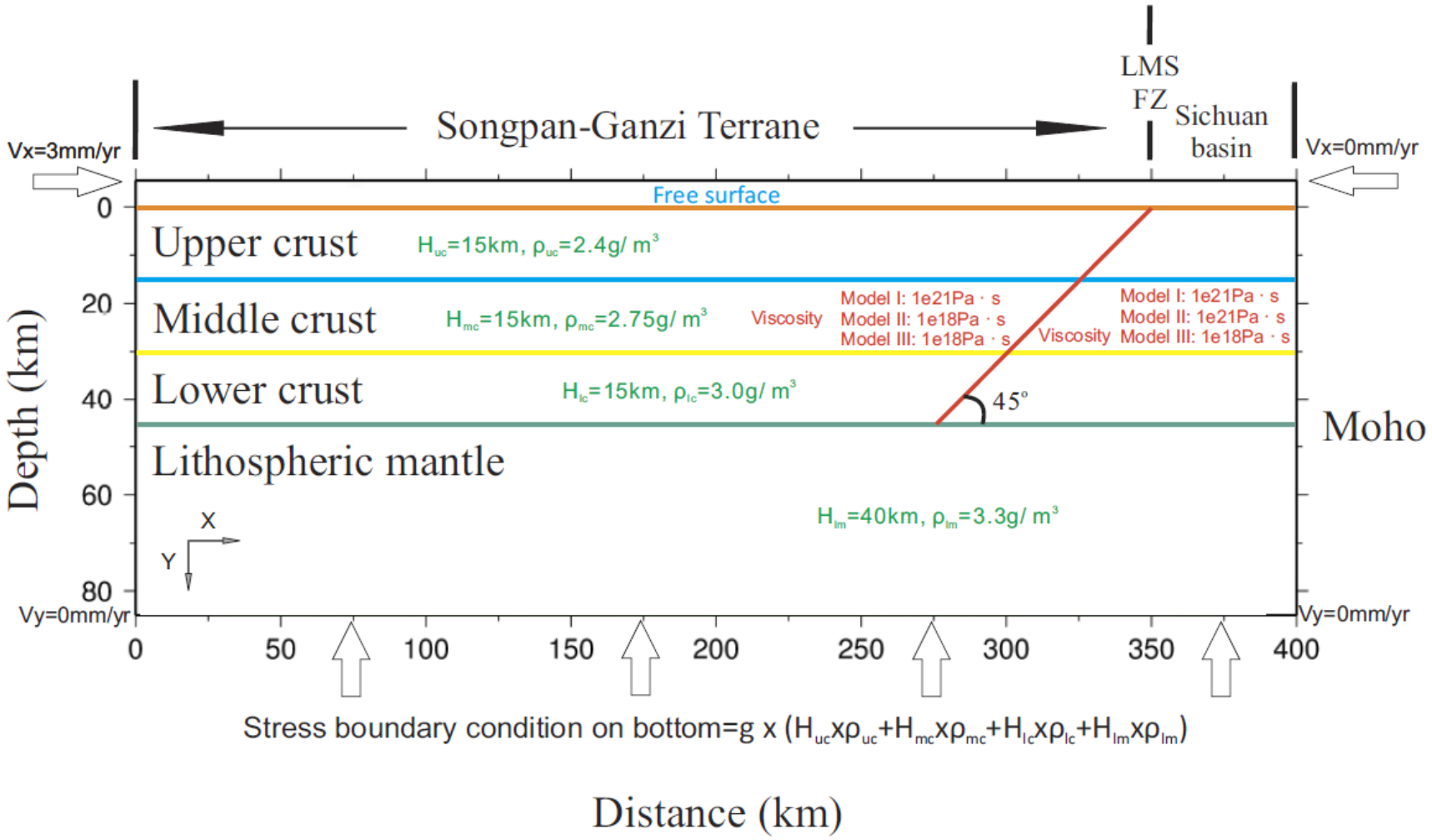
LMS
FZ
Songpan-Ganzi Terrane
Sichuan
basin
Vx=3mm/yr
Vx=0mm/yr
Free surface
Upper crust
H_{uc}=15km, ρ_{uc}=2.4g/ m^3
Middle crust
H_{mc}=15km, ρ_{mc}=2.75g/ m^3
Viscosity
Model I: 1e21Pa · s
Model II: 1e18Pa · s
Model III: 1e18Pa · s
Viscosity
Model I: 1e21Pa · s
Model II: 1e21Pa · s
Model III: 1e18Pa · s
Lower crust
H_{lc}=15km, ρ_{lc}=3.0g/ m^3
45°
Moho
Lithospheric mantle
H_{lm}=40km, ρ_{lm}=3.3g/ m^3
X
Y
Depth (km)
0
20
40
60
80
Vy=0mm/yr
Vy=0mm/yr
0
50
100
150
200
250
300
350
400
Stress boundary condition on bottom=g x ($H_{uc}x\rho_{uc}+H_{mc}x\rho_{mc}+H_{lc}x\rho_{lc}+H_{lm}x\rho_{lm}$)
Distance (km)

Figure 2.9. Initial model for numerical simulation. According to previous research, the LMSFZ dips ~45^{o} towards the west. In our models, we defined four main layers (upper crust, middle crust, lower crust and lithospheric mantle) with their densities and rheological properties. Different viscosity parameters of the middle crust are used in three models. We set the west boundary to move with a constant velocity (3mm/yr) and the east boundary is fixed.

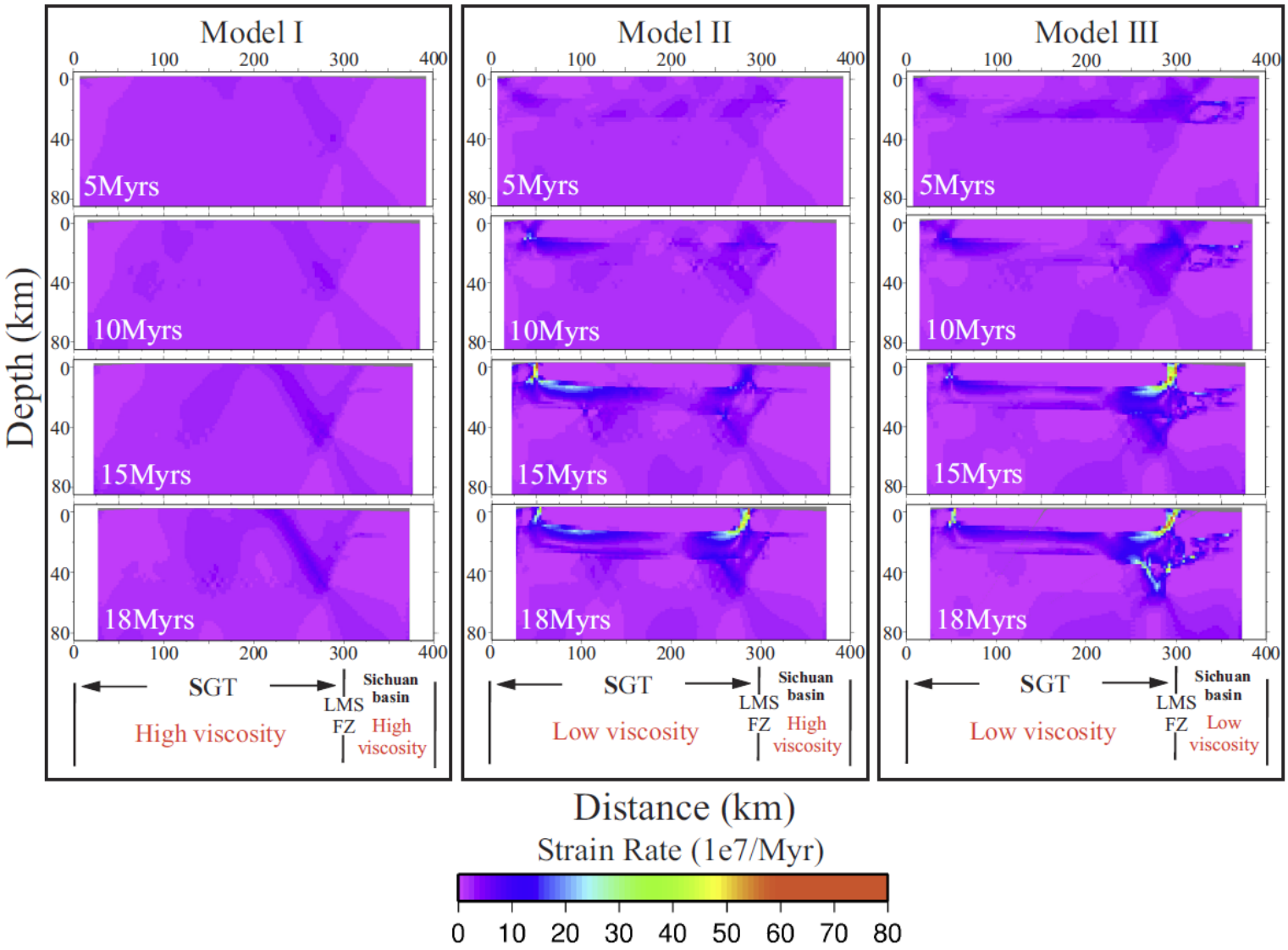
Model I
Model II
Model III
Depth (km)
0
100
200
300
400
0
40
80
5Myrs
10Myrs
15Myrs
18Myrs
SGT
Sichuan basin
LMS
FZ
High viscosity
Low viscosity
Distance (km)
Strain Rate (1e7/Myr)
0 10 20 30 40 50 60 70 80

Figure 2.10. (a) Simulation results for varying strain rates. (a) model I, (b) model II, (c) model III.

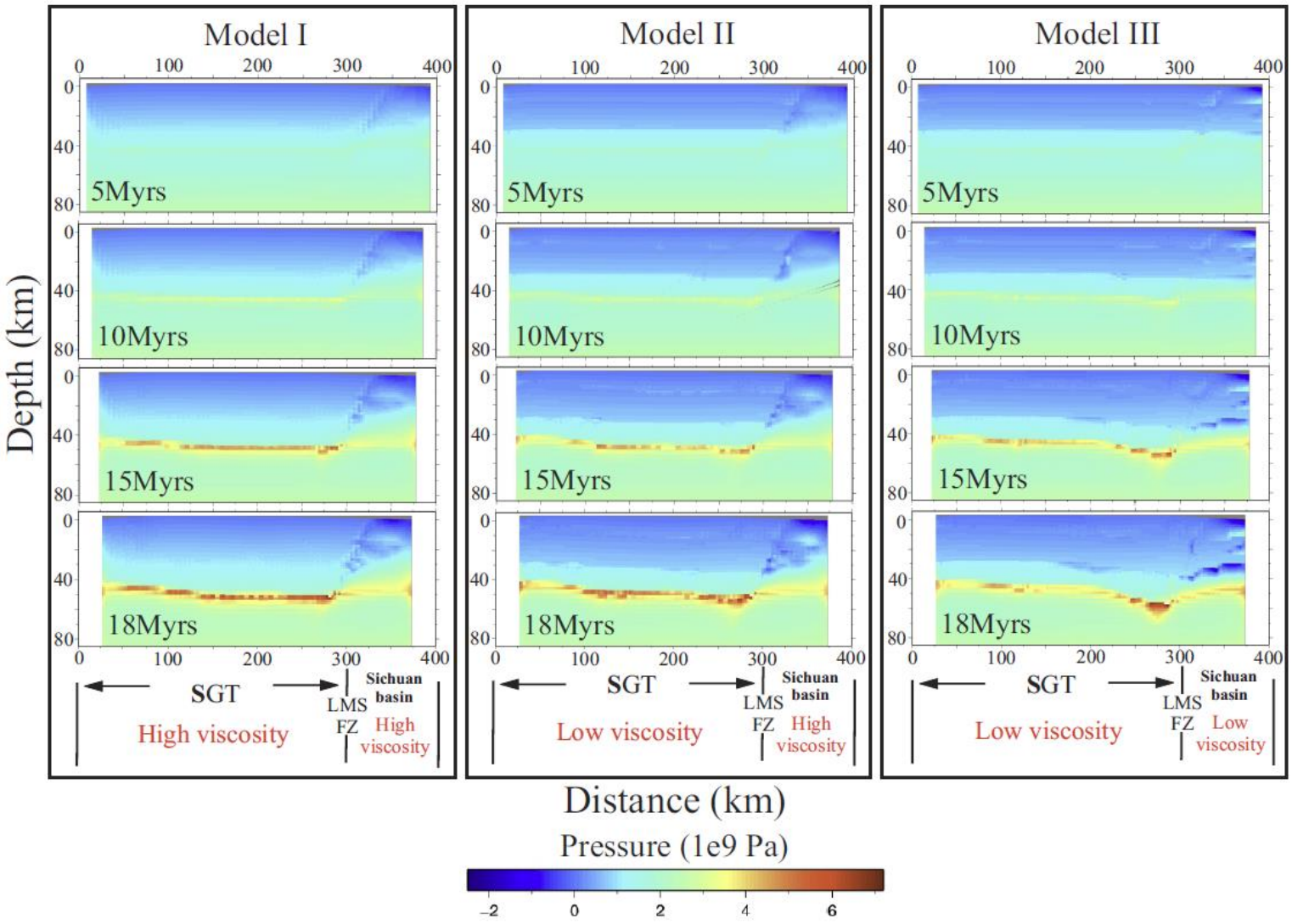
Model I
Model II
Model III
Depth (km)
5Myrs
10Myrs
15Myrs
18Myrs
SGT
LMS
FZ
Sichuan basin
High viscosity
Low viscosity
Distance (km)
Pressure (1e9 Pa)

Figure 2.10. (b) Simulation results for varying pressures. (a) model I, (b) model II, (c) model III.

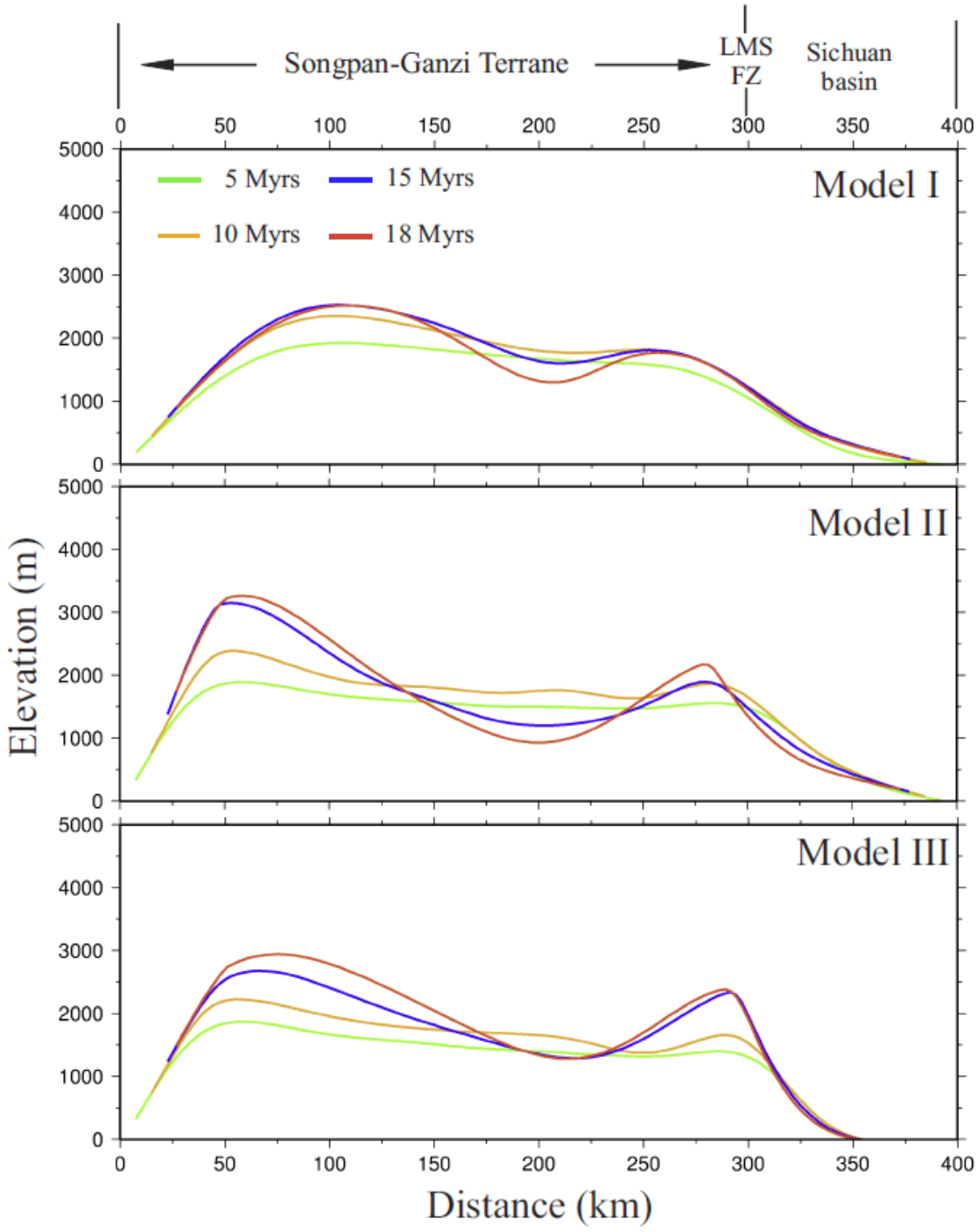

Figure 2.10. (c) Elevation profiles resulting from the simulations for 4 time intervals. model I, model II, model I. The extremely high elevations in western area are caused by the boundary effect.

REFERENCES CITED

An, Z.SH., Kutzbach, J.E., Prell, W.L., Porter S.C., 2001. Evolution of Asian monsoons and phased uplift of the Himalaya–Tibetan plateau since Late Miocene times. Nature 411, 6833 62-66.

Arrial, P.A., Billen M.I., 2013. Influence of geometry and eclogitization on oceanic plateau subduction. Earth and Planetary Science Letters 363, 34-43, http://dx.doi.org/http://dx.doi.org/10.1016/j.epsl.2012.12.011

Block, L., Royden L.H., 1990. Core complex geometries and regional scale flow in the lower crust. Tectonics 9, 557–567.

Brocher, T.M., 2005. Empirical relations between elastic wavespeeds and density in the Earth's crust. Bull. Seismol. Soc. Am. 95, 2081–2092, http://dx.doi.org/10.1785/0120050077.

Burchfiel, B.C., Royden, L.H., van der Hilst, R.D., Hager, B.H., 2008. A geological and geophysical context for the Wenchuan earthquake of 12 May 2008, Sichuan, People's Republic of China. GSA Today 18, 4-11, *http://dx.doi.org/*10.1130/GSATG18A.

Chen, L., Gerya, T., Zhang, Z., Zhu, G., Duretz, T., Jacoby, W.R., 2013. Numerical modeling of eastern Tibetan-type margin: Influences of surface processes, lithospheric structure and crustal rheology. Gondwana Research 24, 1091-1107, http://dx.doi.org/10.1016/j.gr.2013.01.003.

Chen, S.F., Wilson, J.L.C., 1996. Emplacement of the LMS Thrust—Nappe Belt along the eastern margin of the Tibetan Plateau. Journal of Structural Geology. 18, 413-430.

Chen, Y.L., Li, D.P., Zhou, J., Liu, F., Zhang, H.F., Nie, L.S., Jiang, L.T., Song, B., Liu, X.M., Wang. Z., 2009. U-Pb dating, geochemistry, and tectonic implications of the Songpan-Ganzi block and the LMS, China. Geochemical Journal 43, 77-99.

Clark, M.K., Royden, L.H., 2000. Topographic ooze: Building the eastern margin of Tibet by lower crustal flow. Geology 28, 703-706.

Clark, M.K., House, M.A., Royden, L.H., Whipple, K.X., Burchfiel, B.C., Zhang, X., Tang W., 2005. Late Cenozoic uplift of southeastern Tibet. Geology 33, 525-528, http://dx.doi.org/10.1130/G21265.1.

Cook, K.L., Royden, L.H., Burchfiel, B.C., Lee, Y.H., Tan X., 2013. Constraints on Cenozoic tectonics in the southwestern Longmen Shan from low-temperature thermochronology. Lithosphere 5. 393-406, http://dx.doi.org/10.1130/L263.1.

Dix C.H., 1955. Seismic velocities from surface measurements. Geophysics 20, 68–86.

Drucker, D.C., Prager W., 1952. Soil mechanics and plastic analysis for limit design. Quarterly of Applied Mathematics. 10, 157–165.

Dong, S.W., Li, T.D., Gao, R., Hou, H.SH., Li, Q.SH., Li, Y.K., Zhang, S.H., Keller, G.R., Liu, M., 2011. A Multidisciplinary Earth Science Research Program in China. Eos Trans. AGU, 92, 313-314, *http://dx.doi.org/*10.1029/2011EO380001.

Evans, B., Kohlstedt, D.L., 1995, Rheology of rocks. AGU Reference Shelf 3, 148-165, http://dx.doi.org/10.1029/RF003p0148

Gardner, G.H.F., Gardner, L.W., Gregory A.R., 1974. Formation velocity and density — the diagnostic basics for stratigraphic traps. Geophysics 39, 770–780.

Godard, V., Pik, R., Lavé, J., Cattin, R., Tibari, B., de Sigoyer, J., Pubellier, M., Zhu, J., 2009. Late Cenozoic evolution of the central LMS, eastern Tibet: Insight from (U-Th)/He thermochronometry. Tectonics 28, TC5009, doi:10.1029/2008TC002407.

Guo, X.Y., Encarnacion, J., Xu, X., Deino, A., Li, Z.W., Tian, X.B., 2012. Collision and rotation of the South China block and their role in the formation and exhumation of ultrahigh pressure rocks in the Dabie Shan orogeny. Terra Nova 24, 339-350, http://dx.doi.org/10.1111/j.1365-3121.2012.01072.x.

Guo, X.Y., Gao, R., Keller, G.R., Xu, X., Wang H.Y., Li W.H., 2013. Imaging the crustal structure beneath the eastern Tibetan Plateau and implications for the uplift of the LMS range. Earth Planet. Sci. Lett. 379, 72-80, http://dx.doi.org/10.1016/j.epsl.2013.08.005.

Harrowfield, M.J., Wilson, C.J.L., 2005. Indosinian deformation of the Songpan Garzê fold belt, northeast Tibetan Plateau. Journal of Structural Geology 27, 101-117, http://dx.doi.org/10.1016/j.jsg.2004.06.010.

Huang, M.H., Bürgmann, R., Freed, A.M., 2014. Probing the lithospheric rheology across the eastern margin of the Tibetan Plateau. Earth and Planetary Science Letters, 396, 88-96, http://dx.doi.org/10.1016/j.epsl.2014.04.003

Hubbard, J., Shaw J.H., 2009. Uplift of the LMS and Tibetan plateau, and the 2008 Wenchuan (M = 7.9) earthquake. Nature 458, 194-197, http://dx.doi.org/10.1038/nature07837.

Kirby, E., Reiners, P.W., Krol, M.A., Whipple, K.X., Hodges, K.V., Farley, K.A., Tang, W.Q., Chen, Z.L., 2002. Late Cenozoic evolution of the eastern margin of the Tibetan Plateau: Inferences from 40Ar/39Ar and (U-Th)/He thermochronology. Tectonics 21, 1-20, http://dx.doi.org/10.1029/2000TC001246.

Lease, R.O., Burbank, D.W., Clark, M.K., Farley, K.A., Zheng, D., Zhang, H., 2011. Middle Miocene reorganization of deformation along the northeastern Tibetan Plateau. Geology 39, 359-362.

Li, H.Y., Shen, Y., Huang, Z., Li, X., Gong, M., Shi, D., Sandvol, E. Li A., 2014a. The distribution of the mid-to-lower crustal low-velocity zone beneath the northeastern Tibetan Plateau revealed from ambient noise tomography. J. Geophys. Res. Solid Earth, 119, 1954–1970, *doi:10.1002/2013JB010374.*

Li, Z., Jia, D., Chen, W., Yin, H., Shen, L., Sun, C., Zhang, Y., Li, Y., Li, S., Zhou, X., Li, H., Jian, G., Zhang, M., Cui, J., 2014b. Late Cenozoic east–west crustal shortening in southern Longmen Shan, eastern Tibet: Implications for regional stress field changes. Tectonophysics 623, 169-186, http://dx.doi.org/10.1016/j.tecto.2014.03.033.

Liu, Q.Y., van der Hilst, R.D., Li, Y., Yao, H.J., Chen, J.H., Guo, B., Qi, S.H., Wang, J., Huang, H., Li, S.C., 2014. Eastward expansion of the Tibetan Plateau by crustal flow and strain partitioning across faults, Nature Geoscience 7, 361-365, http://dx.doi.org/10.1038/ngeo2130

Liu, S.G., Luo, Z.L., Dai, S.L., Dennis, A., Wilson, C.J.L., 1996. The uplift of the Longmenshan Thrust Belt and Subsidence of the West Sichuan Foreland Basin, Acta Geologica Sinica-English Edition 9, 16-26, http://dx.doi.org/10.1111/j.1755-6724.1996.mp9001002.x.

Liu, S.G., Deng, B., Li, Z.W., Sun, W., 2012. Architecture of basin-mountain systems and their influences on gas distribution: A case study from the Sichuan basin, South China. Journal of Asian Earth Sciences 47, 204-215, http://dx.doi.org/10.1016/j.jseaes.2011.10.012.

Mareschal, J.C., Jaupart, C., 2013. Radiogenic heat production, thermal regime and evolution of continental crust. Tectonophysics 609, 524-534, http://dx.doi.org/10.1016/j.tecto.2012.12.001.

Maus, S., Sazonova, T., Hemant, K., Fairhead, J.D., Ravat D., 2007. National geophysical data center candidate for the world digital magnetic anomaly map. Geochemistry, Geophysics, Geosystems 8, *Q06017, http://dx.doi.org/*10.1029/2007GC001643.

Moresi, L.N., Dufour, F., Mühlhaus, H.B., 2003. A Lagrangian integration point finite element method for large deformation modeling of viscoelastic geomaterials. Journal of Computational Physics 184, 476-497, http://dx.doi.org/10.1016/S0021-9991(02)00031-1.

Rawlinson N., Urvoy, M., 2006. Simultaneous inversion of active and passive source datasets for 3-D seismic structure with application to Tasmania. Geophys. Res. Lett. 33, L24313, http://dx.doi.org/10.1029/2006GL028105.

Ren, J.J., Xu, X.W., Yeats, R.S., Zhang, S.M., Ding, R., Gong, Z., 2013. Holocene paleoearthquakes of the Maoergai fault, eastern Tibet. Tectonophysics 590, 121-135, http://dx.doi.org/10.1016/j.tecto.2013.01.017.

Richardson, N.J., Densmore, A.L., Seward, D., Fowler, A., Wipf, M., Ellis, M.A., Zhang Y., 2008. Extraordinary denudation in the Sichuan basin: Insights from low-temperature thermochronology adjacent to the eastern margin of the Tibetan Plateau. J. Geophys. Res. 113, B0409, http://dx.doi.org/10.1029/2006JB004739.

Robert, A., Pubellier, M., De Sigoyer, J., Vergne, J., Lahfid, A., Cattin, R., Findling, N., Zhu, J., 2010. Structural and thermal characters of the LMS (Sichuan, China). Tectonophysics 491, 165-173, http://dx.doi.org/doi:10.1016/j.tecto.2010.03.018.

Roger, F., Malavieille, J., Leloup, Ph.H., Calassou, S., Xu, Z., 2004. Timing of granite emplacement and cooling in the Songpan–Garzê Fold Belt (eastern Tibetan Plateau) with tectonic implications. Journal of Asian Earth Sciences 22, 465-481, http://dx.doi.org/10.1016/S1367-9120(03)00089-0.

Royden, L.H., Burchfiel, B.C., King, R.W., Wang, E., Chen, Z.L., Shen, F., Liu, Y.P., 1997. Surface Deformation and Lower Crustal Flow in Eastern Tibet, Science, 276. 788-790.

Shen, Z.K., Lü, J., Wang, M., Burgmann, R., 2005. Contemporary crustal deformation around the southeast borderland of the Tibetan Plateau. J. Geophys. Res. 110, B11409, http://dx.doi.org/10.1029/2004JB003421.

Sun, W.D., Li, S.G., Chen, Y.D., Li, Y.J., 2002. Timing of synorogenic granitoids in the South Qinling, central China: Constraints on the evolution of the Qinling‐Dabie orogenic belt. The Journal of geology 110, 457-468, http://dx.doi.org/10.1086/340632.

Sun, Y.J., Liu, M., Dong, S.W., Zhang, H., Shi, Y.L., 2013. Geodynamic modeling of the contrasting lithospheric deformation across the northeastern and eastern margins of the Tibetan Plateau. Acta Geologica Sinica (English Edition), 87, 154.

Tapponnier, P., Peltzer, G., Le Dain, A.Y., Armijo, R., Cobbold, P., 1982. Propagating extrusion tectonics in Asia: New insights from simple experiments with plasticine. Geology 10, 611-616.

Wang, C.Y., Han, W.B., Wu, J.P., Lou, H., Chan, W.W., 2007. Crustal structure beneath the eastern margin of the Tibetan Plateau and its tectonic implications. J. Geophys. Res. 112, B07307, doi:10.1029/2005JB003873.

Wang, C.Y., Zhu, L., Lou, H., Huang, B.S., Yao, Z., Luo, X., 2010a. Crustal thicknesses and Poisson's ratios in the eastern Tibetan Plateau and their tectonic implications. J. Geophys. Res. 115, *B11301, http://dx.doi.org/*10.1029/2010JB007527.

Wang, C.Y., Lou, H., Silver, P.G., Zhu, L.P., Chang L.J., 2010b. Crustal structure variation along 30 N in the eastern Tibetan Plateau and its tectonic implications. Earth Planet. Sci. Lett. 289, 367-376, http://dx.doi.org/10.1016/j.epsl.2009.11.026.

Wang, E., Kirby, E., Furlong, K.P., van Soest, M., Xu, G.Q., Shi, X., JJ Kamp, P., Hodges K.V., 2012a. Two-phase growth of high topography in eastern Tibet during the Cenozoic. Nature Geoscience 5, 640-645, http://dx.doi.org/10.1038/ngeo1538.

Wang, Y.X., Mooney, W.D., Yuan, X.C., Okaya, N., 2012b. Crustal structure of the northeastern Tibetan Plateau from the southern Tarim basin to the Sichuan basin, China. Tectonophysics 584, 191-208, http://dx.doi.org/10.1016/j.tecto.2012.09.003.

Wdowinski, S., Axen, G.J., 1992. Isostatic rebound due to tectonic denudation: A viscous flow model of a layered lithosphere. Tectonics 11, 303–315.

Wood, J.R., Hewett T.A., 1982. Fluid convection and mass transfer in porous sandstones—A theoretical model. Geochimica et Cosmochimica Acta 46, 1707-1713.

Xiao, L., Zhang, H.F., Clemens, J.D., Wang, Q.W., Kan, Z.Z., Wang, K.M., Ni, P.Z., Liu, X.M., 2007. Late Triassic granitoids of the eastern margin of the Tibetan Plateau: geochronology, petrogenesis and implications for tectonic evolution. Lithos 96, 436-452, http://dx.doi.org/10.1016/j.lithos.2006.11.011.

Xu, Z.Q., Ji, S.C., Li, H.B., Hou, L.W., Fu, X.F., Cai, Z.H., 2008a. Uplift of the LMS range and the Wenchuan earthquake, Episodes 31, 291-301.

Xu, X.W., Wen, X.Z., Chen, G.H., Yu, G.H., 2008b. Discovery of the Longriba fault zone in eastern Bayan Har block, China and its tectonic implication. Science in China Series D: Earth Sciences 51, 1209–1223.

Yin, A., Harrison, T.M., 2000. Geologic evolution of the Himalayan-Tibetan orogeny: Annual Reviews of Earth and Planetary Sciences 28, 211-280.

Zandt, G., Ammon , C.J., 1995. Continental crust composition constrained by measurements of crustal Poisson's ratio. Nature 374, 152-154.

Zelt, C.A., Forsyth, D.A., 1994. Modeling wide-angle seismic data for crustal structure: southeastern Grenville province. J. Geophys. Res. 99, 11687–11704.

Zhang, H.F., Zhang, L., Harris, N., Jin, L.L., Yuan, H.L., 2006. U–Pb zircon ages, geochemical and isotopic compositions of granitoids in Songpan–Garze fold belt, eastern Tibetan Plateau: constraints on petrogenesis and tectonic evolution of the basement. Contribution to Mineralogy and Petrology 152, 75–88, http://dx.doi.org/10.1007/s00410-006-0095-2.

Zhang, L.Y., Ding, L., Pullen, A., Xu, Q., Liu, D.L., Cai, F.L., Yue, Y.H., Lai, Q.Z., Shi, R.D., Ducea, M.N., Kapp, P., Chapman, A., 2014. Age and geochemistry of western

Hoh-Xil-Songpan-Ganzi granitoids, northern Tibet: Implications for the Mesozoic closure of the Paleo-Tethys ocean. Lithos 190-191, 328-348, http://dx.doi.org/10.1016/j.lithos.2013.12.019

Zhang, P.Z., 2013. Beware of slowly slipping faults. Nature Geoscience 6, 323-324, http://dx.doi.org/10.1038/ngeo1811.

Zhang, P.Z., Shen, Z.K., Wang, M., Gan, W.J., Bürgmann, R., Molnar, P., Wang, Q., Niu, Z.J., Sun, J.Z., Wu, J.C., Sun, H.R., You, X.Z., 2004. Continuous deformation of the Tibetan Plateau from global positioning system data. Geology 32, 809-812, http://dx.doi.org/10.1130/G20554.1.

Zhang, Z., Deng, Y., Chen, L., Wu, J., Teng, J., Panza, G., 2013. Seismic structure and rheology of the crust under mainland China. Gondwana Research 23, 1455-1483, http://dx.doi.org/10.1016/j.gr.2012.07.010.

Zhang, Z., Deng, Y., Teng, J., Wang, C., Gao, R., Chen, Y., Fan, W., 2011. An overview of the crustal structure of the Tibetan plateau after 35 years of deep seismic soundings, Journal of Asian Earth Sciences 40, 977-989, http://dx.doi.org/10.1016/j.jseaes.2010.03.010.

Zhang, Z.J., Wang, Y.H., Chen, Y., Houseman, G.A., Tian, X.B., Wang, E.C., Teng, J.W., 2009. Crustal structures across Longmenshan fault belt from passive source seismic Profiling. Geophys. Res. Lett. 36, L17310, http://dx.doi.org/10.1029/2009GL039580

CHAPTER 3: Imaging Igneous Basement Structures in the Panhandle Field of the Western Anadarko Basin by Integrating 3D Seismic, Gravity, and Magnetic Data

Chapter 3: Imaging Igneous Basement Structures in the Panhandle Field of the Western Anadarko Basin by Integrating 3D Seismic, Gravity, and Magnetic Data

ABSTRACT

Panhandle-Hugoton is the largest North American gas field in which Panhandle Field includes the Panhandle oil rim and the west and east Panhandle gas fields. The igneous basement beneath the basin is of significant importance in controlling the structural distribution of overlying sediments and the distribution of natural resources such as oil, natural gas and minerals as well. The area that is targeted in this study is located in the northern Texas Panhandle Basin field, southwestern Anadarko Basin. Integrated 3D seismic, magnetic and gravity data are used in this paper to map basement structures in the Panhandle Field of north Texas. The distribution of basement structures can be affected by large-scale tectonic events to produce the traps. In this area, the Amarillo Uplift or buried Amarillo Mountains may be considered as the northwestern subsurface extension of the Wichita Mountains. Gravity and magnetic data are useful tools to identify these igneous basement structures. High-resolution 3D seismic data were collected in Gray County, Texas. I employ 3D travel-time tomography to help us interpret the seismic data. And find a flat, less deformed granite basement overlays gabbro, the gabbro dip to southeast in this survey area. The overlaid sediments exhibit the same relief with basement. The flat Permian sediments,

disconformity between Permian sediments and igneous basement, unconformity between granite and gabbro indicate the complex tectonic history in this region.

INTRODUCTION

The area that is targeted in this study is located in the northern Texas Panhandle Basin field, southwestern Anadarko Basin. Panhandle-Hugoton is the largest North American gas field with variable gas composition (Sorenson, 2005) (Figure 3.1). The asymmetric Anadarko Basin formed during the Early Pennsylvanian Ouachita-Marathon orogeny when the super-continent Pangaea formed from the convergence between the Laurasian and Gondwanan plates (Kluth, 1986). Basement of the Anadarko Basin contains the oldest rocks of Texas and a complex accretionary collage of island-arc and inter-arc sediments (1.79-1.71 Ga), which was later intruded by extensive felsic or bimodal volcanics of 1.4-1.34 Ga age (Thomas et al., 1984). The remains of a Cambrian failed rift were covered by carbonates in the Anadarko Basin during early Paleozoic, and the aulacogen was reactivated by the collision between Laurasian and Gondwanan plates that formed the Ouachita Mountains (Buckey, 2012). The Wichita Mountain–Amarillo Uplift chain is the southern part of the Southern Oklahoma Aulacogen and part of the Ancestral Rocky Mountains. It was thrusted upward and eroded down to igneous basement during late Pennsylvanian (Keller and Stephenson, 2007; Ye et al., 1996). The basin was filled by the Granite Wash that is the result of the erosion of uplifts that exposed the igneous basement (Dutton and Garrett, 1989). The Granite Wash was later combined with fluvial deltaic sediments from the north and east at nearly the end of the Pennsylvanian (Johnson, 1989). In the Early Permian, the Amarillo Uplift separated the Anadarko Basin from the west Texas Permian basin

(Sorenson, 2005). The marine carbonates that resulted from the uplift covered the basin and extended eastward towards the Kansas- Missouri state line (Jorgensen et al, 1993). The massive Brown Dolomite was underlain by interbedded carbonates and coarse clastics in the Panhandle Field and the Palo Duro Basin (Handford and Dutton, 1980). The top seal consists of Permian evaporites which cover the Wolfcampian carbonates (Sorenson, 2005). During the Early Permian, hydrocarbons had already been generated in the deep Anadarko Basin from all potential source rocks. The Amarillo Uplift trapped hydrocarbons with drape structures immediately after deposition of the Permian evaporate. The mid-continent Permian reservoirs contain most of the oil and gas (Sorenson, 2005).

This study is focused on the eastern Texas Panhandle, which is on the top of the Amarillo Wichita Uplift (Figure 3.1). I identified the regional tectonic structures using public domain regional gravity and magnetic data. I use local proprietary aeromagnetic data and 3D seismic data to identify and interpret Precambrian-Cambrian granite igneous basement structures. I estimate depths executing Euler deconvolution of the local magnetic data. I integrate the results obtained from these geophysical methods to understand the details of the Cambrian-Precambrian. Then, I integrate the results to interpret the structural and tectonic history of the igneous basement.

GEOLOGICAL BACKGROUND AND STRATIGRAPHY

The Southern Oklahoma Aulacogen is a major structural feature in my study area. The aulacogen trends to the northwest from the Cambrian rifted margin of Laurentia in northeastern Texas, crossing through southwestern Oklahoma, possibly into Colorado and Utah. The southeast end of the aulacogen underlies the Ouachita

orogenic belt (Buckey, 2012). In Cambrian time, rifting of the southern margin of North America led to the development of a large deep-water basin (Thomas and Astini, 1996). The Anadarko, Ardmore, and Hardeman Basins, as well as the Wichita and Amarillo Uplifts, are all major Paleozoic structures that lie within the aulacogen region (Brewer et al., 1983). This region was uplifted during the collision of the North American plate with the European and African - South American plates to form the Ouachita orogenic belt (Buckey, 2012). The late Pennsylvanian marked the end of the continental collision (Ross, 1979), and the early Permian marked the end of the deformation of the southwestern United States (Kluth and Coney, 1981). These collisional tectonic stresses reactivated basement faults and, as a result of crustal shortening, thrust faults uplifted the Wichita Mountains (Brewer et al., 1983), while the Anadarko Basin subsided and filled with 4 to 5 km of Pennsylvanian sediments (Johnson, 2008). The Anadarko Basin is the deepest and largest basin in North America with 12 to 15 km of vertical displacement (Gilbert, 1983). No significant subsequent motion has been recognized since early Permian time (Soreghan et al., 2012). The Wichita uplift is contiguous with the Amarillo Uplift and forms part of the Pennsylvanian age Ancestral Rocky Mountain orogen (Soreghan et al., 2012). The Palo Duro Basin is bounded to the north by the Amarillo Uplift (Handford and Dutton, 1980). The Hardeman Basin is separated by some structural highs to the east of the Palo Duro Basin (Means and Hubbard, 1987). The Palo Duro Basin contains about 3000 m of sedimentary rocks between Precambrian and early Permian. It deepens generally from north to south (Handford, 1979). The northwest-trending frontal fault zone of the Wichita Mountains is the central part of a 500-km-long fault system that extends from the Arbuckle Mountains in southern

Oklahoma to the Amarillo Uplift in the Texas Panhandle (Brewer, 1982). During the late Paleozoic, both strike-slip and reverse faults are active along this fault system (Keller et al., 1983). 100 km of cumulative left-lateral displacement is measured by stratigraphic markers in the Arbuckle Mountains (Lemiszki and Brown, 1982). Well logs show the faults of the Amarillo Uplift had as much as 120 km of left-lateral displacement (Brewer, 1986). Although poor exposures preclude an estimate of displacement along the frontal faults of the Wichita Uplift, structural analysis indicates two periods of convergent strike-slip faulting (Donovan, 1985). It therefore appears that the frontal faults of the Wichita Uplift may also have up to 100 km of left-lateral displacement (Lemiszki and Brown, 1982). The Amarillo Uplift consists of an en echelon series of rifting basins separating the Anadarko Basin from the Palo Duro Basin. During the Late Mississippian or Early Pennsylvanian, the Amarillo Uplift was broken into a series of rhombic grabens and horsts, probably by a left-lateral strike faulting (McGookey and Budnik, 1983). For example, the Lefors Basin in Gray County is a small 6.4 km by 12.8 km rhombic graben that contains in excess of 1,200 m of Pennsylvanian and Wolfcampian arkose (McGookey and Budnik, 1983). The Amarillo Uplift was buried in Wolfcampian time, but it continued to affect depositional patterns (McGookey and Budnik, 1983).

From the Middle Pennsylvanian until the Early Permian, the Panhandle Field area subaerially contained the northwest part of modern Wichita Mountains of southern Oklahoma that constitute the igneous basement of the Panhandle Field. The Granite Wash (coarse clastics) was eroded from the igneous basement and was deposited on the flanks and ultimately covered the igneous basement. The Early Permian carbonates that

were initially interbedded with Granite Wash were then covered by the massive Brown Dolomite. Wolfcampian carbonates (dolomite) were covered by Leonardian evaporates (Table 3.1). The Panhandle Lime represents the evaporite in the Panhandle Field area. Regional evaporate seals originally occupied approximately the same geographic area as the underlying Wolfcampian carbonates and generally separated Wolfcampian reservoirs from younger Permian and Mesozoic reservoirs. Before the end of the Permian, differential compaction of locally derived Pennsylvanian–Early Permian Granite Wash, Wolfcampian carbonates, and Leonardian evaporites over basement paleotopographic highs produced giant buried traps in the Panhandle Field.

Adjacent to the Palo Duro Basin, the Panhandle Field is fault bounded along much of its southern margin. Along the northern margin of the field, the hydrocarbon accumulation extends beyond the Amarillo Uplift bounding faults. All Wolfcampian and older reservoirs of Mississippian limestone, Cambrian–Ordovician Ellenberger dolomite and fractured igneous basement possibly contain oil or gas if found at a structural elevations corresponding to these fluid columns. To the south, only local oil accumulations are present. The greater Panhandle Field that was controlled by drape closures over eroded basement topography began to accumulate hydrocarbons soon after deposition of Permian evaporite seals. By the end of the Mesozoic, the Panhandle Filed contained most of the hydrocarbons now found in Permian reservoirs in the western Anadarko Basin (Sorenson, 2005).

DATA SETS AND METHODS

In this study, I analyzed gravity, magnetic and 3D seismic data and then integrated the results with other geospatial data of well logs, and previous research to interpret the basement structures.

Gravity data

The gravity anomaly data employed in this study were downloaded from the Pan American Center for Earth and Environmental Studies (PACES, 1995) on-line database. The gravity data were used to determine the distribution of regional tectonic structures and relate the basement structures mapped on the seismic volume to the large-scale Amarillo-Wichita Uplifts and surrounding basins. The regional data cover the area between 34°N to 38°N and 104°W to 99°W (Figure 3.2). I used complete Bouguer anomaly (CBA) gravity values from the PACES database for further mapping. I used a 2 km (~6562 ft.) grid spacing for the CBA grids. The gravity data were combined, plotted and filtered with the Geosoft/Oasis Montaj processing and analysis package. In order to highlight intracrustal structures, a residual CBA map (Figure 3.3) was calculated by subtracting the regional anomalies computed using an upward continuation of 40 km from the CBA map. To detect boundaries of local scale gravity anomalies I computed the total horizontal gradient (THG) of CBA (Figure 3.4) (Cooper and Cowan, 2006), which is defined as:

$$THG = [(\partial g / \partial x)^2 + (\partial g / \partial y)^2]^{1/2}, \quad (1)$$

where $(\partial g/\partial x)$ and $(\partial g/\partial y)$ measure the rate of change of the potential field in the x and y directions on a grid.

The CBA increases from west to east in this area, and the Amarillo-Wichita uplift is associated with a strong northwest-southeast trending gravity high (Figure 3.2).

The residual CBA map outlines the deep structure of the Amarillo-Wichita and Apishapa-Sierra Grande uplifts (Figure 3.3). The Dalhart Basin separates the Amarillo-Wichita uplift from the Apishapa-Sierra Grande uplift. The Anadarko Basin and the Palo Duro Basin are divided by the Amarillo-Wichita uplift. The relatively small-scale structures are highlighted in the THG map (Figure 3.4). The pull-apart basins by left-lateral offset during the Pennsylvanian within the Amarillo Uplift are low anomalies in the middle of Amarillo Uplift.

Magnetic data

This study has two types of total magnetic intensity (TMI) grids, including the regional magnetic data and local aeromagnetic data. The regional magnetic data with 2 km (~6562 ft.) grid spacing are also downloaded from the Pan American Center for Earth and Environmental Studies (PACES, 1995). The regional magnetic data were used to map the large-scale Amarillo Uplifts and surrounding basins. The local aeromagnetic data is a high-resolution. The related survey was carried out over Cimarex Energy's area of interest in Gray County, Texas. The purpose of the survey is to identify basement faults and fractures. North-south primary survey lines were spaced at 400-m intervals with west-east tie-lines spaced at 2,500 m. Terrain clearance was approximately 300 m. I also reduced the TMI data to the magnetic north pole so that the resulting residual magnetic anomalies (Figure 3.5) will lie directly above the magnetic source (Blakely, 1996) unless strong remnant magnetization exists. This reduced-to-pole residual TMI grid was used for further processing and filtering the magnetic data. Finally, I applied the total horizontal derivative to both regional and local magnetic data. TD is the ratio between THG and the absolute value of vertical derivative of the potential field (Cooper

and Cowan, 2006), which is expressed as:

$$TD = \arctan [THG / |\partial g / \partial z|], \quad (2)$$

where f is the potential field, and $\partial g / \partial z$ measures the rate of change of the potential field in the z direction.

In additional, the tilt angle of the horizontal gradient (Ferreira et al., 2013) was applied to local magnetic data. THG is the total horizontal gradient, which is defined as:

$$TAHG = \arctan \{|\partial THG / \partial z| / [(\partial THG / \partial x)^2 + (\partial THG / \partial y)^2]^{1/2}\}, \quad (3)$$

Where $(\partial THG/\partial x)$, $(\partial THG/\partial y)$ and $(\partial THG / \partial z)$ measure the rate of change of the total horizontal gradient in the x, y and z directions, respectively.

The Amarillo-Wichita uplift and Apishapa Sierra Grande uplift show high NW-trending magnetic anomalies in northern Texas (Figure 3.5). North of the Amarillo-Wichita uplift represents the deposit center of Anadarko Basin. The lowest anomaly is located in the Palo Duro Basin. The Dalhart Basin divides the Amarillo-Wichita uplift and Apishapa Sierra Grande uplift (Figure 3.5). The THG map shows the en-echelon basins on the Amarillo-Wichita uplift (Figure 3.6). My local magnetic anomaly indicates the biggest rifting basin is located in the Amarillo-Wichita uplift of the northern Texas (Figure 3.7). The 3D seismic data is located along the west slope of this rift basin. The NW-trending structures are mixed with a few northeast features in this area (Figure 3.8), the area with small values indicate the basement is flat, high values show the locations of slopes. Figure 3.8 shows the distributions of grabens and horsts. TAHG map of local magnetic data shows the locations of possible boundaries of magnetic anomaly bodies (Figure 3.9), the brown color indicates the possible faults. The study area is strongly controlled by NW-trending structures.

I also applied Euler deconvolution techniques to the local aeromagnetic data to determine the depth to the basement structures. The Euler deconvolution method relates the vertical and horizontal gradients of the residual TMI values to the geometry of the magnetic bodies and is given by the structural index (SI) (Barbosa et al., 1999). In addition to estimate of the basement depth, solutions obtained from Euler deconvolution help delineate source geometry. In these data, the depth of basement is shallower than 1000 m, and the basement structures are associated with Cambrian rifting and Pennsylvanian transcurrent movement that produced local pull-apart structures. Thus, I used SI values of 0 to map faults and steps of the Precambrian basement. Figure 3.10 shows the solutions plotted on the result of TD are clustered around the edges of the magnetic anomalies, where TD can be used to identify the scales of structures between THG and TAHG. As a result, some small rhombic grabens and round collapse structures are highlighted. Except for the faults in eastern corner of the 3D seismic survey area, the depths of all faults in this area are less than 1000 m, and they deepen in the northeast direction.

3D Seismic data

The high-resolution 3D seismic data were collected in Gray County, TX (Figures 3.7 and 3.11). The 3D seismic survey covered approximately 55.46 km^2 and has 274 inlines and 202 crosslines. The receiver line spacing is 201 m with a 50.29 m interval for the geophones. The source line spacing is 100.5 m with 50.29 m interval for the shots. The listening time was 2 s, and the sample interval was 2 ms. I used the post-stack Kirchhoff migration volume for interpretation purposes. Gray County is located on the top of the Amarillo-Wichita uplift. The granitic basement is extremely shallow in

this area at a depth of ~780 m and is covered by Granite Wash and dolomites. The high frequency of original pre-stack data has been cut off at 60 Hz. The well data shows the average velocity of basement and Granite Wash is ~5000 m/s, so the vertical resolution is more than 21 m or 4.1 ms, but the thinnest Granite Wash layer is less than 4.1 ms (Figure 3.11).

Since the velocity is not recorded from the top of the well, the stratigraphy is hard to correlate with seismic data in time. Based on the linear moveout velocity, the basement is deeper than 550 ms. The post-stack seismic data (Figure 3.12A, blue dashed box) shows five strong flat reflections between 500 ms to 600 ms. The shot gather indicates the velocities of these refractions (Figure 3.12B, blue dashed box) are more than 15000 ft/s. The regional stratigraphy and well logs indicate Panhandle Lime, Brown Dolomite, Granite Wash and granite basement are possible layers from top to bottom for the reflections between 500 ms to 600 ms. I use 3D tomography to identify the locations of these four layers in time. I picked two phases p1 and p2 (Figure 3.12B), p1 (green dashed line) is the direct wave, and p2 (purple dashed line) is the refraction. Since I didn't know which layer the refraction comes from, I named this layer Layer A. By comparing the results of tomography calculation and well data, I can identify what Layer A is. Total 271 shots and 52257 picks had been used in this research (Figure 3.13A). Calculations of travel times and ray paths were made the using the Fast Marching Tomography Package (FMTOMO) (Rawlinson and Urvoy, 2006). FMTOMO is a Fortran 90 software package for 3D travel-time tomography. It is one of the research products of Prof. Nick Rawlinson now at University of Aberdeen. The FMTOMO code is designed to simultaneously invert multiple travel time datasets for

3D velocity variations and interface structure. With implementation of the FMTOMO code, travel-time grids are computed. The velocity grid cell size of the starting 3D model was 60m x 60m x 10m (X, Y, depth). The top interface is 1 km above sea level and the bottom is 0.4 km below sea level. The initial depth of layer A was set based on the offset of the critical point (Figure 3.12C, gray dashed line). The depth is ~0.45km below the surface, and the average elevation of surface is ~0.9km, so the initial depth is 0.45km (Figure 3.13B). In the original velocity model (Figure 3.13B). The velocity layers are homogeneous and flat, which is based on the linear moveout velocity from the shot gathers. The top half of layer 1 has covered by dense rays, and the refraction rays covered most interface of layer A. The tomography inversion was calculated from layer 1 to layer 2 layer by layer. The layer 1 has been calculated only using P1 at first, then P1 and P2 had been used for calculation of layer 1, layer 2 and depth of interfaces. The top and bottom interfaces were fixed and did not take part in the inversion.

The inversion results (Figure 3.14) show that the velocity of the near surface is about 1 km/s, it caused by weathering zone. The velocity of next 200 m is from 2.5 km/s to 3.5 km/s, and it could represent the Red Cave Formation (Table 3.1). Above the top of layer A, the velocity is about 5km/s. In the southeast area of the survey, the layer below the weathering zone is gently flat and homogenous (Figure 3.14C). The depth changes of the interface are less than 150 m in most of the survey area (Figure 3.15). The average velocity at the depth of layer A is ~5 km/s, and the depth changes in time is about 60 ms (T.W.T.). This result agrees with the variations in the picked layers in Figure 3.16. The depth (Figure 3.15) and time (Figure 3.16) structures maintain a north to south trend. Wells A and B indicate the depth of the Panhandle Lime is 300 m, which

is same as the depth in Figure 3.15. Combining the stratigraphy and average velocity of this layer, I identify layer A to be the Panhandle Lime that is underlain by the Brown Dolomite, Granite Wash and granitic basement (Figure 3.17, red box).

All four layers have the same structurally deep and high places in the west and north corners of the survey area, and a relatively low elevation zone extends from northwest to southeast (Figure 3.16) in the central portion of the survey area. The changes of relief in most areas of each layer are about 20 ms (T.W.T.), or a 30 m variation using 3 km/s as the velocity for the conversion from time to depth. No obvious faults are identified in these four layers. The Permian section has two high amplitude, continuous, reflecting zones at the middle (around 300 ms) and the bottom of this section. The reflectors in the middle of the section are rough and more discontinuous because of weathering, and the bottom of this section has flat and continuous reflectors, which are the Panhandle Lime, Brown Dolomite and Granite Wash (Figure 3.17, yellow zone). The granitic basement has strong and continuous reflector along its top, which is a disconformity with Permian sediments. Within the granitic basement, reflectors are flat but discontinuous (Figure 3.17, brown zone).

The history of rifting in this region is well documented by studies of exposures in the Wichita Mountains in southwest Oklahoma (Figure 3.1). A layered complex partially filled the initial graben at about 575 Ma, and the Roosevelt Gabbros intruded the layered complex at about 550 Ma (Gilbert, 1983). At approximately 525 Ma, extension caused lithospheric partial melting and formation of the extrusive Carlton Rhyolite Group and the intrusive Wichita Granites (Hogan and Gilbert, 1997). The final igneous event was the intrusion of diabase sills into the Carlton Rhyolite Group.

The Granite Wash was formed by erosion and weathering during the Permian, and Permian through Tertiary sediments overly the Granite Wash. After the Pennsylvanian, this region has experienced no major deformation. Figure 3.16 indicates this area has no significant tectonic activity after Pennsylvanian. The traveltime map in Figure 3.16D shows that the granite basement only exhibits gentle relief, as do the overlying layers. The granite basement (Figure 3.16D) does two relatively low areas separately by a parallel rectangular relative high area; these are suggestive of incipient rift basin development.

Comparing the shape of granite basement and the local aeromagnetic anomalies (Figure 3.7), they do not correlate well. There are positive anomalies on three corners of the seismic survey area and anomaly values decrease to the east, the deepest region of granite basement is west corner of the seismic survey area and modest structural high occupies the central portion of the seismic survey area. Thus, the granite basement is not the only source rock for the magnetic anomalies in this area. The granite basement is intruded by gabbros that typically have higher magnetic susceptibility than granite. The gabbros produce chaotic seismic reflections at bottom of the seismic profiles that form a nonconformity with the granites (Figure 3.17, gray zone). I picked the traveltimes to the top of the gabbro (Figure 3.18), the top of the gabbro shows the same trends as the magnetic anomalies.

INTERPRETED TECTONIC EVOLUTION

According to my integrated results and previous research, I summarized my interpreted tectonic evolution of the study area. The southern margin of North America

rifted in Early Cambrian time (Thomas and Astini, 1996). The Southern Oklahoma Aulacogen also began rifting at the time, and its evolution included all of major Paleozoic structures along its length that include the Anadarko, Ardmore, and Hardeman Basins and the Wichita and Amarillo Uplifts (Brewer et al., 1983). The collision of the North American plate with the European and African - South American plates resulted in the uplifting of this region (Buckey, 2012). The collision reactivated basement faults and uplifted the Wichita Mountains (Brewer et al., 1983). The reverse faulting was combined with strike-slip faulting along this fault system during the late Paleozoic (Keller et al., 1983). Stratigraphic markers and well logs indicate left-lateral displacements along the fault zones bounding the Amarillo, Wichita, and Arbuckle Uplifts (Lemiszki and Brown, 1982; Brewer, 1986). The Amarillo Uplift consists of an en echelon series of structures that formed during the Late Mississippian or Early Pennsylvanian, and it was broken into a series of rhomb grabens and rhomb horsts probably by a left-lateral strike-slip faulting (McGookey and Budnik, 1983). The uplifting ended in the Late Pennsylvanian (Ross, 1979), and deformation of the southwestern United States ceased by the early Permian (Kluth, and Coney, 1981).

CONCLUSIONS

The larger scale structures are identified by the regional processed gravity and magnetic data. The Anadarko Basin, Palo Duro Basin and Hardeman Basin flank the Amarillo-Wichita Uplift. The Apishapa-Sierra Grande Uplift is disconnected with the Amarillo-Wichita Uplift by the Dalhart Basin. The strong gravity and magnetic anomalies and the solutions from Euler deconvolution show the Amarillo-Wichita

Uplift is covered by thin Permian and Mesozoic sediments. The THG maps of gravity and magnetic reveal the Amarillo Uplift consists of an en echelon series of rift basins formed by a left-lateral strike-slip faulting. The local magnetic data show the details of the rift basins in this area. In my study area, NW and NE trending structures are dominate. Based on the previous research and interpretations of my potential data, the 3D seismic data has been interpreted within a background of rifting and thrusting. The volumetric seismic attributes are used to determine the major features in igneous basement and overlying sediments, as well as, the relief of the basement. The results show the topography of the overlying sediments is controlled by the granite basement. The basement contains numerous failed rift basins, and the rifting directions are same as the strike of Southern Oklahoma Aulacogen and left-lateral strike slip faults. The seismic data (Figure 3.16) indicates the average thickness of dolomite and Granite Wash is about 20 ms (T.W.T.). The top of the gabbro layer dips to the southeast. This result combined the aeromagnetic low in this area (Figure 3.7), could possibly indicate that a deep rift basin is present in this area.

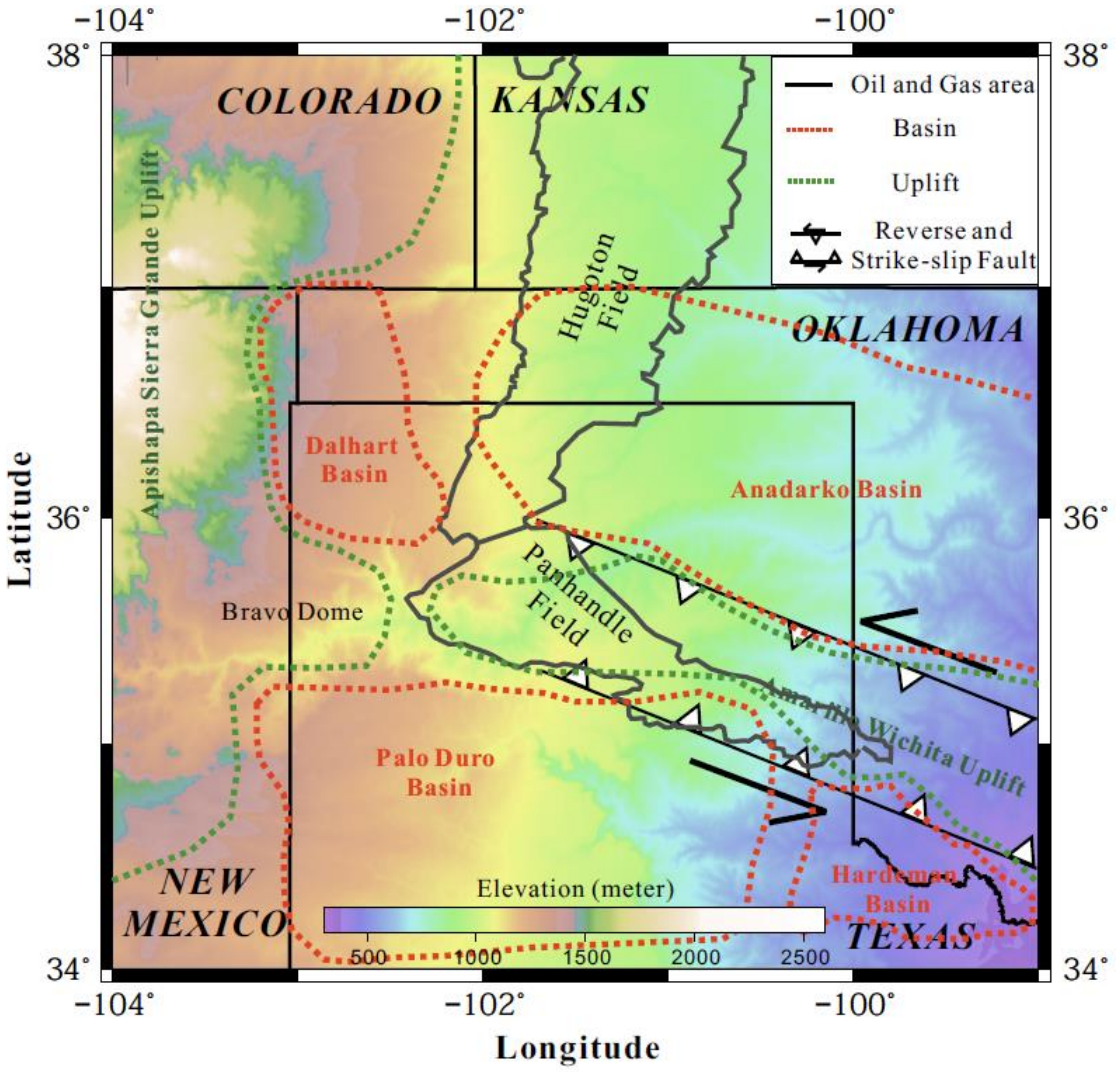

Figure 3.1. Regional topographic map with outlines of major geologic features (modified after Budnick, 1986; Caldwell, 1991; Burnett, 2002).

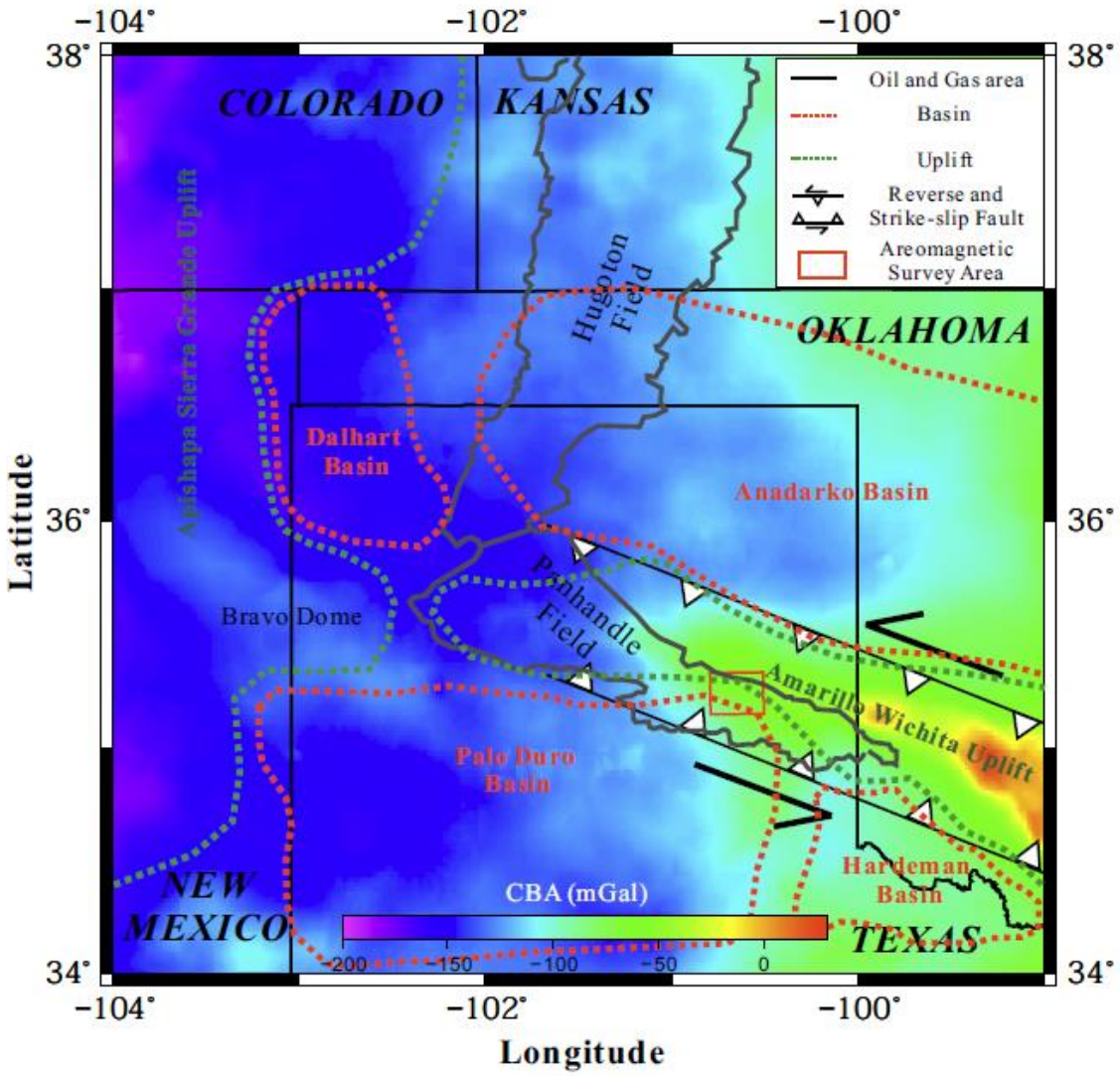

Figure 3.2. Map of the complete Bouguer anomaly (data from PACES database).

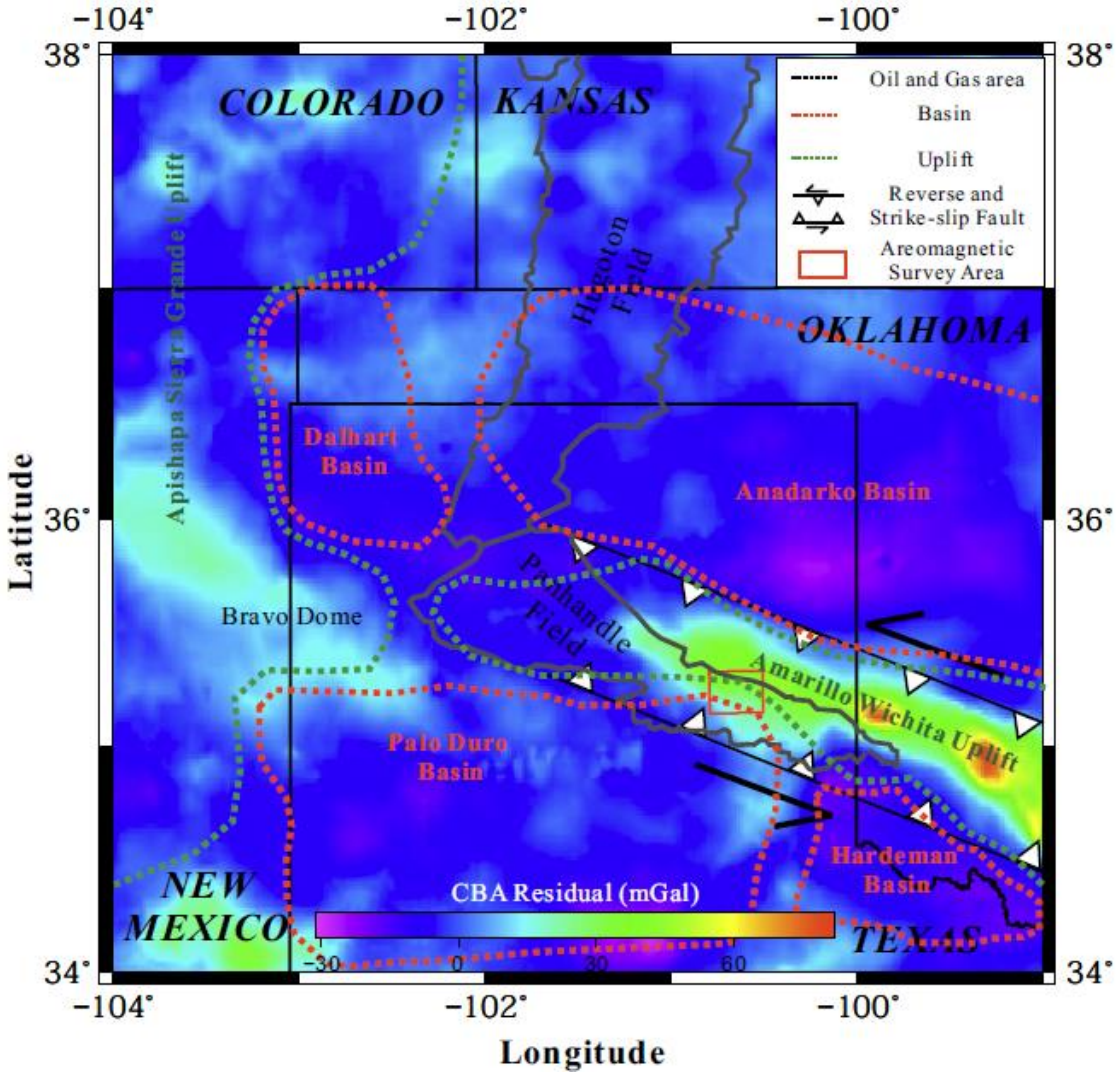

Figure 3.3. Residual complete Bouguer anomaly map calculated by subtracting the regional trend, computed using upward continuation to 40 km, from the data shown in Figure 3.2.

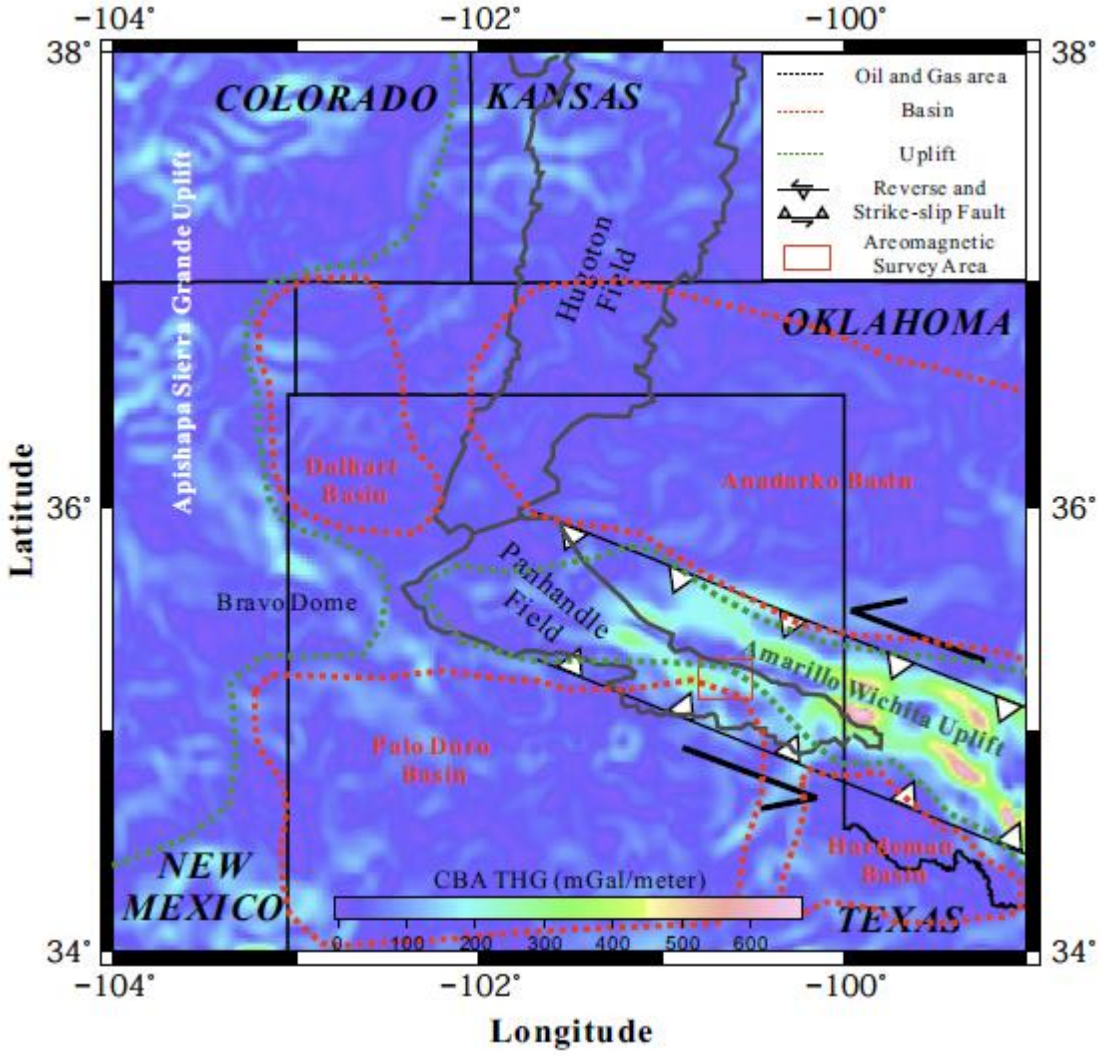

Figure 3.4. Total horizontal gradient of the residual complete Bouguer anomaly values.

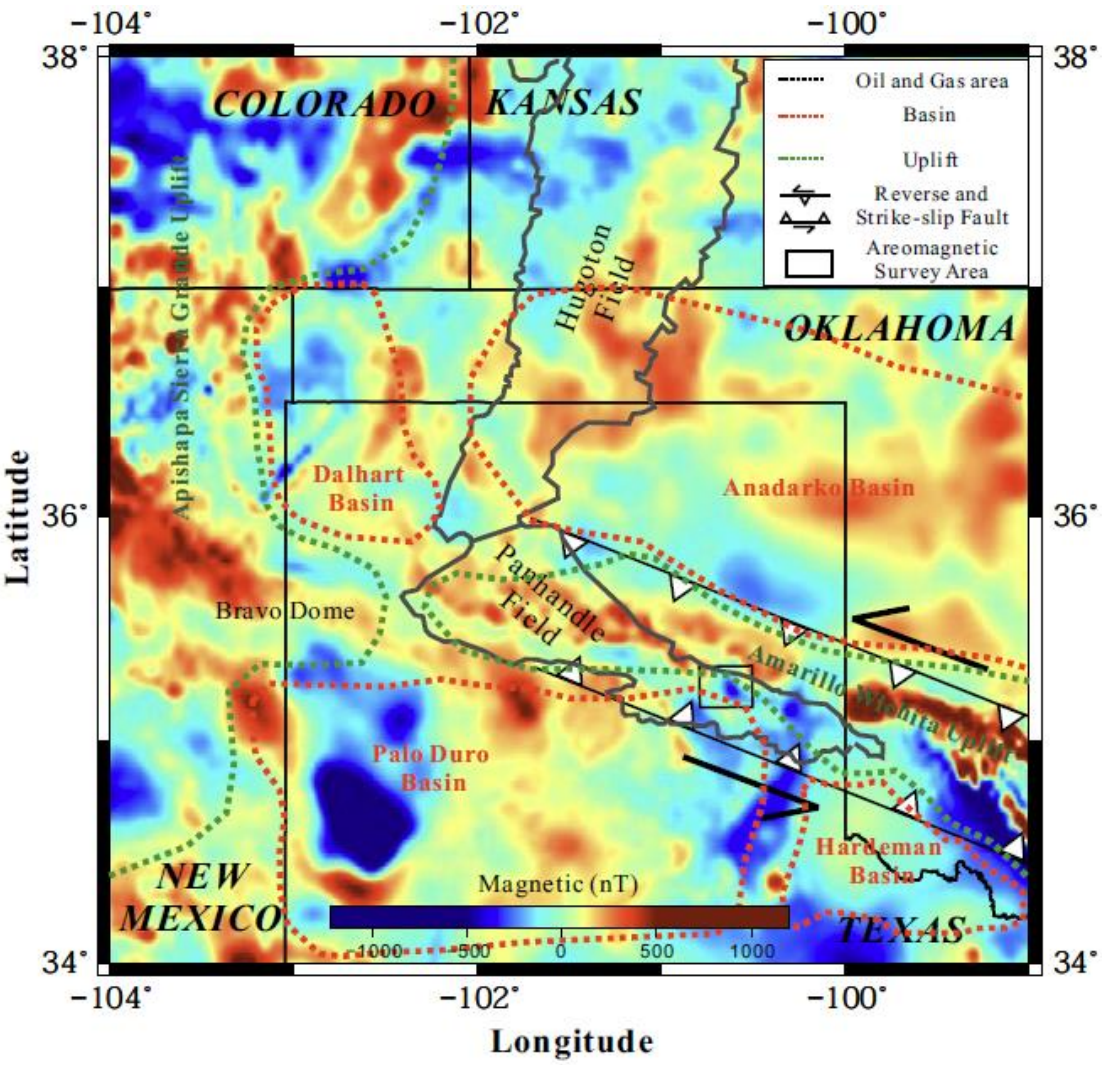

Figure 3.5. Regional residual total magnetic intensity map after reduction to the magnetic pole.

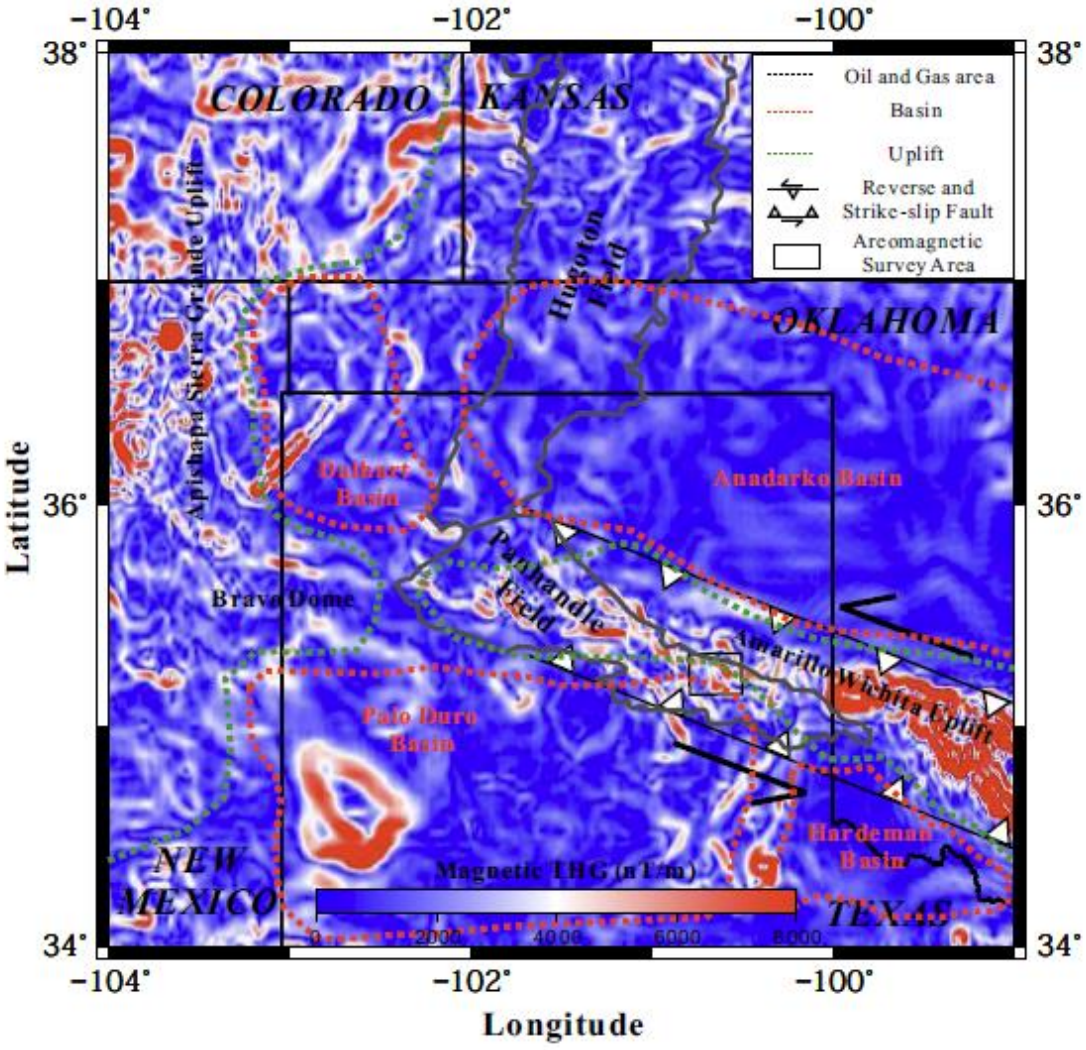

Figure 3.6. Regional total horizontal gradient map of the residual total magnetic intensity values.

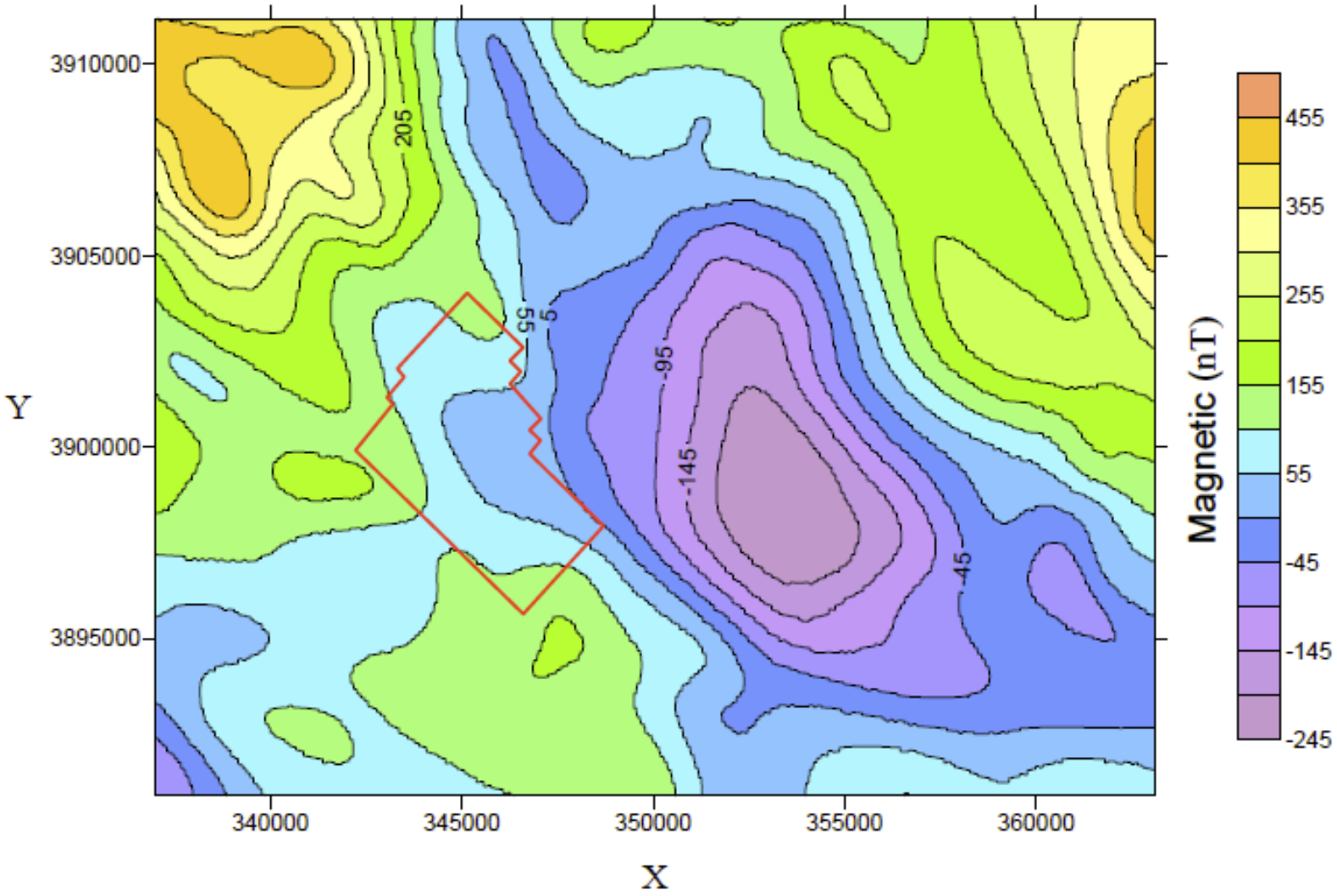
3910000
3905000
3900000
3895000
Y
340000
345000
350000
355000
360000
X
205
55
5
-95
-145
-45
Magnetic (nT)
455
355
255
155
55
-45
-145
-245

Figure 3.7. Residual total magnetic intensity map of local area after reduction to the magnetic pole. The red box is the location of the 3D seismic survey.

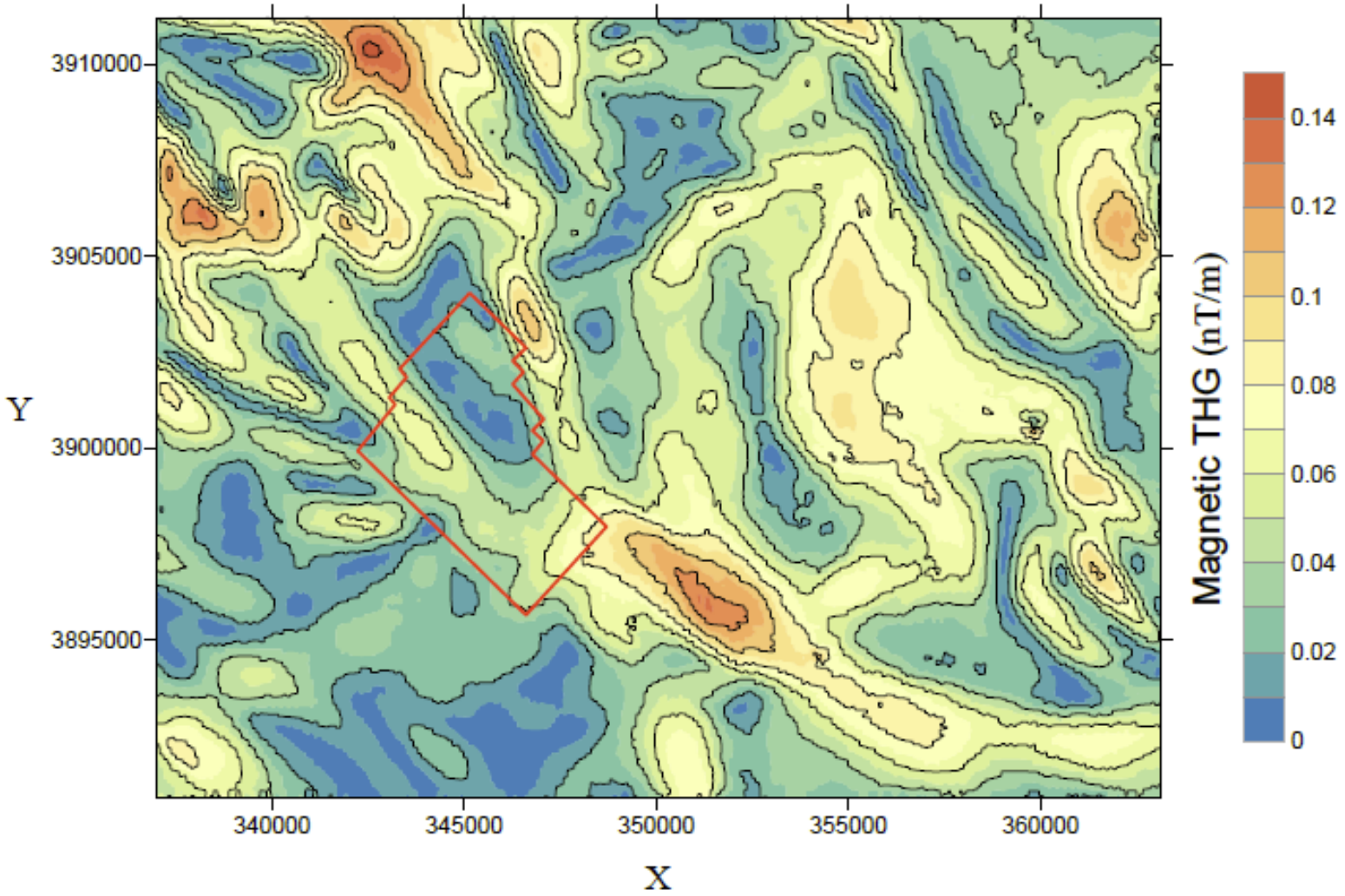
3910000
3905000
3900000
3895000
Y
340000
345000
350000
355000
360000
X
Magnetic THG (nT/m)
0.14
0.12
0.1
0.08
0.06
0.04
0.02
0

Figure 3.8. The total horizontal gradient of the reduced-to-pole residual total magnetic intensity values in the local area. The red box is the location of the 3D seismic survey.

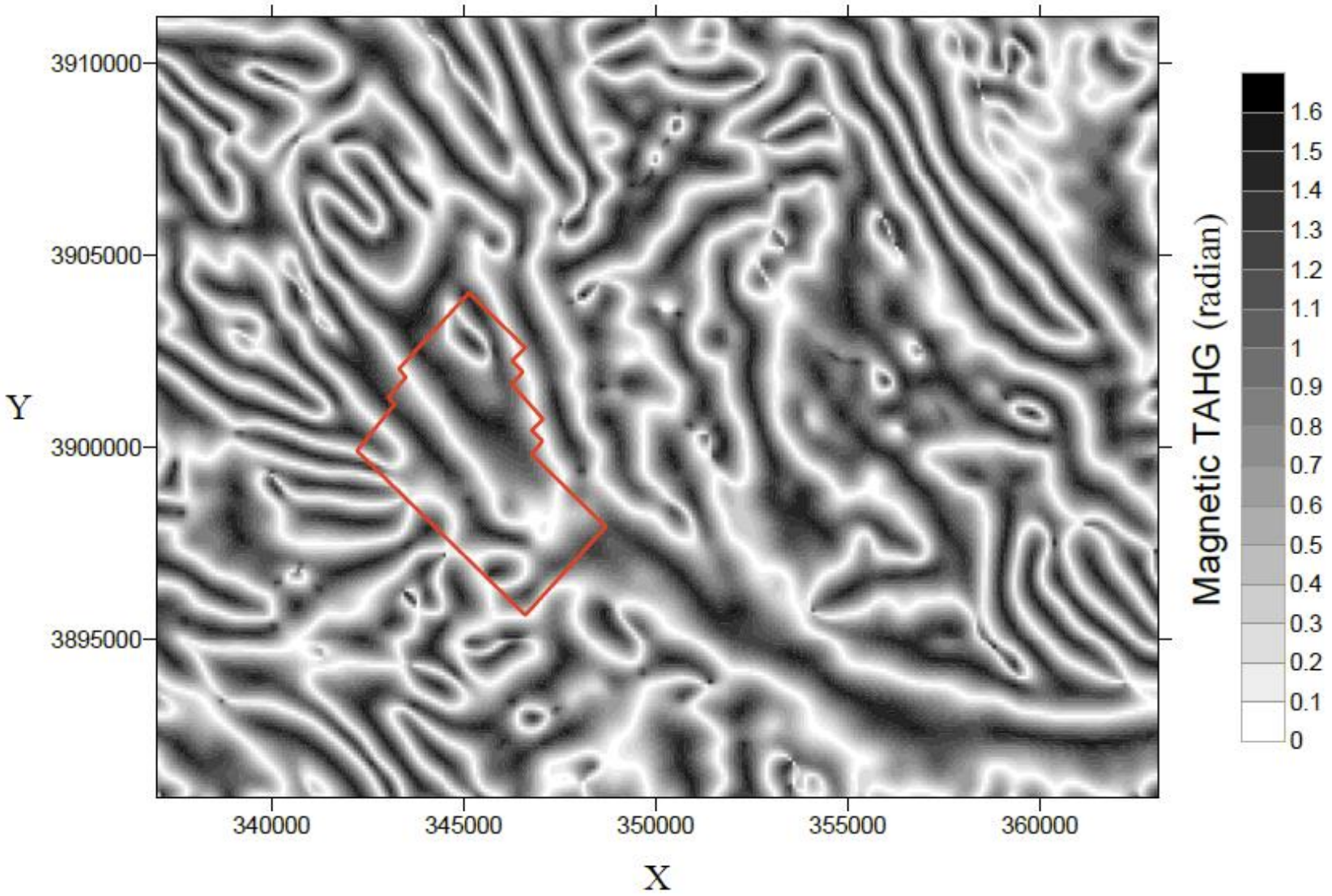
3910000
3905000
3900000
3895000
Y
340000
345000
350000
355000
360000
X
Magnetic TAHG (radian)
1.6
1.5
1.4
1.3
1.2
1.1
1
0.9
0.8
0.7
0.6
0.5
0.4
0.3
0.2
0.1
0

Figure 3.9. The tilt angle of the horizontal gradient of the reduced-to-pole residual total magnetic intensity values in the local area. The red box is the location of the 3D seismic survey.

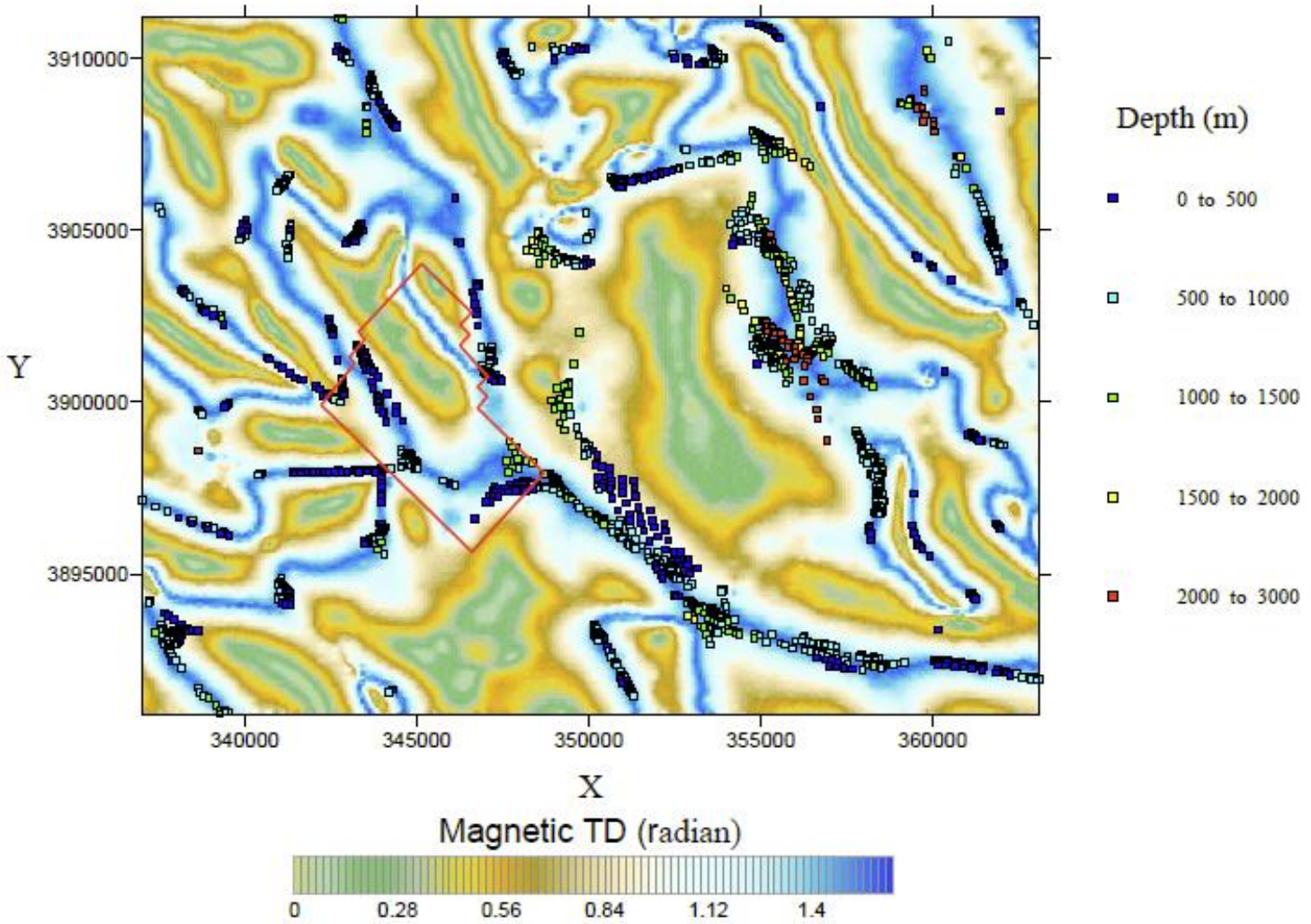
3910000
3905000
3900000
3895000
Y
340000
345000
350000
355000
360000
X
Depth (m)
0 to 500
500 to 1000
1000 to 1500
1500 to 2000
2000 to 3000
Magnetic TD (radian)
0
0.28
0.56
0.84
1.12
1.4

Figure 3.10. Standard Euler solutions of basement depth estimates plotted on top of the tilt derivative of the reduced-to-pole residual total magnetic intensity values in the local area. The red box is the location of the 3D seismic survey.

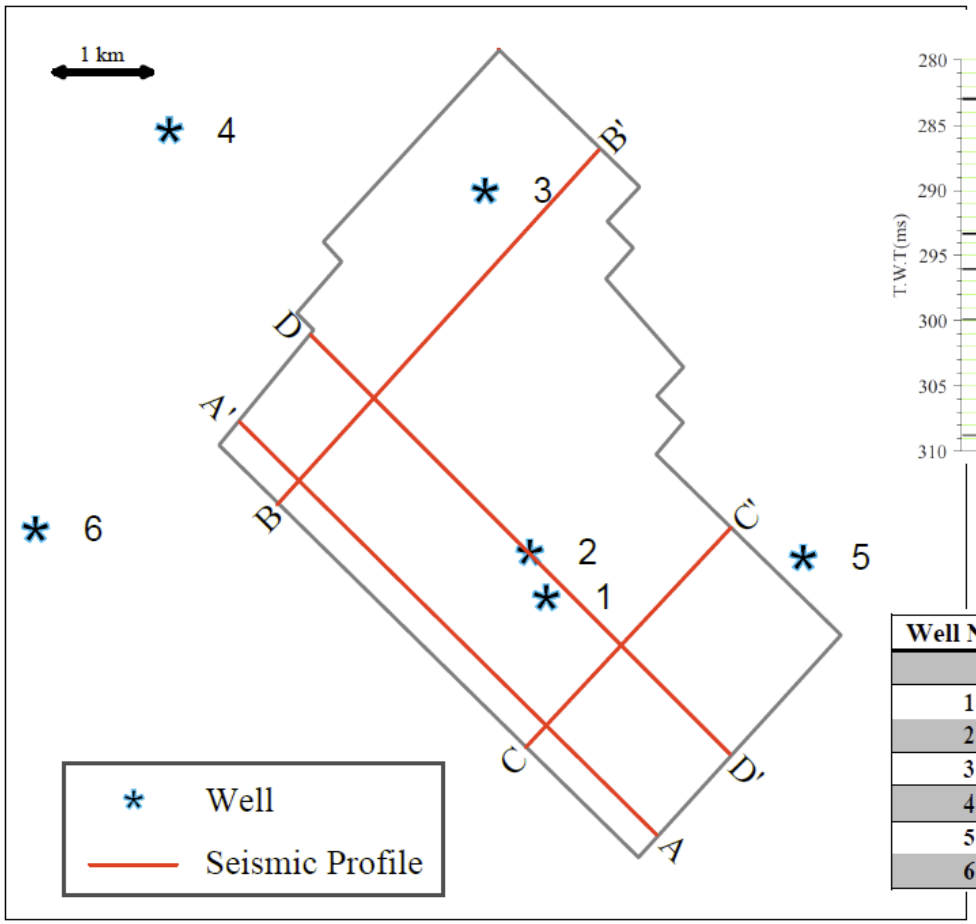

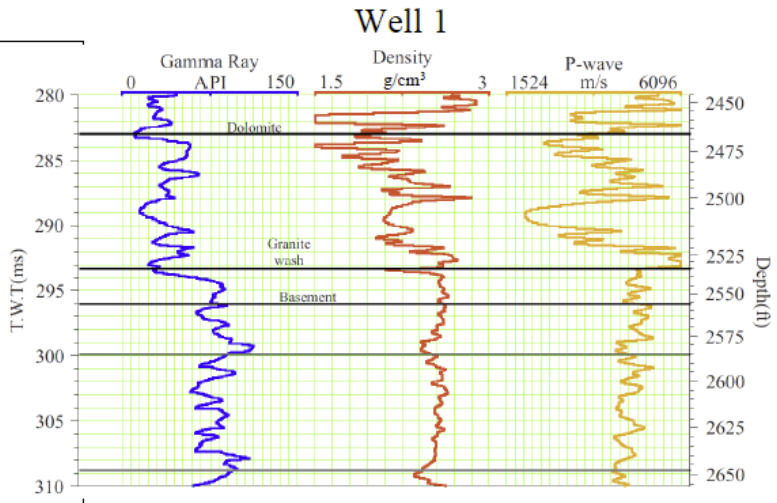

Well Name	Elevation of Layer's top (km)			
	Lime	Dolomite	Granite Wash	Basement
1	0.272	0.141	0.121	0.114
2	0.273	0.141	0.119	0.109
3			0.15	
4			0.144	
5		0.272	0.127	
6	0.228	0.089	0.67	

Figure 3.11. A) Index map with locations of seismic profiles in Figures 3.12, 3.14, and 3.17 and well available for study. 1, 2, 3, 4, 5, and 6 are the locations of the wells. B). The well logs from the well 1. The table shows the depth of layer tops from the well data.

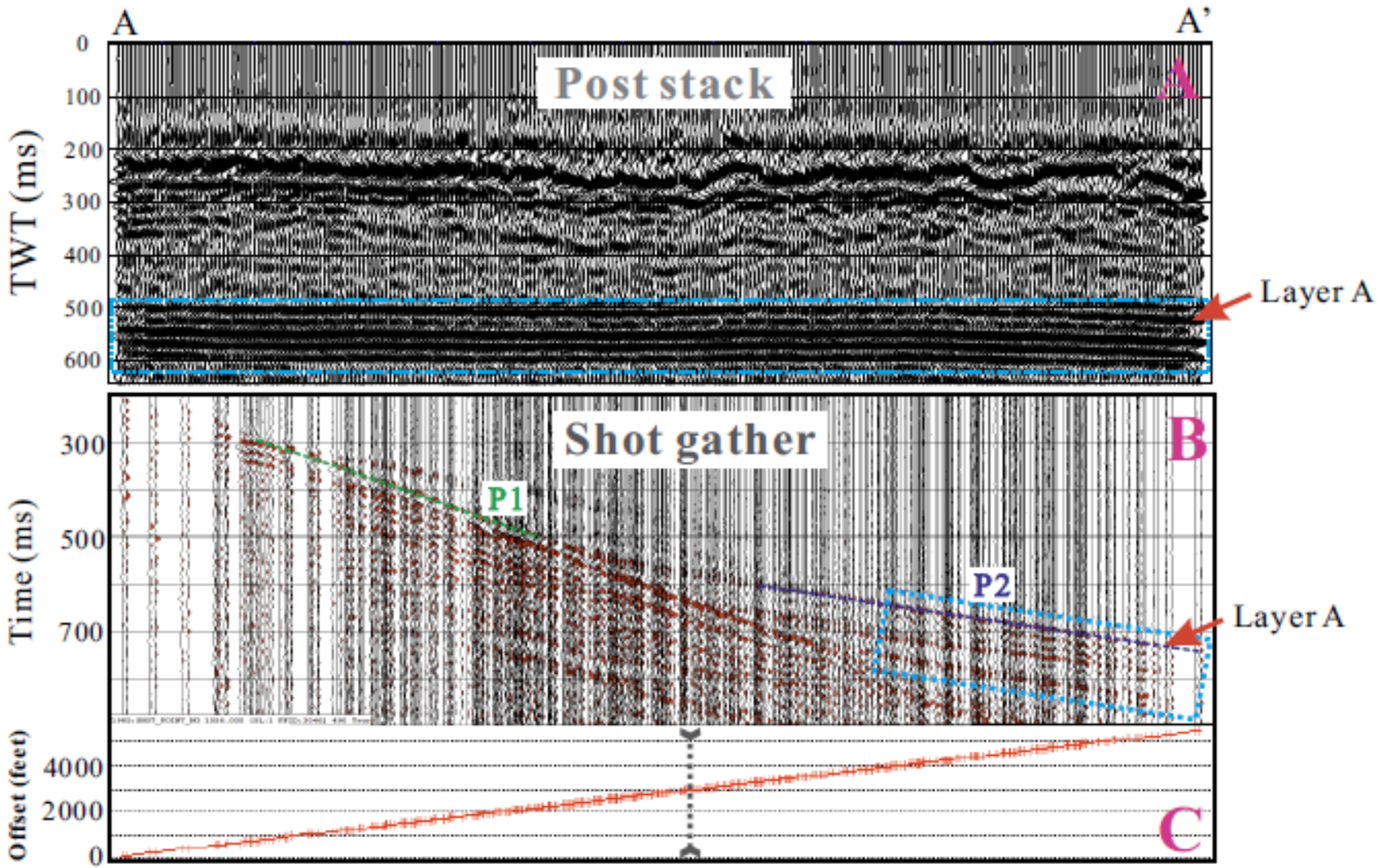
A
A'
Post stack
A
TWT (ms)
0
100
200
300
400
500
600
Layer A
Shot gather
B
P1
P2
Time (ms)
300
500
700
Layer A
Offset (feet)
4000
2000
0
C

Figure 3.12. A) Post stack seismic reflection profile, the locations are shown in Figure 3.11. B) A shot gather, P1 is the direct wave, P2 is the refraction from layer A. C) A plot of the offsets of the traces in B. The dashed line is the location of the critical point.

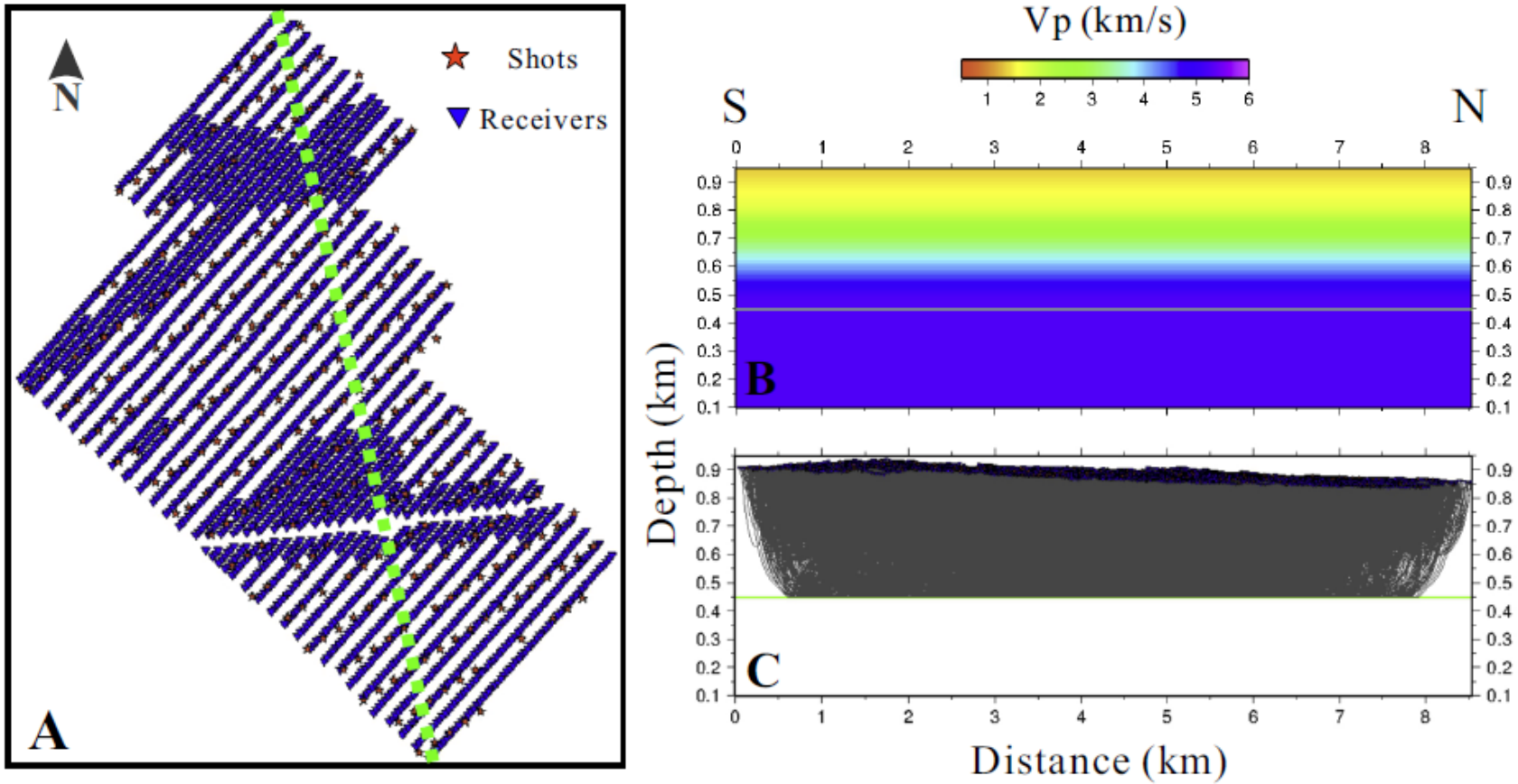
N
Shots
Receivers
A
Vp (km/s)
1 2 3 4 5 6
S
N
0 1 2 3 4 5 6 7 8
0.9 0.8 0.7 0.6 0.5 0.4 0.3 0.2 0.1
B
C
Depth (km)
Distance (km)

Figure 3.13. A) The locations of shots and receivers, the green dashed line is the location of the velocity model shown in B. B) The starting velocity model. C) Ray coverage for the starting velocity model using refraction and reflection seismic tomography.

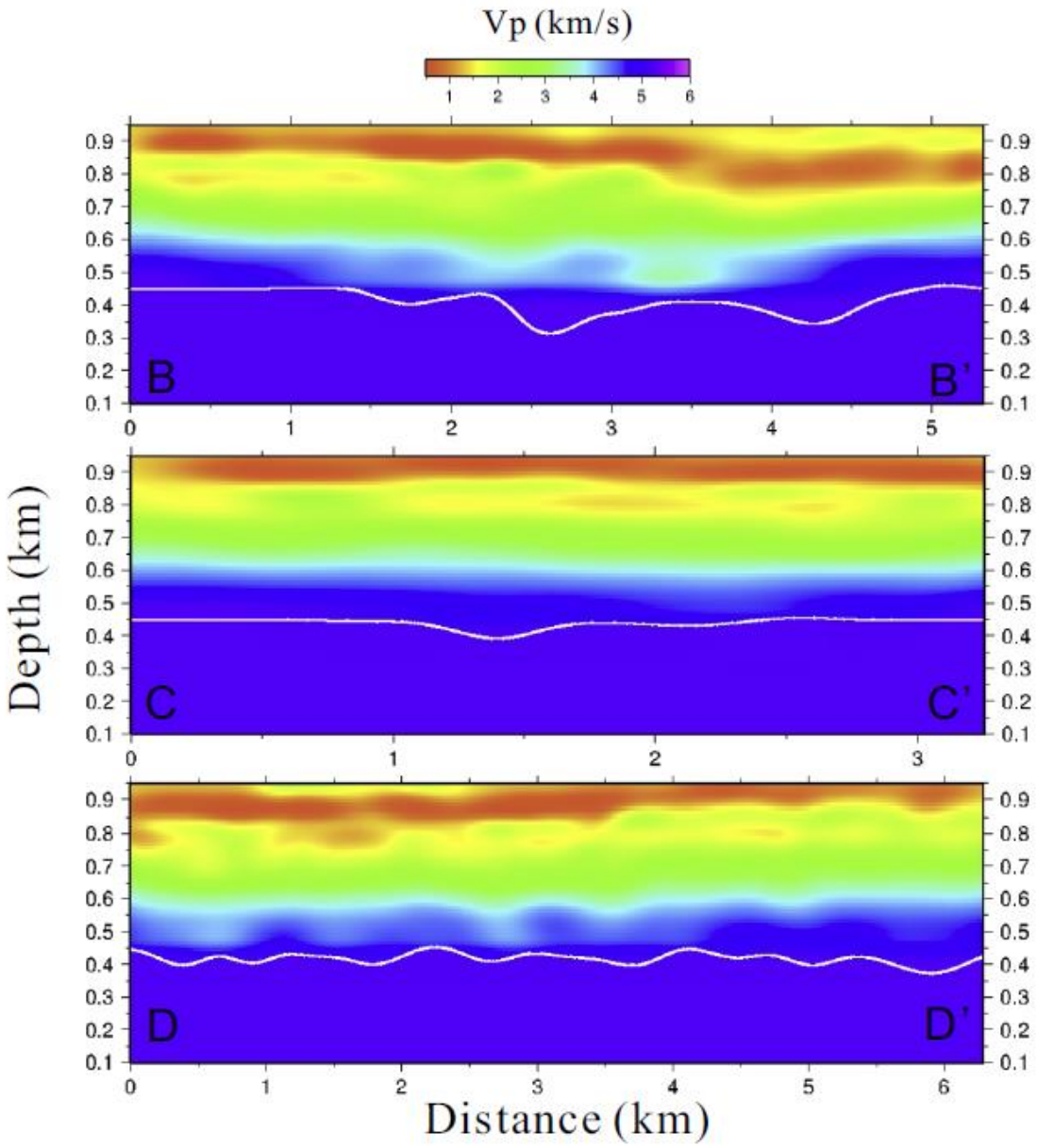

Figure 3.14. Vertical slices through the final velocity model. The white line is the top of Layer A. The locations are shown in Figure 3.11.

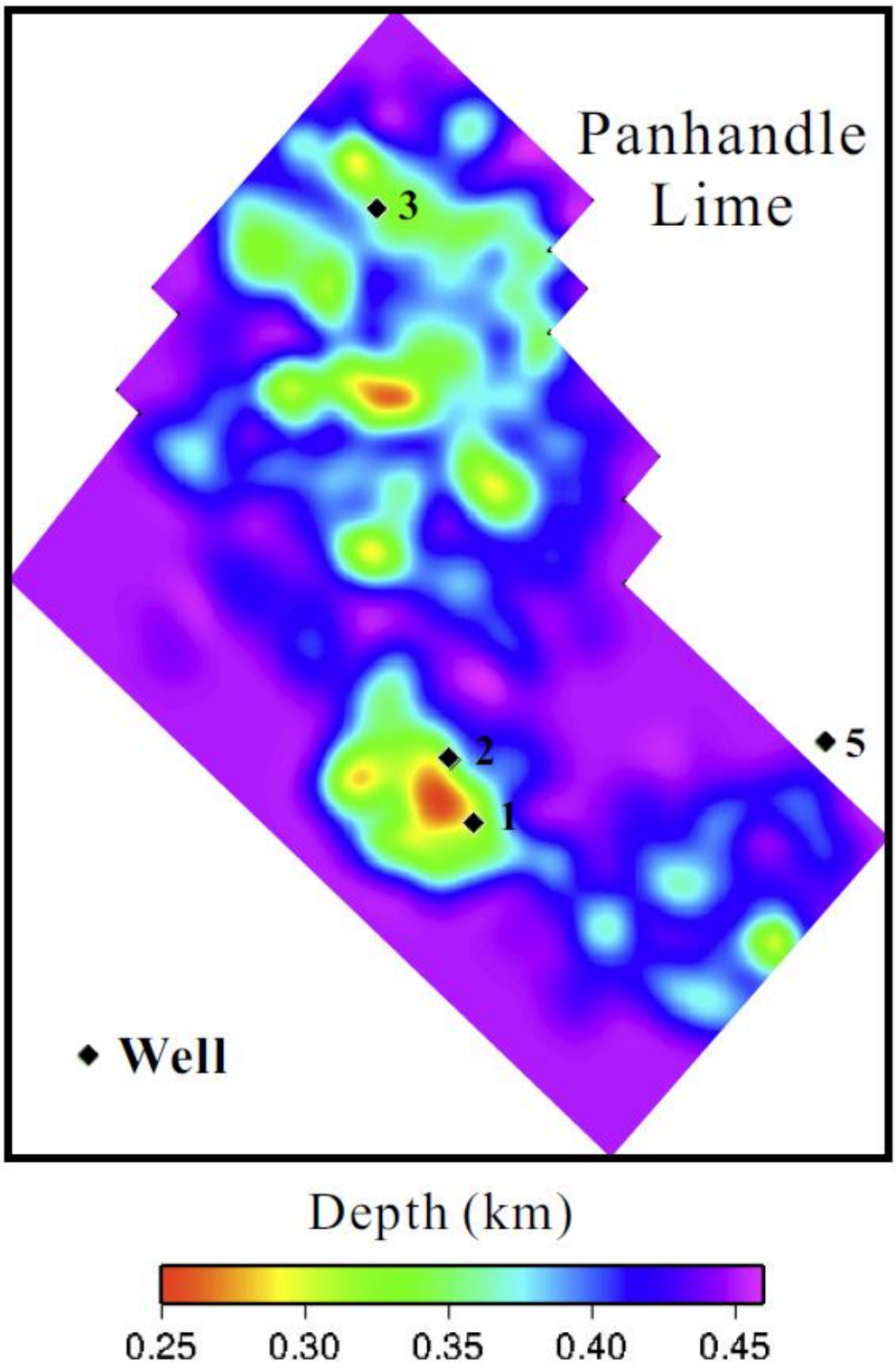

Figure 3.15. The depth map of layer A, which is the Panhandle Lime (see text).

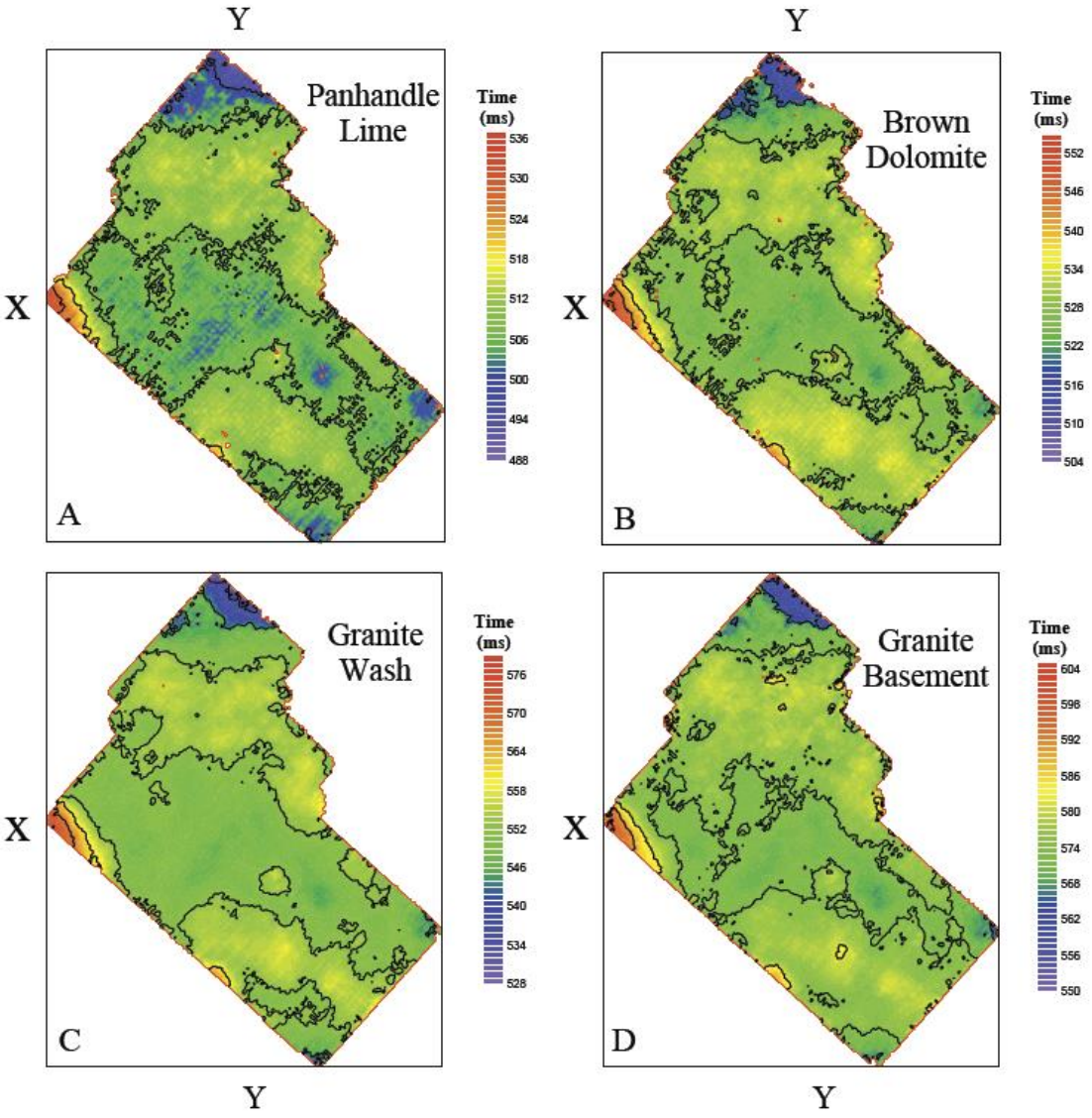

Figure 3.16. Maps of the horizontal picks of the travel times to the tops of the Panhandle Lime, Brown Dolomite, Granite Wash, and granitic basement.

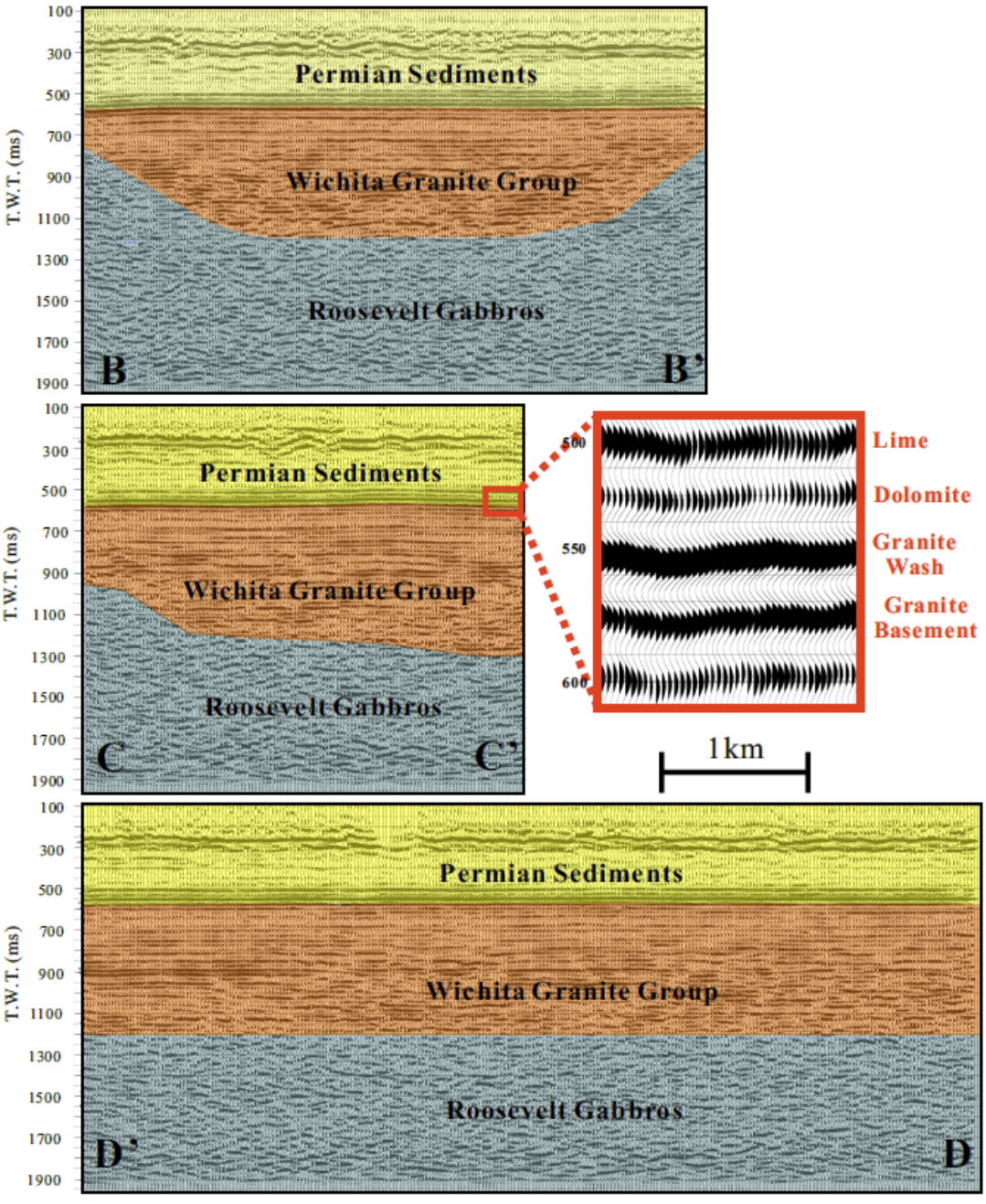

Figure 17. Interpreted seismic reflection profiles. The locations are shown in Figure 3.11.

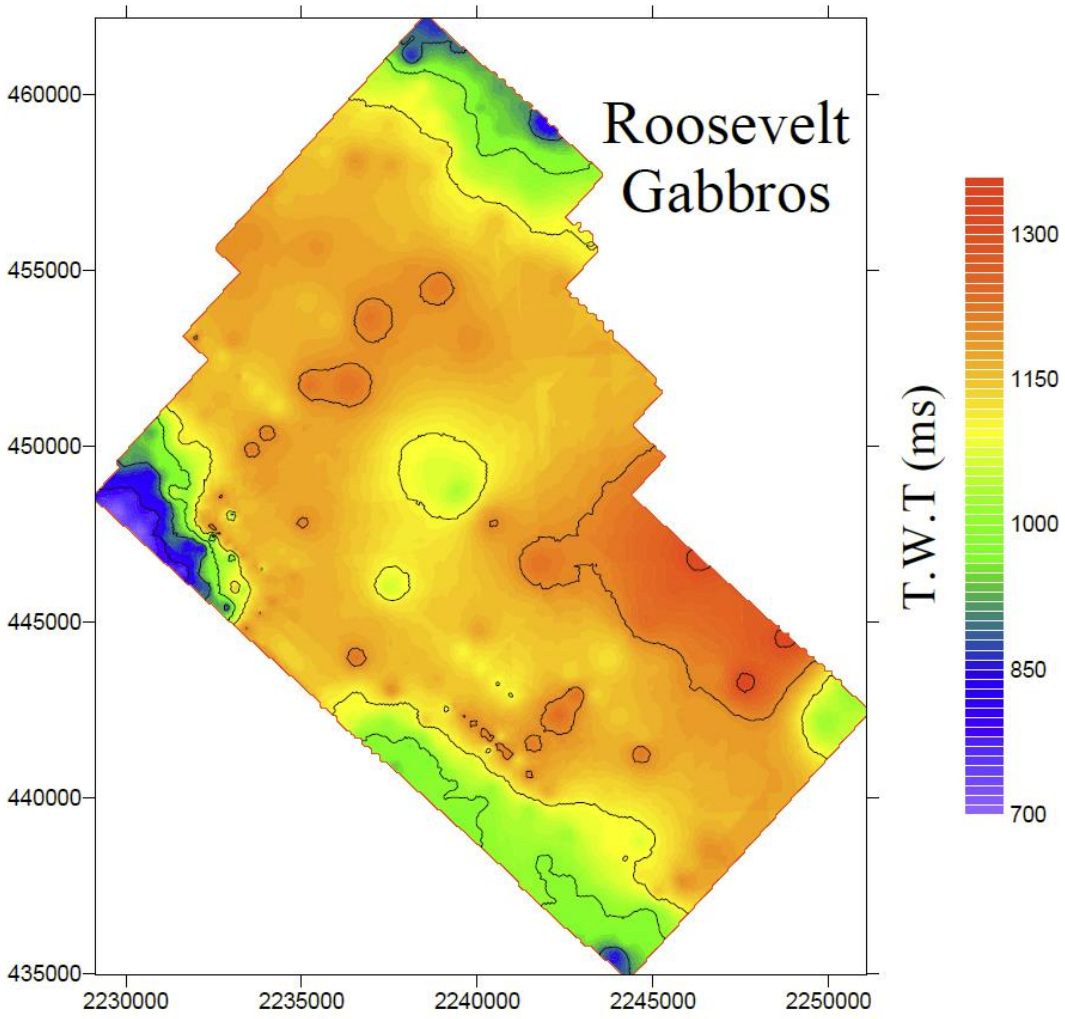

Figure 3.18. Map of the horizontal picks of the travel time to the tops of the Roosevelt Gabbros.

Table 3.1. Panhandle Field stratigraphic column (after Sorenson, 2005). The dashed lines indicate the nonconformity between the sedimentary rocks and the Amarillo Wichita Uplift.

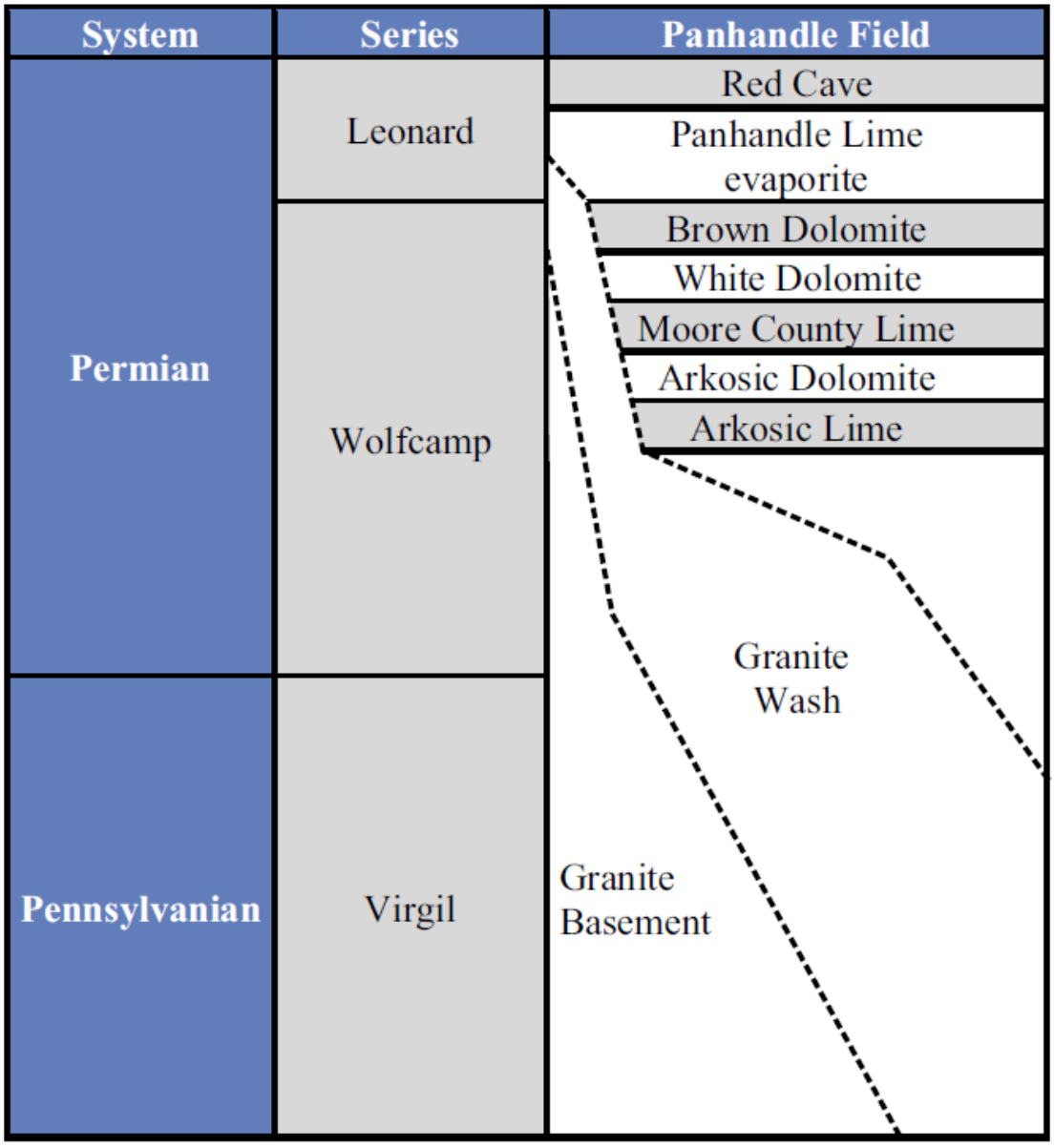

REFERENCES CITED

Barbosa, C. F., J. B. C. Silva, and W. E. Medeiros, 1999, Stability analysis and improvement of structural index estimation in Euler deconvolution: Geophysics, **64**, 48– 60, doi: 10.1190/1.1444529.

Blakely, R. J., 1996, Potential theory in gravity and magnetic applications: Cambridge University Press.

Brewer, J. A., 1982, Study of southern Oklahoma Aulacogen, using COCORP deep seismic-reflection profiles: Oklahoma Geological Survey Guidebook, **21**, 31-39.

Brewer, J. A., Good, R., Oliver, J. E., Brown, L. D., & Kaufman, S., 1983, COCORP profiling across the Southern Oklahoma Aulacogen: Overthrusting of the Wichita Mountains and compression within the Anadarko Basin: Geology, **11**, no. 2, 109-114.

Bodine, J.H., 1984, Waveform analysis with seismic attributes: Oil & Gas Journal, **84**, no. 24, 59-63.

Buckey, A. R., 2012, An Integrated Geophysical Analysis of Crustal Structure in the Wichita Uplift Region of Southern Oklahoma: Oklahoma City Geological Society Shale Shaker, **62**, no. 6, 432-452.

Budnick, R.T., 1986, Left-lateral intraplate deformation along Amarillo-Wichita Uplift, Texas panhandle and Oklahoma (Abstract): Oklahoma Geology Notes, **46**, 68.

Burnett, M., 2002, Stratigraphic adventures in the Granite Wash of Hartley County, Texas: A case of study: AAPG Bulletin, **85,** 1689-1696.

Caldwell, C. D., 1991, Cyclic deposition of the Lower Permian, Wolfcampian Chase Group, western Guymon-Hugoton field, Texas County, Oklahoma. In W. L. Watney, A. W. Walton, C. G. Caldwell, and M. K. Dubois, organizers, Midcontinent Core Workshop on Integrated Studies of Petroleum Reservoirs in the Midcontinent: Midcontinent AAPG Section Meeting, Wichita, Kansas, **91-52**,57-75.

Cooper, G.R.J., and Cowan, D.R., 2006, Enhancing potential field data using filters based on the local phase: Computers & Geosciences, **32**, no. 10, 1585-1591, doi: 10.1016/j.cageo.2006.02.016.

Donovan, R.N., 1985, The Meers fault as a hinge to the Wichita frontal fault zone: Earthquake Notes, **55**, 1.

Dutton, S. P., and Garrett, C. M. Jr., 1989, PN-13, Pennsylvanian fan-delta sandstone, Anadarko Basin, in E. C. Kosters, D. G. Bebout, S. J. Seni, C. M. Garrett Jr., L. F. Brown Jr., H. S. Hamlin, S. Dutton, S. C. Ruppel, R. J. Finley, and N. Tyler, eds., Atlas of major Texas gas reservoirs: Gas Research Institute, 146– 147.

Ferreira, F.J.F., de Souza, J., Bongiolo, de B. e S. A., and de Castro, G. L., 2013, Enhancement of the total horizontal gradient of magnetic anomalies using the tilt angle: Geophysics, **78**, no. 3, J33-J41.

Gilbert, M. C., 1983, Timing and chemistry of igneous events associated with the southern Oklahoma Aulacogen: Tectonophysics, **94**, no. 1, 439-455.

Handford, C R., 1979, Depositional History and Diagenesis of High-Constructive Delta Systems (Wolfcampian) Southeastern Palo Duro Basin, Texas: Pennsylvanian Sandstones of the Mid-Continent, 247-258

Handford, C. R., and Dutton, S., 1980, Pennsylvanian– Early Permian depositional systems and shelf-margin evolution, Palo Duro Basin, Texas: AAPG Bulletin, **64**, no. 1, 88– 106.

Hogan, J. P., and Gilbert, M. C., 1997, Intrusive style of A-type sheet granites in a rift environment: The Southern Oklahoma Aulacogen: Geological Society of America Special Papers, **312**, 299-311.

Johnson, K. S., 1989, Geologic evolution of the Anadarko Basin, in K. S. Johnson, ed., Anadarko Basin symposium: Oklahoma Geological Survey Circular, **90**, 3– 12.

Johnson, K. S., 2008, Geologic history of Oklahoma. Earth sciences and mineral resources of Oklahoma: Oklahoma Geological Survey Educational Publication, **9**, 3-5.

Jorgensen, D. G., Helgesen, J. O., and Imes, J. L. 1993, Regional aquifers in Kansas, Nebraska, and parts of Arkansas, Colorado, Missouri, New Mexico, Oklahoma, South Dakota, Texas, and Wyoming— Geohydrologic framework: U.S. Geological Survey Professional Paper, **1414-B**, 72 p.

Keller, G.R., Lidiak, E.G., Hinze, W.J., and Braile, L.W., 1983, The role of rifting in the tectonic development of the midcontinent, U.S.A.: Tectonophysics, **94**, 391-412.

Keller, G.R., and Stephenson, R.A., 2007, The Southern Oklahoma and Dniepr-Donets Aulacogens: a comparative analysis, in Hatcher, R.D., ed., 4-D Framework of continental crust: Geological Society of America Memoir, **200**, 127-143.

Kluth, C. F., and Coney, P. J., 1981, Plate tectonics of the ancestral Rocky Mountains: Geology, **9**, no. 1, 10-15.

Kluth, C.F., 1986, Plate tectonics of the Ancestral Rocky Mountains: American Association of Petroleum Geologists Memoir, **42**, 353-369.

Lemiszki, J., and, Brown, L. D.1988, Variable crustal structure of strike-slip fault zones as observed on deep seismic reflection profiles: Geological Society of America Bulletin, **100**, no. 5, 665-676.

McGookey, D.A., and Budnik R.T., 1983, Tectonic history and influence on sedimentation of rhomb horsts and grabens associated with Amarillo Uplift, Texas Panhandle (Abstract): AAPG Bulletin, **67**, no. 3, 511.

Means, J. L., and Hubbard, N., 1987, Short-chain aliphatic acid anions in deep subsurface brines: a review of their origin, occurrence, properties, and importance and new data on their distribution and geochemical implications in the Palo Duro Basin, Texas: Organic geochemistry, **11**, no. 3, 177-191.

Ross, C.A., Late Paleozoic collision of North and South America: Geology, **7**, no. 1, 41-44.

PACES, 1995, Pan American Center for Earth and Environmental Studies, University of Texas, http://research.utep.edu/Default.aspx?alias=research.utep.edu/paces, accessed 10 June 2010.

Sorenson, R. P., 2005, A dynamic model for the Permian Panhandle and Hugoton fields, western Anadarko Basin: AAPG Bulletin, **89**, no. 7, 921-938.

Soreghan, G. S., Keller, G. R., Gilbert, M. C., Chase, C. G., and D. E., Sweet, 2012, Load-induced subsidence of the Ancestral Rocky Mountains recorded by preservation of Permian landscapes: Geosphere, **8**, no. 3, 654-668.

Thomas, J. J., Schuster, R. D. and Bickford, M. E., 1984, A terrain of 1350 to 1400-m.y.-old silicic volcanic and plutonic rocks in the buried Proterozoic of the Mid-continental and in the west Mountains, Colorado: Geological Society of America, Bulletin, **95**, 1150-1157.

Thomas, W.A., and Astini, R. A., 1996, The Argentine Precordillera: A traveler from the Ouachita Embayment of North American Laurentia: Science, **273**, no. 5276, 752-757.

Thompson, D., 1982, EULDPH: A new technique for making computer-assisted depth estimates from magnetic data: Geophysics, **47**, 31–37, doi: 10.1190/1.1441278.

Ye, H., Royden, L, Burchfiel, C., and Schuepach, M., 1996, Late Paleozoic deformation of interior North America: The greater Ancestral Rocky Mountains: AAPG Bulletin, **80**, no. 9, 1397– 1432.

Conclusions

This dissertation used the integrated geophysical methods to identify various geological features, structures and tectonic evolution, which overcome the limitation of geophysical methods' multiple solutions. And the application for different scales of geological settings indicated the integrated interpretation is a powerful tool to solve all kinds of tectonic geological problems.

I used new 3D seismic tomography and gravity data to carry out an integrated study of the geometry of the subducting slabs of the North American and North Caribbean Plates. The results indicate that both slabs have an increase of dip westward, which is strongly controlled by the subduction rollback of the North American Plate. These variations affected the tectonic evolution of the Puerto Rico-Virgin Islands. Thus, the results of this research advance our understanding of the kinematic evolution of the Puerto Rico-Virgin Islands and associated natural hazards.

In order to investigate the mechanism for uplift of LMS area in the eastern Tibetan Plateau, I explored the lithospheric structure across the Songpan-Ganzi terrane, LMS and western Sichuan basin by undertaking an integrated analysis of deep seismic profiling, gravity, magnetic, and geologic data. Based on my new results and previous research, the current crust is not thick enough to support current elevation, so a 2D numerical simulation was conducted using a crustal structure model based on recent seismic refraction and reflection profiles results to discover a reasonable mechanism. The seismic and gravity results show that the crust is composed of 3 distinct layers (upper crust, middle crust and lower crust). Among them, the numerical simulation results show the middle crust beneath the Songpan-Ganzi terrane need be most ductile, which is the key factor responsible for the crustal-scale faulting, earthquake behavior

and periods of uplifting. In addition, the modeling results show the flexural stress by the strong Sichuan block is the cause of the uplift and subsidence of the Moho.

Gravity and magnetic data are the useful tool to identify the igneous basement structures in Panhandle field. The high-resolution 3D seismic data were collected in Gray County, Texas. I employed 3D travel-time tomography to help us interpreting the seismic data. My research shows the granite basement overlays on the gabbro, it is flat and less deformation. The overlaid sediments keep same relief with basement. The gabbro is dipping to southeast in this survey area. The Permian sediments are completely because of less regional tectonic actives after Pennsylvanian and the igneous basement indicates the impact of the rifting history.

Thus, the integrated geophysical methods have solved three different scales geological problems with powerful results in these study areas. Integrated geophysical methods effectively suppress the limitation of each geophysical method and combined the advantages of the methods to identify the target precisely.